

Fermilab Proposal P1021

November 28, 2011

ORKA*: Measurement of the $K^+ \rightarrow \pi^+ \nu \bar{\nu}$ Decay at Fermilab

Joseph Comfort

Arizona State University, Tempe, AZ

Douglas Bryman,[†] Luca Doria, Toshio Numao, Aleksey Sher, Dmitry Vavilov
University of British Columbia and TRIUMF, Vancouver, Canada

David Jaffe, Steve Kettell, Laurence Littenberg, Elizabeth Worcester
Brookhaven National Laboratory, Upton, NY

Leo Bellantoni, Brendan Casey, David Christian, D. A. Jensen, Andreas Kronfeld
Jonathan Lewis, Sergei Striganov, Robert Tschirhart,[†] Herman White, Peter Wilson
Fermi National Accelerator Laboratory, Batavia, IL

Kevin Pitts

University of Illinois, Urbana Champaign, IL

Corrado Gatto

Istituto Nazionale di Fisica Nucleare, Napoli, Italy

Roberto Carosi

Istituto Nazionale di Fisica Nucleare, Pisa, Italy

Yuri Kudenko, Oleg Mineev, Artur Shaykhiev
Institute for Nuclear Research, Moscow, Russia

Akram Artikov, Julian Budagov, Yuri Davydov, Vladimir Glagolev
Joint Institute of Nuclear Research, Dubna, Russia

Ahmed Hussein

University of Northern British Columbia, Prince George, Canada

Alexis A. Aguilar-Arévalo

Universidad Nacional Autónoma de Mexico

Jurgen Engelfried

Universidad Autónoma de San Luis Potosí, Mexico

Jack Ritchie

University of Texas, Austin, TX

Shaomin Chen, Mingming Ding, Zhe Wang
Tsinghua University, Beijing, China

* The Golden KAon Decay

[†] Contact Persons

Contents

1	Introduction	2
2	Theoretical Summary	6
2.1	Standard Model	6
2.2	Generic Effects Beyond the Standard Model (BSM)	11
2.3	Specific Effects Beyond the Standard Model	12
3	History of $K^+ \rightarrow \pi^+ \nu \bar{\nu}$ Experiments	18
4	Accelerator Configuration	21
4.1	The Main Injector Proton Source	21
4.1.1	Accelerator Operating Scenario and Beam Power	21
4.1.2	Establishing a High Power Slow Spill Program	22
4.1.3	Operational Considerations	23
4.1.4	Proton Source Summary	23
4.2	Target Yield Studies and Performance Requirements	23
5	Experiment Siting Options	26
5.1	Re-use of the CDF Collision Hall	26
5.2	Siting the Experiment in the Meson Detector Building	27
5.3	Siting the Experiment at SeaQuest Hall (the old KTeV Hall; NM4)	29
6	Secondary Beam Line	30
6.1	A Separated K^+ Beam	30
6.1.1	Layout and Optics	31
6.1.2	Results of Monte Carlo Calculations	33
6.2	Beamline Degradors	33
6.2.1	Beamline and Logic	34
6.2.2	Degraders and Yields	35
6.2.3	Secondaries	36

6.2.4	Summary of Degradar/Stopping Efficiency Calculations	37
7	Spectrometer	38
7.1	Magnet	38
7.2	Beam and Target	39
7.3	Drift Chamber	40
7.4	Range Stack	40
7.5	Photon Veto	40
7.6	Front-end Electronics	41
8	Trigger and Data Acquisition	42
8.1	Detector Rates and Deadtime Issues	42
8.2	Data Acquisition Architecture	43
8.3	Event Storage	44
8.4	Controls and Monitoring	45
9	Sensitivity and Background Estimate	46
9.1	Detector Acceptance	46
9.1.1	$\pi \rightarrow \mu \rightarrow e$ Acceptance	46
9.1.2	Deadtimeless Data Acquisition	47
9.1.3	Larger Solid Angle	47
9.1.4	Magnetic Field	47
9.1.5	Range Stack Segmentation	47
9.1.6	Photon Veto	48
9.1.7	Improved Target	49
9.1.8	Delayed Coincidence	49
9.1.9	Macro-efficiency	49
9.1.10	Other Acceptance Gains	50
9.2	Stopped Kaons per Year	50
9.2.1	Proton Accounting	50
9.2.2	Kaon Beamline	50

9.2.3	Kaon Production	51
9.2.4	Kaon Stopping Fraction	52
9.2.5	Expected Rate of Stopped Kaons and Signal Yield	52
9.3	Backgrounds	53
9.4	Estimated Precision on $\mathcal{B}(K^+ \rightarrow \pi^+ \nu \bar{\nu})$	54
9.4.1	Background Systematic Uncertainties	54
9.4.2	Overview of Systematic Uncertainties in Acceptance	56
9.4.3	Pion Track Acceptance Systematic Uncertainty	56
9.4.4	Acceptance of $\pi \rightarrow \mu \rightarrow e$ Detection Systematic Uncertainty	56
9.4.5	Systematic Uncertainty in Geometric Acceptance of the Trigger	57
9.4.6	Systematic Uncertainty in Acceptance Loss due to Nuclear Interactions	57
9.4.7	$T \cdot 2$ Acceptance Systematic Uncertainty	57
10	Costs	59
10.1	WBS and Costing Methodologies	59
10.2	Accelerator and Beams	59
10.3	Detector	60
10.3.1	Spectrometer Magnet	60
10.3.2	Beam and Target	61
10.3.3	Drift Chamber	61
10.3.4	Range Stack	61
10.3.5	Photon Veto	61
10.3.6	Electronics	61
10.3.7	Trigger and DAQ	62
10.3.8	Software and Computing	62
10.3.9	Installation and Integration	62
10.3.10	Project Management	62
10.4	Cost Estimate	63
11	Schedule and Funding	64

List of Figures

1.1	Schematic views of the E949 detector.	3
1.2	Range vs. kinetic energy of events satisfying cuts for E787 and E949 data.	3
2.1	One-loop electroweak diagrams.	7
2.2	Error budgets for $K \rightarrow \pi\nu\bar{\nu}$ in the Standard Model.	9
2.3	Predictions for different new physics models.	13
2.4	Predictions of p_{π^+} with ultralight neutralinos.	14
3.1	Momentum spectra of charged particles from K^+ decays in the rest frame.	19
4.1	KOPIO target concept.	24
4.2	K^+ yields and K^+/π^+ ratios.	25
5.1	Aerial view of the accelerator complex.	26
5.2	ORKA experiment siting options.	27
5.3	Option of CDF detector in B0 collision hall.	28
6.1	Beam-line layout and beam envelopes.	30
6.2	Beam momentum acceptance, spot sizes, and divergences.	33
6.3	Vertical kaon and pion spots at the mass slits.	34
6.4	Stopped, decayed, and escaped K^+	36
7.1	Elevation view of the proposed ORKA detector.	38
8.1	A scalable triggerless data acquisition architecture.	44
9.1	Estimated momentum resolution vs. pion momentum for E949 and ORKA.	48
9.2	Sensitivity vs. time	55
11.1	Funding profile.	65

List of Tables

4.1	Relationship between beam energy, cycle time, flattop, duty factor, and beam power.	22
4.2	Energy deposition and target yield studies.	24
4.3	Estimates of relative K^+ yield between BNL-E949 and the 95-GeV/ c yield point.	24
6.1	Beamline elements, and poletip fields.	32
6.2	Dipole and separator characteristics.	32
6.3	Stopped, decayed, interacted, and escaped K^+ in various regions.	35
6.4	Stopped and decayed K^+ particles in degrader and target.	36
6.5	Escaped secondary particles.	37
8.1	Approximate channel counts, hit multiplicities, and total rates for each detector.	42
9.1	Estimated acceptance increase factors for components of the acceptance.	46
9.2	Estimate of acceptance factors due to cuts on measured events.	47
9.3	Macro-efficiency of E949 compared to FNAL experiments in FY08.	49
9.4	The E949 experiment “as run” is compared with the proposed experiment.	51
9.5	The components of the background for the E949 PNN1 analysis.	53
9.6	The relative systematic uncertainty for components of the PNN1 signal acceptance in E949.	56
10.1	High level Work Breakdown Structure (WBS).	59
10.2	Estimated project cost.	60
11.1	Projected timescale and major milestones.	64

Executive Summary

A high precision measurement of the ultra-rare $K^+ \rightarrow \pi^+ \nu \bar{\nu}$ decay at Fermilab would be one of the most incisive probes of quark flavor physics this decade. Its dramatic reach for uncovering new physics is due to several important factors:

1. The branching ratio is sensitive to most new physics models which extend the Standard Model to solve its considerable problems.
2. The Standard Model predictions for the $K^+ \rightarrow \pi^+ \nu \bar{\nu}$ and $K_L^0 \rightarrow \pi^0 \nu \bar{\nu}$ branching fractions are broadly recognized to be theoretically robust at the 5–10% level. Only a precious few accessible loop-dominated quark processes can be predicted with this level of certainty.
3. The $K^+ \rightarrow \pi^+ \nu \bar{\nu}$ branching fraction is highly suppressed in the Standard Model to the level $< 10^{-10}$ (<1 part in 10 billion). This suppression allows physics beyond the Standard Model to contribute dramatically to the branching fraction with enhancements of up to factors of 5 above the Standard Model level.
4. The certainty with which the Standard Model contribution to $K^+ \rightarrow \pi^+ \nu \bar{\nu}$ can be predicted will permit a 5σ discovery potential for new physics even for enhancements of the branching fraction as small as 35%.

This sensitivity is unique in quark flavor physics and allows probing of essentially all models of new physics that couple to quarks within the reach of the LHC. Furthermore, a high precision measurement of $K^+ \rightarrow \pi^+ \nu \bar{\nu}$ is sensitive to many models of new physics with mass scales well beyond the direct reach of the LHC.

The experimental challenge of suppressing backgrounds to enable measurement of $K^+ \rightarrow \pi^+ \nu \bar{\nu}$ at the 1 in 10-billion Standard Model rate has been met successfully. Several events of $K^+ \rightarrow \pi^+ \nu \bar{\nu}$ decay have been clearly observed at BNL by using a carefully refined technique involving stopped low-energy kaons. Recently, it has become evident that the Fermilab Main Injector (MI) accelerator, running at about 95 GeV with a moderate duty factor to produce kaons, presents an opportunity to extend this approach by two orders of magnitude in sensitivity. The first order of magnitude improvement comes from the substantially brighter source of low energy kaons, and the second arises from incremental improvements to the experimental techniques firmly established at BNL. The proposed experiment at Fermilab, ORKA, will yield a precision of 5% for the $K^+ \rightarrow \pi^+ \nu \bar{\nu}$ branching ratio measurement, which is comparable to the uncertainty of the Standard Model prediction. Opportunities for further advances to attain even higher precision would be made possible by the advent of Project X.

1 Introduction

The ultra-rare decay modes $K^+ \rightarrow \pi^+ \nu \bar{\nu}$ and $K_L^0 \rightarrow \pi^0 \nu \bar{\nu}$ represent prime opportunities in the search for new physics [1]. They have been calculated to a high degree of precision within the framework of the Standard Model (SM). Hypothesized new phenomena coming from a wide range of physics beyond the SM would lead to measurable departures from its precise predictions. Study of these reactions could represent the single most incisive probe of quark flavor physics in the coming decade.

We will concentrate here on the dramatic physics reach of a high precision measurement of the decay $K^+ \rightarrow \pi^+ \nu \bar{\nu}$. The Standard Model prediction for the branching ratio is broadly recognized to be theoretically robust at the few percent level; only a few other loop-dominated quark process can be predicted with this degree of certainty. Because the $K^+ \rightarrow \pi^+ \nu \bar{\nu}$ branching ratio is highly suppressed in the SM to $< 10^{-10}$, new physics can compete and be observed with enhancement factors of up to five times the SM value. In addition, the certainty with which the SM contribution to $K^+ \rightarrow \pi^+ \nu \bar{\nu}$ is known permits 5σ discovery potential for new physics, even for enhancements of the branching fraction as small as 35%. This sensitivity is unique in quark flavor physics and probes essentially all proposed models of new physics that couple to quarks within the reach of the LHC. Moreover, a high precision measurement of $K^+ \rightarrow \pi^+ \nu \bar{\nu}$ is sensitive to many models of new physics which have mass scales beyond the reach of the LHC.

Definitively measuring $K^+ \rightarrow \pi^+ \nu \bar{\nu}$ decay at the 10^{-10} branching ratio level represents a significant experimental challenge. The poorly defined signal consists of a charged kaon followed by a charged pion, $K^+ \rightarrow \pi^+$, with no other observed particles. Potential backgrounds, primarily from other K decays at branching ratios as much as 10 orders of magnitude larger, have similar signatures. Therefore, the experimental strategy involves proving that candidate events have low probabilities of being due to background. To be successful at detecting $K^+ \rightarrow \pi^+ \nu \bar{\nu}$ and separating it from background, the detector must have powerful π^+ particle identification so that $K^+ \rightarrow \mu^+ \nu_\mu$ ($K_{\mu 2}$) and $K^+ \rightarrow \mu^+ \nu_\mu \gamma$ ($K_{\mu 2 \gamma}$) decays can be rejected, highly efficient 4π solid-angle photon detection coverage for vetoing $K^+ \rightarrow \pi^+ \pi^0$ ($K_{\pi 2}$) events and other decays, and an efficient K^+ identification system for eliminating beam-related backgrounds.

BNL experiment E949 [2] was the culmination of a long series of experiments spanning 40 years that searched for $K^+ \rightarrow \pi^+ \nu \bar{\nu}$. Like its predecessors, it employed a low-momentum beam of stopping kaons. In E949, a pure K^+ beam at 710-MeV/c was slowed in a degrader and stopped in a scintillating fiber target detector. The basic layout of the experiment is shown in Fig. 1.1.

Measurement of the $K^+ \rightarrow \pi^+ \nu \bar{\nu}$ decay involved observation of the daughter π^+ in the absence of other coincident activity in the detector. Two momentum regions were selected to reduce backgrounds from $K^+ \rightarrow \pi^+ \pi^0$ ($K_{\pi 2}$) decays: 1) “PNN1” above the $K_{\pi 2}$ peak, and 2) “PNN2” below the peak. The π^+ was identified by its kinematic features obtained from energy deposited in a scintillator calorimeter, and from momentum and range measurements. In addition, E949 used high-speed 500-MHz digitizers on all scintillation detectors to make precise observations of the complete $K^+ \rightarrow \pi^+ \rightarrow \mu^+ \rightarrow e^+$ decay sequence. The entire E949 spectrometer was immersed in a 1-T solenoidal magnetic field along the beam direction. In addition to the use of scintillating fibers and the large systems of 500-MHz digitizers, the challenges of E949 spurred the construction of the world’s most efficient detector of radiation, and the development of blind analysis methodology to avoid biases in background predictions and analysis of data. The numerous sources of potential background were extensively studied in E787 (the predecessor experiment) and E949, resulting in reliable and testable background predictions and a likelihood analysis method for evaluating potential candidate events for the probability of being due to $K^+ \rightarrow \pi^+ \nu \bar{\nu}$ or background. For the entire PNN1 high momentum region data sets from the E787/E949 experiments, the number of background events expected was less than one event.

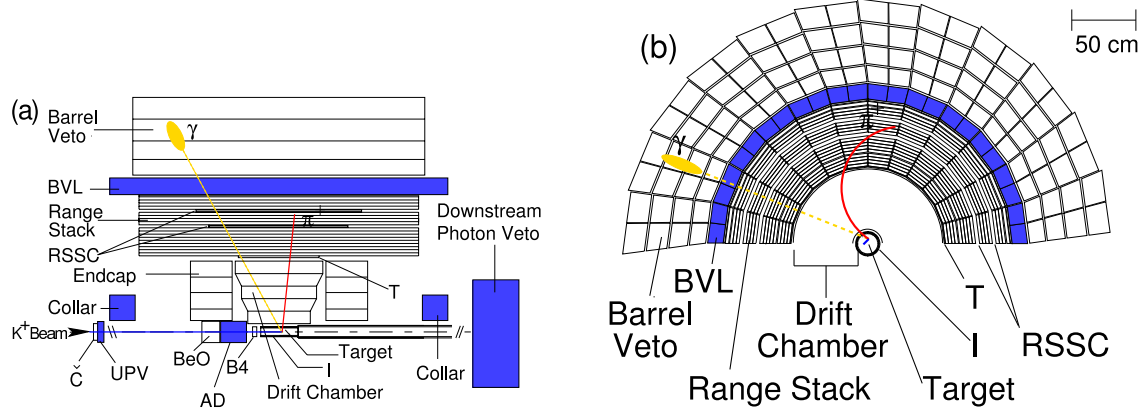


Figure 1.1: Schematic side (a) and end (b) views of the upper half of the E949 detector [2]. Illustrated in this figure: an incoming K^+ that traverses all the beam instruments, stops in the target, and undergoes the decay $K^+ \rightarrow \pi^0 \pi^+$. The outgoing π^+ and one photon from $\pi^0 \rightarrow \gamma\gamma$ are also shown.

Three events were observed by E787 and E949 in the PNN1 momentum region of $211 \leq P \leq 229$ MeV/ c , as shown in Fig. 1.2. Analysis of E787 and E949 data in the phase-space region below the $K_{\pi 2}$ peak gave four additional events resulting in an overall branching ratio result of $\mathcal{B}(K^+ \rightarrow \pi^+ \nu \bar{\nu}) = 1.73^{+1.15}_{-1.05} \times 10^{-10}$. The estimated probability that all the candidates observed by E787 and E949 were due to background was <0.001 . The measured branching ratio, although twice as large as the current SM prediction of $\mathcal{B}(K^+ \rightarrow \pi^+ \nu \bar{\nu}) = (0.781 \pm 0.075) \times 10^{-10}$, was consistent with the prediction within the statistical uncertainty.

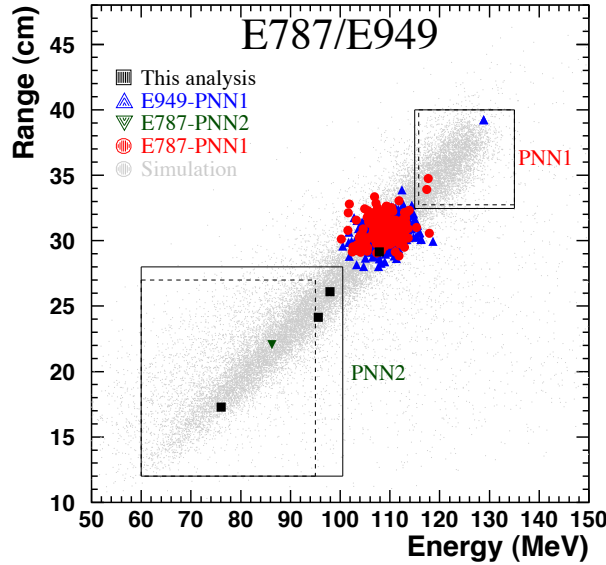


Figure 1.2: Range vs. kinetic energy of the events satisfying all of the cuts, except for the phase-space cuts on both the range and energy for all E787 and E949 data [2]. The inner rectangle represents the signal region defined in E787 (dashed lines) and E949 (solid lines). Events near $E = 108$ MeV were due to $K_{\pi 2}$ decays which were not removed by the photon veto cuts. The light points represent the expected distribution of $K^+ \rightarrow \pi^+ \nu \bar{\nu}$ events from simulation.

To obtain much higher precision in the study of $K^+ \rightarrow \pi^+ \nu \bar{\nu}$ with this approach requires a substantially higher beam intensity with a good duty factor to limit random effects. A unique opportunity for producing extremely high rates of low-energy charged kaons under favorable conditions for a measurement of the rare process $K^+ \rightarrow \pi^+ \nu \bar{\nu}$ exists at Fermilab by using the Main Injector (MI) accelerator running at 90-100 GeV. Recent investigations have shown that the MI can produce an intense secondary beam at 600 MeV/c with a 35–60% duty factor that is nearly an order of magnitude brighter in stopped K^+ mesons than was available at BNL. Another order of magnitude improvement in sensitivity can be achieved by incrementally improving on several aspects of the demonstrated performance of the BNL E949 technique. The outcome can be extrapolated with confidence to a Fermilab experiment capable of reaching 5% precision on a measurement at the SM level.

For the new experiment (ORKA), sensitivity and background estimates can be reliably made relative to the measurements for E949. The MI could be run at 90–100 GeV with a 35–45% duty factor beginning five years after the inception of NO ν A; ORKA would therefore have minimal impact on the ultimate sensitivity of NO ν A. Kaon beams of a low momentum 600 MeV/c will be used in order to substantially improve the kaon stopping efficiency. Low-energy K^+ production cross sections at 0° for 95-GeV/c protons on a platinum target were estimated from target production simulations, resulting in highly favorable yields compared to BNL. A new design for a shorter, enhanced acceptance charged K^+ beam has also been made, leading to higher flux with good pion suppression.

The basic approach employed by E949 will be used; kaons will be stopped in a highly segmented active target and $K^+ \rightarrow \pi^+ \nu \bar{\nu}$ events will be observed with a high precision central drift chamber surrounded by segmented scintillation detectors for measuring pion range, energy and the $\pi - \mu - e$ decay sequence and an efficient 4π solid angle calorimeter for vetoing events accompanied by gamma rays. An acceptance gain of >10 will be attained with reduced backgrounds by making several incremental improvements to the E949 technique. Many of the estimated improvements that result in superior background rejection and higher acceptance are quantified by using E949 data.

In the new $K^+ \rightarrow \pi^+ \nu \bar{\nu}$ experiment, an existing magnet, such as the CDF solenoid run with a 1.25-T magnetic field, will be used allowing a longer detector with increased solid angle acceptance and improved momentum resolution. Several other improvements are anticipated including finer segmentation of the pion-stopping region ‘Range Stack’ (RS) detectors. The improved design will substantially reduce muon backgrounds, providing a significant gain in acceptance due to the application of less stringent cuts. Finer segmentation of the RS will also facilitate improvements in π^+ tracking prior to stopping. Improved momentum resolution will result in improved two-body background rejection and substantial acceptance gains. In addition, the photon veto detector will be enhanced by using more radiation lengths than in E949, and by reducing inactive materials. Accidental losses (spoilage of valid events) due to extraneous hits in the photon veto system will be less of a problem than in E949.

The numbers of events expected for the new Fermilab experiment with the Main Injector kaon source would be about 210/year – two orders of magnitude greater than achieved at BNL. A precision of 5%, including projected background subtraction, would be anticipated if the branching ratio is consistent with the SM. Thus, a 5σ discrepancy could potentially be observed even if the $K^+ \rightarrow \pi^+ \nu \bar{\nu}$ branching ratio differed from the SM prediction by as little as 35%, based on projected improvements to the theory discussed in Sec. 2. Further improvements in experimental precision would be anticipated with the higher kaon fluxes available at Project X.

References

- [1] D. Bryman, W. Marciano, R. Tschirhart, and T. Yamanaka, *Ann. Rev. Nucl. Part. Sci.* **61**, 331(2011).
- [2] A. V. Artamonov *et al.*, *Phys. Rev. D* **79**, 092004 (2009).

2 Theoretical Summary

The hallmark of the $K^+ \rightarrow \pi^+ \nu \bar{\nu}$ and $K_L \rightarrow \pi^0 \nu \bar{\nu}$ decays is their clean separation of the QCD scale from the electroweak and higher scales. If the Standard Model (SM) suffices, then measurement of the branching fraction of the charged (neutral) mode yields a constraint on the CKM unitarity triangle with 2% (4%) precision. However, ORKA may well observe a rate substantially different than the SM prediction, which would be a significant discovery in its own right. Furthermore, if TeV-scale particles are observed at the Large Hadron Collider, much of high-energy physics research will start to focus on the interplay of direct observation, data-driven model building, and constraints from measurements such as these rare kaon decays.

In this theoretical overview, we start by summarizing the current status of the SM prediction of the branching ratios for both $K^+ \rightarrow \pi^+ \nu \bar{\nu}$ and $K_L \rightarrow \pi^0 \nu \bar{\nu}$. The largest uncertainties stem from the CKM matrix but, by folding in foreseeable improvements, the Standard Model predictions of the branching fractions will be known to 7% (9%). We then give a brief survey of well-motivated non-SM effects that could drastically alter the rates, while remaining in agreement with the BNL E787/949 measurement.

2.1 Standard Model

In the Standard Model (SM), the branching fraction can be written [1, 2]

$$B_{\text{SM}}(K^+ \rightarrow \pi^+ \nu \bar{\nu}) = \frac{\tau_{K^+} M_{K^+}^5}{32\pi^3} (1 + \Delta_{\text{EM}}) \left| f_+^{K^+ \pi^+}(0) \right|^2 \mathcal{I}_\nu^+ \left| \frac{GF\alpha(M_Z)}{2\pi\sqrt{2}\sin^2\theta_W} Y \right|^2, \quad (1)$$

which separates the kinematic factors, electromagnetic corrections, QCD factors (f_+ and \mathcal{I}), and the short-distance (electroweak) contribution. The last factor starts at the one-loop level, and it is convenient to separate it according to the charged lepton l and the t , c , or u quark in the loop [1, 4]

$$Y = V_{td}^* V_{ts} X(x_t) + V_{cd}^* V_{cs} [X(x_c) + |V_{us}|^4 \delta P_{c,u}] , \quad (2)$$

$$X(x_q) = \frac{1}{3} \sum_l X(x_q, x_l) , \quad (3)$$

where V denotes the CKM matrix, $x_q = m_q^2/M_W^2$, and $x_l = m_l^2/M_W^2$. The function $X(x_q, x_l)$ is computed in perturbation theory from box and penguin diagrams, starting with the diagrams in Fig. 2.1 but supplemented with higher-order QCD and electroweak corrections. The last term $\delta P_{c,u}$ encompasses long-distance effects. The status of theoretical calculations of X and $\delta P_{c,u}$ is discussed below. Equation (2) omits the short-distance contribution with an up quark in the loop, $V_{ud}^* V_{us} X(0)$. It has been eliminated with CKM unitarity, which says

$$V_{ud}^* V_{us} = -V_{td}^* V_{ts} - V_{cd}^* V_{cs}. \quad (4)$$

With this subtraction, Eq. (2) can be understood as having $X(x_q) - X(0)$ in the top-quark and charmed-quark terms. In practice, the literature redefines the notation so that $X(0) = 0$ and Eq. (2) holds as written.

An important consequence is that (after subtraction) $X(x_c) \sim -x_c \ln(x_c)$, which is the so-called GIM suppression of the charmed-loop contribution. On the other hand, the top-loop contribution is Cabibbo suppressed. In the end, the first two terms in Eq. (2) are comparably important: $V_{td}^* V_{ts} X(x_t) = 5 \times 10^{-4}$ [1, 3], $V_{cd}^* V_{cs} X(x_c) = 2 \times 10^{-4}$ [4].

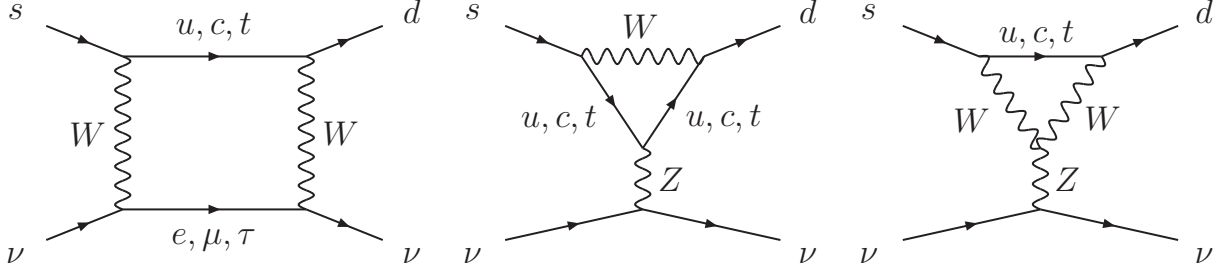


Figure 2.1: One-loop electroweak diagrams inducing the $s \rightarrow d\bar{\nu}\nu$ transition, yielding (the leading-order approximation to) the function $X(x_q, x_l)$ in Eq. (3). In practice, the charged lepton in the box can be taken massless except when $q = c$ and $l = \tau$. From Ref. [4].

The last term in Eq. (2), $\delta P_{c,u}$, accounts for two effects that, strictly speaking, spoil the clean separation of scales.¹ One is a higher-dimension operator that arises from the charmed-quark loop [5]. The other consists of long-distance effects from the up-quark loop, such as $K^+ \rightarrow \pi^0 l^+ \nu$ followed by a weak rescattering of $\pi^0 l^+$ into $\pi^+ \bar{\nu}$. Both of these effects should modify the q^2 distribution $d\Gamma/dq^2$, but this aspect has always been neglected. (Here q is the four-momentum of the $\nu\bar{\nu}$ pair.) The current estimate of these two effects is [6]

$$\delta P_{c,u} = 0.04 \pm 0.02, \quad (5)$$

by using the operator-product expansion for the contribution of charmed-quark loop, and chiral perturbation theory for the long-distance effect. This estimate could be improved with a lattice-QCD calculation [7] that will be feasible over the next few years.

The contribution with the top-quark loop, $X(x_t)$, has been calculated to two loops in the electroweak theory [8] and to next-to-leading order (NLO) in perturbative QCD [1, 3]. The remaining uncertainty from higher-order QCD is around 1%. The contribution with the charmed-quark loop, $X(x_c)$, presents a more subtle QCD problem because a series of the large $\ln(m_c/M_W)$ terms must be resummed. This treatment has been extended to next-to-next-to-leading order (NNLO) [9] and, more recently, the QED and electroweak corrections have been computed through NLO in QCD [4]. These calculations reduce the theoretical uncertainty in $X(x_c)$ to 2.3%.

The charmed-quark loop also suffers from a parametric uncertainty stemming from the charmed-quark mass, $X(x_c) \sim x_c \propto m_c^2$. With moments of charmonium correlation functions analyzed to NNNLO in perturbative QCD, one now has, in the $\overline{\text{MS}}$ scheme,

$$m_c(m_c) = \begin{cases} 1.279(13) \text{ GeV} & [10] \\ 1.273(6) \text{ GeV} & [11] \end{cases} \quad (6)$$

with the correlation functions determined from e^+e^- data [10] and from lattice QCD [11], respectively. With this precision on m_c , the associated parametric uncertainty is now comparable to those from α_s and m_t [8].

Nonperturbative QCD enters these decays in a simple way because, in the Standard Model (without right-handed neutrinos), the only dimension-six four-fermion operator that contributes is

$$Q_{\bar{\nu}\nu} = \bar{s}\gamma^\mu d \bar{\nu}_L \gamma_\mu \nu_L. \quad (7)$$

In general, the matrix element $\langle \pi | \bar{s}\gamma^\mu d | K \rangle$ entails two form factors, but the contribution to the rate from the scalar form factor $f_0(q^2)$ is suppressed by $(m_\nu/M_K)^2$, which is less than 10^{-3} with the

¹The relative factor of $|V_{us}|^4$ between δP and X is a convention introduced for numerical convenience.

pessimistic direct limit on $m_{\nu\tau}$, and several orders of magnitude smaller according to cosmological constraints. The loop diagrams also generate higher-dimension operators [5]; at dimension 8 the fields are the same but extra derivatives appear. The only important effects are suppressed by $(M_K/m_c)^2$ or $(\Lambda_{\text{QCD}}/m_c)^2$ relative to $Q_{\bar{\nu}\nu}$; they are folded into $\delta P_{c,u}$.

Integrating $|f_+(q^2)|$ over phase space leads to $|f_+(0)|^2 \mathcal{I}_\nu^+$ in Eq. (1). This separation is customary in the analysis of K_{l3} decays because the phase-space integrals \mathcal{I} can be deduced from measurements while the overall normalization cannot. In K_{l3} decays, the left-over normalization is $|V_{us}f_+(0)|^2$, and a theoretical calculation of $f_+(0)$ is used to turn the measurement into a determination of $|V_{us}|$. In the rare decays, a more accurate strategy is to take $|V_{us}f_+(0)|$ and \mathcal{I} from K_{l3} measurements. There are small differences from isospin breaking, but these have been computed in chiral perturbation theory precisely enough so that they do not play a significant role in the overall error budget [2, 12]. The extra factor of $|V_{us}|$ next to f_+ can be canceled by placing another one as a denominator for the CKM factors in Eq. (2).

Finally, the radiative corrections Δ_{EM} have been computed to order α in leading-order chiral perturbation theory, $\Delta_{\text{EM}} \approx -0.003$ [2].

The related decay $K_L \rightarrow \pi^0 \nu \bar{\nu}$ follows the same theoretical description, except that the kaon lifetime, mass, form factor, and phase-space integrals must be changed in the obvious way; there is no electromagnetic correction; and, moreover, the difference of CP conjugate amplitudes must be taken. Thus, Y in Eq. (1) is replaced with

$$\text{Im } Y = (\text{Im } V_{td}^* V_{ts}) X(x_t), \quad (8)$$

where the right-hand side omits the other terms because $x_c \text{Im } V_{cd}^* V_{cs} \approx 10^{-5} \text{Im } V_{td}^* V_{ts}$. Thus, charmed-quark effects, including the uncertainty coming from m_c and $\delta P_{c,u}$, have no influence on $B_{\text{SM}}(K_L \rightarrow \pi^0 \nu \bar{\nu})$. The isospin corrections to the QCD factors $f_+^{K^0 \pi^0}(0)$ and \mathcal{I}_ν^0 are on the same footing as $f_+^{K^+ \pi^+}(0)$ and \mathcal{I}_ν^+ [2, 12].

When all these ingredients are put together, the current Standard-Model predictions for the rates are [8]

$$B_{\text{SM}}(K^+ \rightarrow \pi^+ \nu \bar{\nu}) = (7.81_{-0.64}^{+0.72} \pm 0.33 \pm 0.26 \pm 0.08) \times 10^{-11}, \quad (9)$$

$$B_{\text{SM}}(K_L \rightarrow \pi^0 \nu \bar{\nu}) = (2.43_{-0.36}^{+0.39} \pm 0.09 \pm 0.05 \pm 0.03) \times 10^{-11}, \quad (10)$$

where the uncertainties stem from the CKM matrix,² other input parameters (α_s , m_t , m_c , $\sin^2 \theta_W$), the truncation of electroweak and QCD perturbation theory, and the (isospin-corrected) K_{l3} normalization. The overall uncertainty budget, for both neutral and charged modes, is shown in Fig. 2.2. The dominant source of uncertainty is from the CKM matrix: 9% and 15%. The theoretical and other parametric uncertainties (added in quadrature) are only 2.3% and 4.6%. In the charged mode, the uncertainties stemming from $\delta P_{c,u}$, m_c , and m_t contribute about equally, but the first of these sources of error is the hardest to estimate; eliminating it with the lattice-QCD approach of Ref. [7] would be desirable.

Below we shall assess the utility of these modes for constraining new physics. To prepare for that discussion, it is important to have a feel for how the CKM uncertainty will be reduced over the

²The PDG's uncertainty on $|V_{cb}|$ has increased over the past few years, because of a discrepancy in inclusive and exclusive determinations.

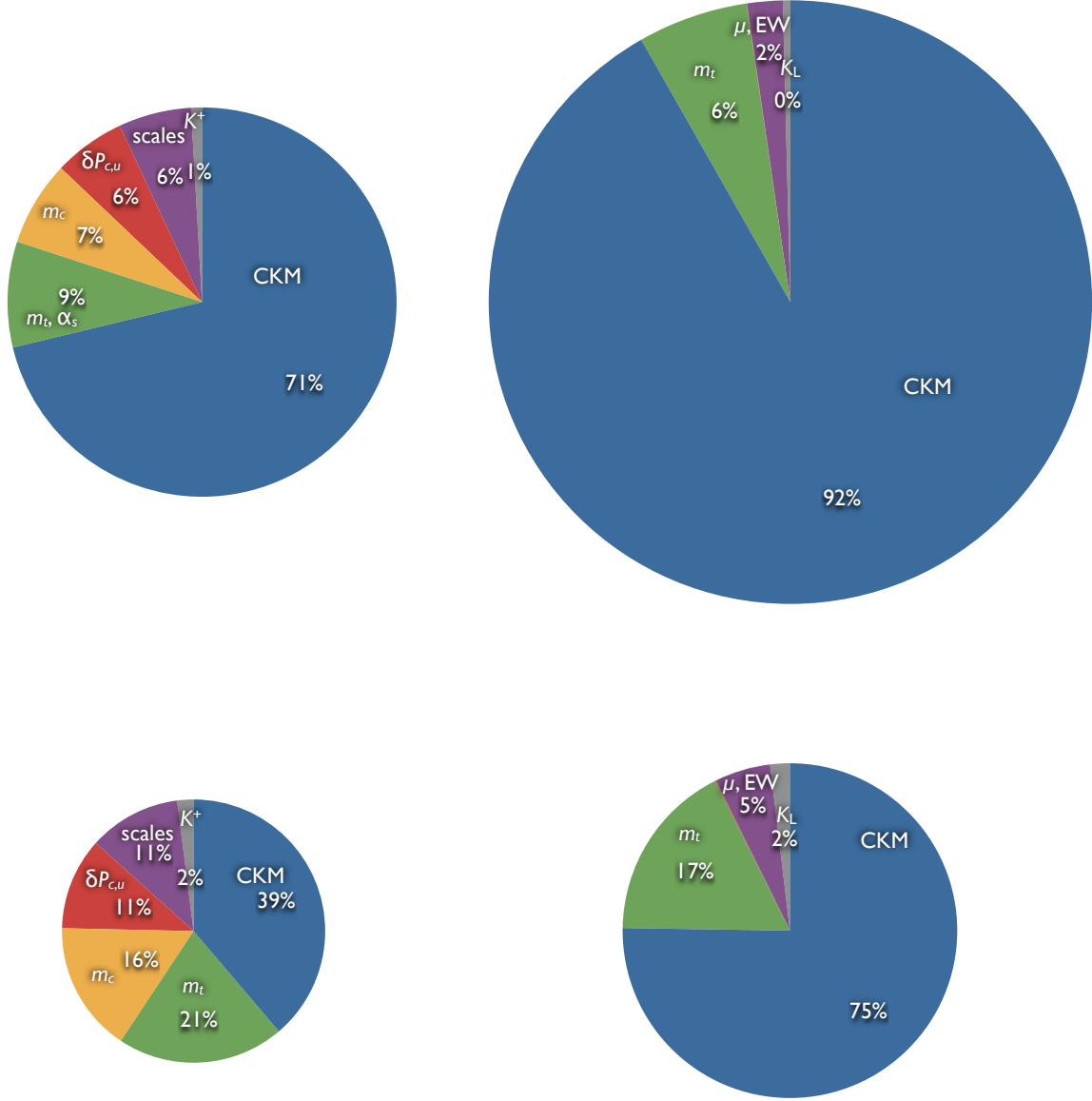


Figure 2.2: Error budgets for $B(K^+ \rightarrow \pi^+ \nu \bar{\nu})$ and $B(K_L \rightarrow \pi^0 \nu \bar{\nu})$ in the Standard Model, in light of improvements in m_c [10, 11], $X(x_c)$ [4], and $X(m_t)$ [8]. Percentages are based on the sum of errors in quadrature, and the radius is proportional to the relative error. Top left: $B(K^+ \rightarrow \pi^+ \nu \bar{\nu})$; top right: $B(K_L \rightarrow \pi^0 \nu \bar{\nu})$. Bottom: error budgets with foreseeable improvements in determining the CKM matrix.

next several years. The CKM combinations appearing in the amplitude can be re-written

$$\frac{\text{Re } V_{cd}^* V_{cs}}{|V_{us}|} \approx -V_{ud} = -\sqrt{1 - \lambda^2}, \quad (11)$$

$$\frac{\text{Re } V_{td}^* V_{ts}}{|V_{us}|} \approx -\frac{|V_{cb}| \text{Re } V_{td}}{|V_{us}|} = -\frac{A\lambda^2[A\lambda^3(1 - \rho)]}{\lambda}, \quad (12)$$

$$\frac{\text{Im } V_{td}^* V_{ts}}{|V_{us}|} \approx \frac{|V_{cb}||V_{ub}| \sin \gamma}{|V_{us}|} = \frac{(A\lambda^2)(A\lambda^3\eta)}{\lambda}, \quad (13)$$

neglecting $|V_{tb}| - 1$ and using CKM unitarity. The right-most expressions use the Wolfenstein parameterization. One sees that all four CKM parameters enter ($|V_{us}|$, $|V_{cb}|$, $|V_{ub}|$, and $\sin \gamma$ or, equivalently, $\lambda = |V_{us}|$, A , ρ , and η).

We shall discuss two general strategies for determining the CKM matrix. One is through a global analysis of all flavor-violating processes (sometimes called the unitarity-triangle fit), assuming the Standard Model. The other, which may be more germane if several non-SM sources of flavor violation begin to emerge, is the direct determination of CKM, through processes that proceed through electroweak tree diagrams. Intermediate strategies incorporating a parametrization of generic non-CKM effects can also be pursued, but their prognosis can be inferred from these two.

The CKM uncertainty in Eqs. (9) and (10) is based on a global CKM analysis, so we start here. The largest CKM uncertainty stems, for both modes, from the parameter $A = |V_{cb}|/\lambda^2$. Even in a global fit, the relative error on A essentially reflects that of the direct determination of $|V_{cb}|$, which in turn is limited by the error on the lattice-QCD calculation of the form factors for $B \rightarrow D^{(*)}l\nu$.³ Note that only one (unquenched) lattice QCD calculation is currently available [14]. For the charged (neutral) mode, the second-largest CKM uncertainty stems from $1 - \rho$ (η). In a global fit, these two depend most directly on $\sin 2\beta$ from $B \rightarrow \psi K$ and on the ratio of oscillation frequencies, $\Delta M_{B_s}/\Delta M_{B_d}$, of the neutral B mesons. Both are well measured, but only the first has negligible theoretical uncertainty. The needed ratio of hadronic matrix elements for B_q^0 - \bar{B}_q^0 mixing can be determined only via lattice QCD. Two (unquenched) calculations are available [15, 16], and others are underway [17, 18].

It is encouraging that the current status is limited by one or two lattice-QCD calculations. Lattice QCD has made great strides in the past decade [19, 20] and now seems to be well supported [21], so the scope for improvement is significant. Over the period that this experiment will be mounted and run, the available computing power should increase by two orders of magnitude. The needed lattice uncertainties not only will come down but also will be cross-checked by different groups with, say, different methods for sea quarks. Therefore, it is expected that the uncertainties for $|V_{cb}|$ and $\Delta M_{B_d}/\Delta M_{B_s}$ could be reduced by a factor of 2 or more. The same holds for $\delta P_{c,u}$ [7]. Reducing the CKM and $\delta P_{c,u}$ uncertainties by a factor of 2 improves Eqs. (9) and (10) to

$$B_{\text{SM}}(K^+ \rightarrow \pi^+ \nu \bar{\nu}) = (7.81 \pm 0.54) \times 10^{-11}, \quad (14)$$

$$B_{\text{SM}}(K_L \rightarrow \pi^0 \nu \bar{\nu}) = (2.43 \pm 0.22) \times 10^{-11}, \quad (15)$$

where all theoretical and parametric uncertainties, including those from CKM, have been added in quadrature. As shown in the bottom half of Fig. 2.2, now several uncertainties are of comparable size, so further reductions would require a sustained effort on several fronts. Equations (14) and (15) thus represent solid benchmarks for this and other experiments over the coming decade.

In a direct approach to determining the CKM matrix, it is less crucial (but still worthwhile) to reduce the uncertainty on $|V_{cb}|$ because (in the amplitude) one of the factors of A comes from $|V_{ub}|$.

³The rate for inclusive $B \rightarrow X_c l \nu$ currently quotes smaller uncertainties than for the exclusive decays, but the two methods disagree slightly, leading to an increase in the error for the average, in the usual way [13].

Moreover, because both $\sin 2\beta$ and ΔM_{B_q} are loop processes in the Standard Model, it becomes preferable to use $|V_{ub}|$ and γ (also known as ϕ_3) from tree processes to determine $1-\rho$ and η . As with $|V_{cb}|$, the error in $|V_{ub}|$ from $B \rightarrow \pi l \nu$, currently 10% from two (unquenched) calculations [22, 23], can be expected to come down by a factor of 2 or more. Recent projections [24] from the LHCb experiment expect a measurement, combining several tree processes, of γ with an error of $8-10^\circ$ ($4-5^\circ$) with 0.5 fb^{-1} (2 fb^{-1}), and an earlier projection [25] anticipates 2.5° with 10 fb^{-1} . This precision corresponds to 2% (1%) on $\text{Re } V_{td}/|V_{ub}|$ and $\sin \gamma$, and eventually 0.6%, leaving $|V_{ub}|$ and $|V_{cb}|$ as the most important sources of (CKM) uncertainty.

With a forecast of a 5% error on $|V_{ub}|$, the CKM uncertainty (without a global CKM fit) on the branching fractions for $K \rightarrow \pi \nu \bar{\nu}$ would exceed that quoted now (based on a global fit). Note, however, that one would abandon the global fit only if the corpus of results for flavor violation and new TeV particles suggested widespread deviations from the Standard Model. Under that scenario, the rare K decays may lose some of their precision, but their importance in sorting out the physics would be correspondingly greater, either as a constraint on CKM or as a diagnostic of new physics.

2.2 Generic Effects Beyond the Standard Model (BSM)

Before discussing specific extensions of the Standard Model, it is instructive to consider how, in general, non-SM particles could alter the branching fraction. As a rule, any new particles with flavor-changing neutral currents will change the short-distance coefficient of the effective interaction $Q_{\nu\nu}$. Then, in Eq. (1), one replaces

$$\frac{G_F \alpha(M_Z)}{2\pi\sqrt{2}\sin^2\theta_W} Y \rightarrow \frac{G_F \alpha(M_Z)}{2\pi\sqrt{2}\sin^2\theta_W} Y + C_{\text{new}} X_{\text{new}}, \quad (16)$$

where X_{new} is a function of new particle masses in the new loop (or, in principal, tree) diagrams, and C_{new} represents coupling factors from the vertices, including new CP -violating phases. Should experiments at the LHC observe new particles, many new models will be devised to account for the observations. In any useful model, $C_{\text{new}} X_{\text{new}}$ is well-defined and computable so, in this general way, rare kaon decays put a constraint on new physics.

The electroweak couplings in Eq. (16) presume conventions for absorbing radiative corrections, but at the tree level

$$\frac{G_F \alpha(M_Z)}{2\pi\sqrt{2}\sin^2\theta_W} = \frac{1}{4M_W^2} \left(\frac{g_2^2}{4\pi} \right)^2, \quad (17)$$

where g_2 is the weak $SU(2)$ gauge coupling. A generic BSM loop is expected to have couplings of this size and a mass of a few to several times larger than M_W . If its (analog to) the CKM and GIM suppression in the Standard Model is not severe, then relatively large effects can arise.

With nonzero neutrino mass, one should also consider effective interactions with right-handed neutrinos. As discussed above, even without new particles directly entering the $s \rightarrow d \nu \bar{\nu}$ transition, the nonzero neutrino mass implies (minute) corrections from the scalar form factor $f_0(q^2)$. To see these effects from the shape, not only would the measurements have to be sufficiently precise, but other influences on the shape, for example from the effects lumped into $\delta P_{c,u}$, would have to be understood at a similar level.

Exchanges of new particles could also lead to other four-fermion operators, such as $\bar{s}d \bar{\nu}_R \nu_L$, $\bar{s}d \bar{\nu}_L \nu_R$, $\bar{s} \sigma^{\mu\rho} d \bar{\nu}_R \sigma_{\mu\rho} \nu_L$, and $\bar{s} \sigma^{\mu\rho} d \bar{\nu}_L \sigma_{\mu\rho} \nu_R$, which would bring in the scalar form factor $f_0(q^2)$ and also a tensor form factor $f_2(q^2)$. Such contributions need not be suppressed by the neutrino mass-squared and would enter the rate as $|C_{\text{new}} X_{\text{new}}|^2$ or $(m_\nu/M_K) Y_{\text{SM}} C_{\text{new}} X_{\text{new}}$. Such contributions are not

likely to be as visible as those in Eq. (16), which interfere with the SM amplitude without neutrino helicity suppression. In any case, we do not know of any attractive models that generate such effects.

2.3 Specific Effects Beyond the Standard Model

There is now a substantial literature on the subject of new physics effects on $K \rightarrow \pi \nu \bar{\nu}$. A summary that covers developments through 2007 can be found in Ref. [26]. In this discussion we will focus mainly on examples recent enough that we can be confident that the constraints imposed on the model are reasonably current. In fact, the majority of the models studied can accommodate effects that would be significant in a $K^+ \rightarrow \pi^+ \nu \bar{\nu}$ experiment with 5% precision. This is true in large part even in models that incorporate the very restrictive Constrained Minimal Flavor Violation (CMFV) assumptions [27], *i.e.* that there are no new sources of flavor violation and no new effective dimension-six flavor-changing operators beyond the Standard Model ones. With a further assumption that charged leptons and neutrinos couple in the same way, in terms of the experimental precision proposed here, the possible range of $B(K^+ \rightarrow \pi^+ \nu \bar{\nu})$ is $[-9.6\sigma, +4.5\sigma]$ with respect to the Standard Model [28]. Without this extra assumption [29], $B(K^+ \rightarrow \pi^+ \nu \bar{\nu})$ is constrained only by experimental bounds on $B(B^+ \rightarrow K^+ \nu \bar{\nu})$, which are a few times the SM expectation [30, 31].

Examples where excursions from the SM value of $B(K^+ \rightarrow \pi^+ \nu \bar{\nu})$ could easily be more than 3σ from the SM value include the general MSSM [32, 33], the Minimal 3-3-1 Model (in which the weak $SU(2)_L$ gauge group is extended to $SU(3)_L$) [34], a Littlest Higgs model with T -parity [35], models incorporating a warped extra dimension with custodial protection [36], an extra down-type isosinglet quark model [37], and a 5-dimensional split fermion model [38], among others. In many cases, non-SM effects could be observable in $B(K^+ \rightarrow \pi^+ \nu \bar{\nu})$, even though the superficially similar $B(B^+ \rightarrow K^+ \nu \bar{\nu})$ remains consistent with the SM.

In other cases, rather than explicit predictions of the $K^+ \rightarrow \pi^+ \nu \bar{\nu}$ decay rate, the current result from BNL E787/949 is used to limit the parameters of models of new physics. Examples include R -parity violating supersymmetry [39], extended technicolor [40], anomalous charm couplings [41], singlet and triplet leptoquarks [42], a fourth quark generation [43, 44, 45], non-standard neutrino interactions [46], and more generic semi-phenomenological schemes [47]. A more precise value for $B(K^+ \rightarrow \pi^+ \nu \bar{\nu})$ would serve to eliminate many of these models, or to refine or confirm them.

Note that the already considerable power of $K^+ \rightarrow \pi^+ \nu \bar{\nu}$ to probe new physics would be significantly enhanced by the availability of a measurement of $K_L \rightarrow \pi^0 \nu \bar{\nu}$. This point has been well-explored, most recently by Blanke [48]. Fig. 2.3 gives a sense of the possibilities for several popular theoretical approaches [49]. Similar results have been found by other authors [50].

It is also important to note that the experimental signature of $K \rightarrow \pi \nu \bar{\nu}$, a π^+ emerging from a K^+ decay with missing energy, is shared by other, non-SM, processes. Perhaps the smallest excursion from the SM is the case in which the process is still $K \rightarrow \pi \nu \bar{\nu}$, but the neutrino flavor is not conserved. Such models include versions of supersymmetry [52] and new effective four-fermion interactions involving neutrinos [46]. As in the case of most examples of lepton flavor violation in kaon decay, the effects tend to be small, although there are exceptions.

A second category is reactions in which a single unseen particle recoils against the π^+ . These cases include species of axions [53], the familon [54], light scalar pseudo-Nambu Goldstone bosons in models of meta-stable SUSY breaking [55], sgoldstinos [56], a gauge boson corresponding to a new $U(1)'$ gauge symmetry [57, 58], and various light-mass dark-matter candidates [59, 60, 61]. In general these models do not predict branching ratios; rather they use limits on $K^+ \rightarrow \pi^+ + \text{“nothing”}$ to constrain their parameters.

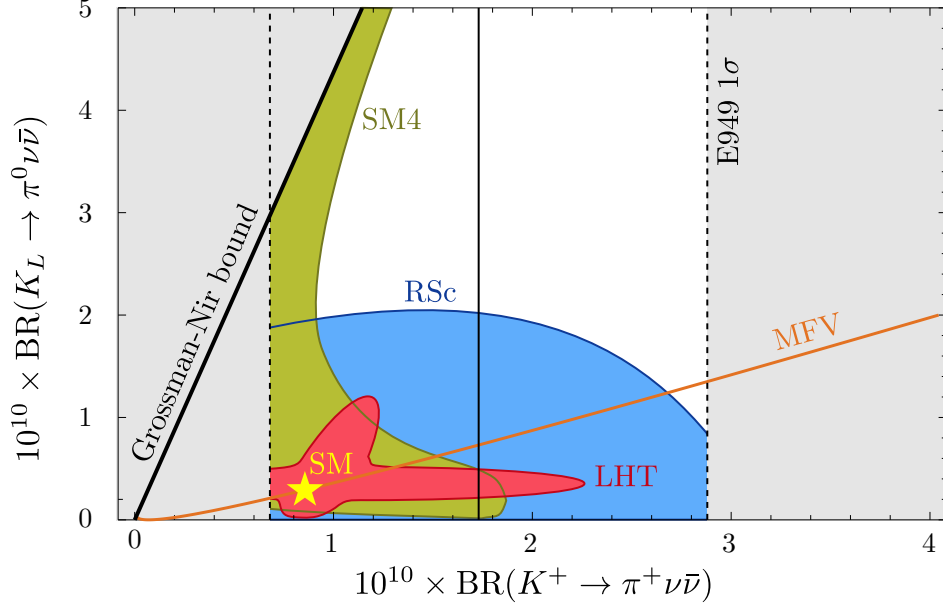


Figure 2.3: Predictions of different physics models for the branching ratios of the charged and neutral versions of $K \rightarrow \pi \nu \bar{\nu}$. The SM prediction is indicated by a yellow star. The gray regions indicate the 68% CL limits from the BNL E787/949 experiments, and the exclusion from the Grossman-Nir bound. The orange line indicates the tight constraint of minimal-flavor violation. (Other models predict similarly strong correlations between the two modes.) The red lobes show the region preferred by the Littlest Higgs model with T parity (LHT) [35]; the blue shoulder shows the region preferred by the Randall-Sundrum model with custodial protection (RSc) [36]; and the olive-green boomerang shows the region preferred by the Standard Model with a fourth sequential generation (SM4) [44]. The MSSM (with pre-LHC limits) populates most of the rest of the experimentally allowed region [50]. From Ref. [49].

There are also examples of models with two or more unseen BSM particles recoiling against the π^+ . For example, if the lightest superpartner is neutral and light enough (i.e., a neutralino $\tilde{\chi}_1^0$), the decay $K^+ \rightarrow \pi^+ \tilde{\chi}_1^0 \tilde{\chi}_1^0$ is allowed. As shown in Fig. 2.4 [62], the spectrum depends sensitively on the neutralino mass, although the predicted rates are small unless squark-mass difference are nearly as large as possible to remain consistent with bounds on other FCNCs. In general, the shape of π^+ spectrum could be distorted in a measurable way. An especially exotic example of this phenomenon is the unparticle model of Wu and Zhang [63]. This is an example of a process whose parameters are constrained by the BNL E787/949 results.

This brief summary is necessarily incomplete, but should give an accurate impression of the wide range of BSM possibility that can be accessed via measurements of $K^+ \rightarrow \pi^+ \nu \bar{\nu}$.

References

- [1] G. Buchalla and A. J. Buras, Nucl. Phys. B **548**, 309 (1999) [arXiv:hep-ph/9901288].
- [2] F. Mescia and C. Smith, Phys. Rev. D **76**, 034017 (2007) [arXiv:0705.2025 [hep-ph]].
- [3] M. Misiak and J. Urban, Phys. Lett. **B451**, 161-169 (1999) [hep-ph/9901278].

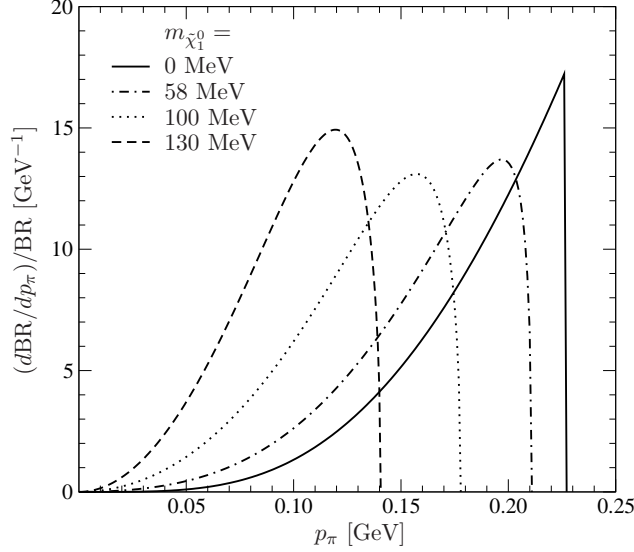


Figure 2.4: Predictions of the pion momentum spectrum for $K^+ \rightarrow \pi^+ \tilde{\chi}_1^0 \tilde{\chi}_1^0$, in SUSY with decay to pairs of neutralinos $\tilde{\chi}_1^0$ kinematically allowed. $K \rightarrow \pi \nu \bar{\nu}$ shares the endpoint of the massless case. From Ref. [62].

- [4] J. Brod and M. Gorbahn, Phys. Rev. D **78**, 034006 (2008) [arXiv:0805.4119 [hep-ph]].
- [5] A. F. Falk, A. Lewandowski, and A. A. Petrov, Phys. Lett. B **505**, 107 (2001) [arXiv:hep-ph/0012099].
- [6] G. Isidori, F. Mescia, and C. Smith, Nucl. Phys. B **718**, 319 (2005) [arXiv:hep-ph/0503107].
- [7] G. Isidori, G. Martinelli, and P. Turchetti, Phys. Lett. B **633**, 75 (2006) [arXiv:hep-lat/0506026].
- [8] J. Brod, M. Gorbahn, and E. Stamou, Phys. Rev. D **83**, 034030 (2011) [arXiv:1009.0947 [hep-ph]].
- [9] A. J. Buras, M. Gorbahn, U. Haisch, and U. Nierste, JHEP **0611**, 002 (2006) [arXiv:hep-ph/0603079].
- [10] K. G. Chetyrkin et al., Phys. Rev. D **80**, 074010 (2009) [arXiv:0907.2110 [hep-ph]].
- [11] C. McNeile, C. T. H. Davies, E. Follana, K. Hornbostel, and G. P. Lepage [HPQCD Collaboration], Phys. Rev. D **82**, 034512 (2010) [arXiv:1004.4285 [hep-lat]].
- [12] J. Bijnens and K. Ghorbani, arXiv:0711.0148 [hep-ph].
- [13] K. Nakamura et al. [Particle Data Group], J. Phys. G **37**, 075021 (2010) and 2011 partial update for the 2012 edition.
- [14] C. Bernard *et al.* [Fermilab Lattice Collaboration], Phys. Rev. D **79**, 014506 (2009) [arXiv:0808.2519 [hep-lat]].
- [15] E. Gámiz, C. T. H. Davies, G. P. Lepage, J. Shigemitsu, and M. Wingate [HPQCD Collaboration], Phys. Rev. D **80**, 014503 (2009) [arXiv:0902.1815 [hep-lat]].
- [16] C. Albertus *et al.* [RBC and UKQCD Collaborations], Phys. Rev. D **82**, 014505 (2010) [arXiv:1001.2023 [hep-lat]].

- [17] R. T. Evans *et al.* [Fermilab Lattice and MILC Collaborations], PoS **LAT2009**, 245 (2009) [arXiv:0911.5432 [hep-lat]].
- [18] C. Bouchard *et al.* [Fermilab Lattice and MILC Collaborations], PoS **LATTICE2010** 299 [arXiv:1011.2570 [hep-lat]].
- [19] C. T. H. Davies *et al.* [HPQCD, MILC, and Fermilab Lattice Collaborations], Phys. Rev. Lett. **92**, 022001 (2004) [arXiv:hep-lat/0304004].
- [20] A. Bazavov *et al.*, Rev. Mod. Phys. **82**, 1349 (2010) [arXiv:0903.3598 [hep-lat]].
- [21] <http://www.usqcd.org/>
- [22] E. Dalgic, A. Gray, M. Wingate, C. T. H. Davies, G. P. Lepage, and J. Shigemitsu, Phys. Rev. D **73**, 074502 (2006); **75**, 119906(E) (2007) [arXiv:hep-lat/0601021].
- [23] J. A. Bailey *et al.* [Fermilab Lattice Collaboration], Phys. Rev. D **79**, 054507 (2009) [arXiv:0811.3640 [hep-lat]].
- [24] B. Adeva *et al.* [LHCb Collaboration], “Roadmap for selected key measurements of LHCb,” [arXiv:0912.4179 [Unknown]].
- [25] M. Calvi [LHCb Collaboration], <http://lhcb-doc.web.cern.ch/lhcb-doc/presentations/conferencetalks/postscript/2007presentations/MCalviFlavourPhysics.pdf>
- [26] A. J. Buras, F. Schwab, and S. Uhlig, Rev. Mod. Phys. **80**, 965 (2008) [arXiv:hep-ph/0405132].
- [27] M. Blanke, A. J. Buras, D. Guadagnoli, and C. Tarantino, JHEP **0610**, 003 (2006) [arXiv:hep-ph/0604057].
- [28] U. Haisch and A. Weiler, Phys. Rev. D **76**, 074027 (2007) [arXiv:0706.2054 [hep-ph]].
- [29] T. Hurth, G. Isidori, J. F. Kamenik, and F. Mescia, Nucl. Phys. B **808**, 326 (2009) [arXiv:0807.5039 [hep-ph]].
- [30] K. -F. Chen *et al.* [Belle Collaboration], Phys. Rev. Lett. **99**, 221802 (2007) [arXiv:0707.0138 [hep-ex]].
- [31] P. del Amo Sanchez *et al.* [BaBar Collaboration], Phys. Rev. **D82**, 112002 (2010) [arXiv:1009.1529 [hep-ex]].
- [32] G. Isidori, F. Mescia, P. Paradisi, C. Smith, and S. Trine, JHEP **0608**, 064 (2006) [arXiv:hep-ph/0604074].
- [33] W. Altmannshofer, A. J. Buras, D. M. Straub, and M. Wick, JHEP **0904**, 022 (2009) [arXiv:0902.0160 [hep-ph]].
- [34] C. Promberger, S. Schatt, and F. Schwab, Phys. Rev. D **75**, 115007 (2007) [arXiv:hep-ph/0702169].
- [35] M. Blanke, A. J. Buras, B. Duling, S. Recksiegel, and C. Tarantino, Acta Phys. Polon. B **41**, 657 (2010) [arXiv:0906.5454 [hep-ph]].
- [36] M. Blanke, A. J. Buras, B. Duling, K. Gemmler, and S. Gori, JHEP **0903**, 108 (2009) [arXiv:0812.3803 [hep-ph]].
- [37] N. G. Deshpande, D. K. Ghosh, and X. G. He, Phys. Rev. D **70**, 093003 (2004) [arXiv:hep-ph/0407021].

- [38] W. F. Chang and J. N. Ng, JHEP **0212**, 077 (2002) [arXiv:hep-ph/0210414].
- [39] J. Welzel, arXiv:hep-ph/0505094.
- [40] T. Appelquist, N. D. Christensen, M. Piai and R. Shrock, Phys. Rev. D **70**, 093010 (2004) [arXiv:hep-ph/0409035].
- [41] X. G. He, J. Tandean, and G. Valencia, Phys. Rev. D **80**, 035021 (2009) [arXiv:0904.2301 [hep-ph]].
- [42] I. Doršner, S. Fajfer, J. F. Kamenik, and N. Košnik, Phys. Lett. B **682**, 67 (2009) [arXiv:0906.5585 [hep-ph]].
- [43] A. Soni, A. K. Alok, A. Giri, R. Mohanta, and S. Nandi, Phys. Lett. B **683**, 302 (2010) [arXiv:0807.1971 [hep-ph]].
- [44] A. J. Buras, B. Duling, T. Feldmann, T. Heidsieck, C. Promberger, and S. Recksiegel, JHEP **1009**, 106 (2010) [arXiv:1002.2126 [hep-ph]].
- [45] W. S. Hou and C. Y. Ma, Phys. Rev. D **82**, 036002 (2010) [arXiv:1004.2186 [hep-ph]].
- [46] C. H. Chen, C. Q. Geng, and T. C. Yuan, Phys. Rev. D **75**, 077301 (2007) [arXiv:hep-ph/0703196].
- [47] A. J. Buras and D. Guadagnoli, Phys. Rev. D **79**, 053010 (2009) [arXiv:0901.2056 [hep-ph]].
- [48] M. Blanke, Acta Phys. Polon. B **41**, 127 (2010) [arXiv:0904.2528 [hep-ph]].
- [49] D. M. Straub, “New physics correlations in rare decays,” talk presented at the 6th International Workshop on the CKM Unitarity Triangle, Warwick, UK, (September 6–10, 2010), arXiv:1012.3893 [hep-ph].
- [50] F. Mescia, quoted by G. Isidori, “KAON 2007: Conference Summary,” PoS **KAON**, 064 (2008) [arXiv:0709.2438 [hep-ph]].
- [51] A. J. Buras, T. Ewerth, S. Jäger and J. Rosiek, Nucl. Phys. B **714**, 103 (2005) [arXiv:hep-ph/0408142].
- [52] Y. Grossman, G. Isidori, and H. Murayama, Phys. Lett. B **588**, 74 (2004) [arXiv:hep-ph/0311353].
- [53] M. Hindmarsh and P. Moulatsiotis, Phys. Rev. D **59**, 055015 (1999) [arXiv:hep-ph/9807363].
- [54] F. Wilczek, Phys. Rev. Lett. **49**, 1549 (1982).
- [55] T. Banks and H. E. Haber, JHEP **0911**, 097 (2009) [arXiv:0908.2004 [hep-ph]].
- [56] D. S. Gorbunov, Nucl. Phys. B **602**, 213 (2001) [arXiv:hep-ph/0007325].
- [57] T. M. Aliev, M. I. Dobroliubov, and A. Y. Ignatiev, Nucl. Phys. B **335**, 311 (1990).
- [58] M. Pospelov, Phys. Rev. D **80**, 095002 (2009) [arXiv:0811.1030 [hep-ph]].
- [59] M. Pospelov, A. Ritz, and M. B. Voloshin, Phys. Lett. B **662**, 53 (2008) [arXiv:0711.4866 [hep-ph]].
- [60] P. Fayet, Phys. Rev. D **75**, 115017 (2007) [arXiv:hep-ph/0702176].
- [61] J. F. Gunion, D. Hooper, and B. McElrath, Phys. Rev. D **73**, 015011 (2006) [arXiv:hep-ph/0509024].

- [62] H. K. Dreiner, S. Grab, D. Koschade, M. Krämer, B. O’Leary, and U. Langenfeld, Phys. Rev. D **80**, 035018 (2009) [arXiv:0905.2051 [hep-ph]].
- [63] Y. F. Wu and D. X. Zhang, “On unparticles and $K^+ \rightarrow \pi^+ + \text{missing energy}$,” arXiv:0712.3923 [hep-ph].

3 History of $K^+ \rightarrow \pi^+ \nu \bar{\nu}$ Experiments

Searches for the $K^+ \rightarrow \pi^+ \nu \bar{\nu}$ process, which began about 40 years ago, have used stopped- K^+ beams. It was believed at the time of the first of these experiments that the branching ratio might be as high as a few $\times 10^{-5}$ [1]. It was recognized that, even at this level, a process with a poor signature such as $K^+ \rightarrow \pi^+ \nu \bar{\nu}$ would need effective particle identification, precise kinematic measurement, and the ability to veto extra charged and neutral tracks to discriminate it from common decay modes such as $K^+ \rightarrow \mu^+ \nu_\mu$ and $K^+ \rightarrow \pi^+ \pi^0$ (referred to as $K_{\mu 2}$ and $K_{\pi 2}$, respectively).

The earliest published result was from a heavy-liquid bubble chamber experiment at the Argonne Zero Gradient Synchrotron, in which a 90% CL upper limit of $\mathcal{B}(K^+ \rightarrow \pi^+ \nu \bar{\nu}) < 10^{-4}$ was obtained [2]. In that paper, $K_{\pi 2}$ decay in flight and hadronic π^+ interactions in the detector were identified as dangerous sources of potential background.

The final analysis of the Argonne experiment improved the limit to 5.7×10^{-5} [3]. However, before it appeared in print, a subsequent counter/spark-chamber experiment at the LBL Bevatron improved the limit to 1.4×10^{-6} [4]. The Bevatron experiment was sensitive to only the most energetic π^+ , whereas the bubble chamber experiment covered a wide kinematic range. In addition to backgrounds from common K^+ decay modes, this experiment considered possible backgrounds from K^+ charge exchange in the stopping target followed by $K_L^0 \rightarrow \pi^+ e^- \bar{\nu}_e$, and from beam π^+ particles that scattered into the detector. The Chicago-Berkeley group continued their program with a setup sensitive to π^+ in the kinetic energy range 60–105 MeV, *i.e.*, below that of the potential background process $K_{\pi 2}$ rather than above it. This restriction required reconfiguring their photon veto system so that it became nearly hermetic. Combining results from the two configurations, the branching ratio upper limit was improved slightly to 5.6×10^{-7} [5].

About a decade later, an experiment at the KEK Proton Synchrotron improved the limit to 1.4×10^{-7} [6]. The technique of waveform digitization to record the $\pi^+ \rightarrow \mu^+ \rightarrow e^+$ decay chain was introduced for the first time. This experiment was sensitive only to the π^+ with momenta greater than that from $K_{\pi 2}$ (referred to as the “ $\pi \nu \bar{\nu}(1)$ ” or “PNN1” region) and its setup resembled that of Ref. [4].

The BNL series of experiments was initiated in the early 1980’s. They were based on a large-acceptance solenoidal spectrometer with a hermetic photon veto situated at the end of a highly pure, very intense stopped- K^+ beam [7] from the BNL Alternating Gradient Synchrotron (AGS). The experimental signature of the $K^+ \rightarrow \pi^+ \nu \bar{\nu}$ decay was a single π^+ track with $p_{\pi^+} < 227$ MeV/ c plus no other particle from a K^+ decay. Fig. 3.1 shows momentum spectra of major decay modes of the K^+ .

The first phase of E787 in 1988-91 achieved a 90% CL upper limit on the branching ratio of 2.4×10^{-9} [9], by using data from the PNN1 region. A separate limit of 1.7×10^{-8} at 90% CL [10] was extracted from the kinematic region in which the π^+ is softer than that of the π^+ from $K_{\pi 2}$ (referred to as the “ $\pi \nu \bar{\nu}(2)$ ” (PNN2) region). This program completed the identification of backgrounds needed to reach the 10^{-10} level of sensitivity and developed methods to measure them reliably.

A major upgrade of both the beam line and the detector was undertaken between 1992 and 1994. The search for $K^+ \rightarrow \pi^+ \nu \bar{\nu}$ resumed in 1995 and continued through 1998. The limit on the branching ratio from the PNN2 region was improved by an order of magnitude to 2.2×10^{-9} at 90% CL [11], but the major output of this series of runs was the observation of two clean $K^+ \rightarrow \pi^+ \nu \bar{\nu}$ events in the PNN1 region and a measurement of the branching ratio $\mathcal{B}(K^+ \rightarrow \pi^+ \nu \bar{\nu}) = (1.57_{-0.82}^{+1.75}) \times 10^{-10}$ [12]. The BNL-E787 detector was upgraded again over the period from 1999–2001. The E949 experiment was proposed to use this detector to run for 60 weeks. After the

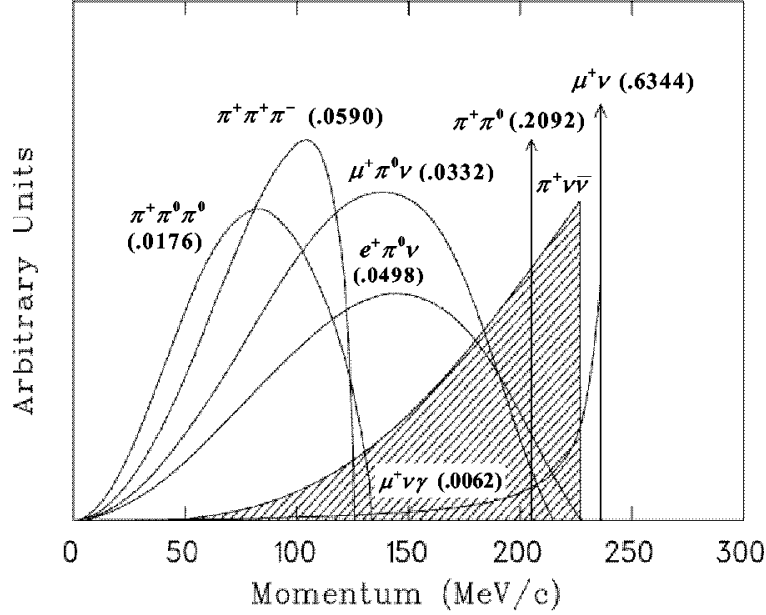


Figure 3.1: Momentum spectra (in MeV/c) of charged particles from K^+ decays in the rest frame. The values in the parentheses represent the branching ratios of the decay modes [8]. The hatched spectrum shows the π^+ momentum from $K^+ \rightarrow \pi^+ \nu \bar{\nu}$ decay assuming the $V - A$ interaction.

first 12 weeks of running in 2002, no further funds were provided to complete the experiment. Based on the collected BNL-E949 data, the first result, published in 2004 [13], reported the observation of a third event in the PNN1 region. A subsequent paper [14] provided an extended and detailed description of the detector and data analysis techniques used to produce the E949 result. The final analysis of E949 in the PNN2 region resulted in the observation of three more events and a revised branching ratio of $(1.73^{+1.15}_{-1.05}) \times 10^{-10}$ for the whole of the E787 and E949 data set [15][16].

An experiment, known as CKM, was proposed in 1998 at Fermilab to measure $K^+ \rightarrow \pi^+ \nu \bar{\nu}$ by using an in-flight technique [17]. The CKM experiment (terminated in 2004) was to use a 22-GeV SCRF-separated kaon beam produced by the Main Injector. In a new CERN experiment, NA62 [18], an in-flight technique that has a number of common features with the CKM proposal will be used. However, it will run with an un-separated charged beam, which results in significantly higher rates in some detectors. NA62 anticipates taking data for two years (100 days of running) in order to reach a sensitivity equivalent to 80 SM events. According to present plans, most of the detectors should be commissioned during a technical run in September 2012 and data taking would commence following the 2013/2014 LHC shutdown.

References

- [1] R. J. Oakes, Phys. Rev. **183**, 1520 (1969).
- [2] U. Camerini, D. Ljung, M. Sheaff and D. Cline, Phys. Rev. Lett. **23**, 326 (1969).
- [3] D. Ljung and D. Cline, Phys. Rev. D **8**, 1307 (1973).
- [4] J. H. Klems, R. H. Hildebrand, and R. Stiening, Phys. Rev. D **4**, 66 (1971).

- [5] G. D. Cable, R. H. Hildebrand, C. Y. Pang, and R. Stiening, Phys. Rev. D **8**, 3807 (1973).
- [6] Y. Asano *et al.*, Phys. Lett. B **107**, 159 (1981).
- [7] M. S. Atiya *et al.*, Nucl. Instrum. Meth. A **321**, 129 (1992).
- [8] W. M. Yao *et al.* [Particle Data Group], J. Phys. G **33**, 1 (2006).
- [9] S. C. Adler *et al.*, Phys. Rev. Lett. **76**, 1421 (1996) [arXiv:hep-ex/9510006].
- [10] M. S. Atiya *et al.*, Phys. Rev. D **48**, 1 (1993).
- [11] S. Adler *et al.*, Phys. Rev. **D70**, 037102 (2004); S. Adler *et al.*, Phys. Lett., **B537**, 211 (2002).
- [12] S. Adler *et al.*, Phys. Rev. Lett. **88**, 041803 (2002); S. Adler *et al.*, Phys. Rev. Lett. **84**, 3768 (2000); S. Adler *et al.*, Phys. Rev. Lett. **79**, 2204 (1997).
- [13] V. V. Anisimovsky *et al.*, Phys. Rev. Lett. **93**, 031801 (2004).
- [14] S. Adler *et al.* [The E949 Collaboration and E787 Collaboration], Phys. Rev. D **77**, 052003 (2008) [arXiv:0709.1000 [hep-ex]].
- [15] A. V. Artamonov *et al.* [E949 Collaboration], Phys. Rev. Lett. **101**, 191802 (2008) [arXiv:0808.2459 [hep-ex]].
- [16] A. V. Artamonov *et al.* [BNL-E949 Collaboration], Phys. Rev. D **79**, 092004 (2009) [arXiv:0903.0030 [hep-ex]].
- [17] R. Coleman *et al.* [CKM Collaboration], Fermilab Proposal 0905 (1998).
- [18] G. Anelli *et al.* [NA62 Collaboration], CERN-SPSC-2005-013, 11 June 2005.

4 Accelerator Configuration

The BNL E949 experiment was driven with 21.5-GeV/ c protons delivered with an intensity of 65×10^{12} (65 Tp) protons per 2.2-second spill in a 5.4-second cycle, corresponding to about 40 kW of average beam power. The primary beam and the secondary beam line delivered 710-MeV/ c K^+ particles to the stopping target inside the detector. Increasing the sensitivity over the E949 experiment will require a higher rate of stopping K^+ , which in turn requires higher beam power at comparable or greater beam duty factor. The conceptual design of the new K^+ beam line (described in Chapter 6) selects 600-MeV/ c charged kaons, which have a substantially higher stopping fraction in the detector. The design has the dual consequence of higher sensitivity and lower accidental background effects. The Main Injector proton source for the new experiment at Fermilab is described in Sec. 4.1, and the production target and kaon yield studies are discussed in Sec. 4.2.

4.1 The Main Injector Proton Source

For the past decade, the Main Injector has provided high-energy proton beam power to the NuMI target (300-400 kW), the anti-proton production target (90 kW), and slow-extracted beam (5 kW) to the test beam program. Following the accelerator complex shutdown in 2012, the Main Injector will drive the NO ν A program with 48×10^{12} (48 Tp) 120-GeV protons delivered to the NuMI target every 1.3 seconds, corresponding to 700 kW of beam power. Interlaced with NO ν A fast-extraction cycles, the Main Injector will drive the SeaQuest program with 10×10^{12} (10 Tp) slow-extracted protons and also the test beam program with 1×10^{12} (1 Tp) slow-extracted protons. Both SeaQuest and the test beam program will operate within a relatively-low joint duty factor of 8%.

The SeaQuest experiment will be the next step toward re-establishing high-power slow-extracted beam at Fermilab. The Tevatron fixed target program was driven by up to 10 Tp of slow-extracted protons with high duty factor (30-50)% and minimal instantaneous variation. The BNL AGS achieved routine production running of 65 Tp of slow-extracted beam with a 40% duty factor and good control of instantaneous variations. Achieving this performance required that beam-extraction losses be limited to less than 2%. The J-PARC 30-GeV proton synchrotron has further developed the state of the slow-extraction art by now controlling losses to less than the 1%.

Reaching the ORKA sensitivity requires 50-75 kW of slow-extracted Main Injector beam with 48 Tp per pulse at a duty factor of 35–45%. The optimum slow-extraction beam energy is discussed in Sec. 4.1.1. Development will be required to achieve this slow-extraction performance from the Main Injector. There is sufficient precedence with the Fermilab Tevatron, the BNL AGS, and now the J-PARC Main Ring to expect that this performance can be achieved with limited technical risk following production running of SeaQuest at 10 Tp and a commissioning period with steps in intensity toward 48 Tp of slow-extracted beam per cycle.

4.1.1 Accelerator Operating Scenario and Beam Power

Operating the Main Injector in a “mixed mode” with interlaced fast and slow-extraction cycles is routine, and will be further developed with coincident operation of NO ν A, SeaQuest, and the test beam program. The Main Injector magnet power systems can sustain up to 4800 Amps (rms), which imposes a constraint on the configuration of mixed-mode operation. Dedicated NO ν A operations with 1.3-second cycles at 120 GeV corresponds to 4200 Amps (rms), whereas a dedicated (100% duty factor) slow-extraction flattop at 87 GeV saturates the 4800 Amp (rms) limit [3]. The quadrature

sum of the slow-extraction and fast-extraction magnet currents is then [3]:

$$I = \sqrt{(1.16 \times (t + 0.433 \text{ sec})/T) \times ((E/(87.0 \text{ GeV})) \times (4800 \text{ A}))^2 + ((T - t - 1.3 \text{ sec})/T) \times (4200 \text{ A})^2}, \quad (18)$$

where t is the duration of the slow-extraction flattop, T is the cycle time, E is the beam energy, and 1.3 seconds is the sum of the Main Injector up-ramp and down-ramp durations. The 1.16 coefficient and 0.433 second offset are appropriate rms average terms of the slow-extraction component of the cycle. The interplay of fast-extraction cycles, slow-extraction beam energy, flattop, cycle time, and duty factor at a fixed total current of 4800 A (rms) is shown in Table 4.1.

Table 4.1: Relationship between beam energy, cycle time, flattop, duty factor, and beam power with a 4800 A (rms) magnet power bus constraint. The proposed operating proton beam energy of 95 GeV is highlighted with bold face.

$E_{\text{beam}}[\text{GeV}]$	$T_{\text{cycle}}[\text{s}]$	t_{flattop}	Duty Factor [%]	$P_{\text{ave}}[\text{kW}]$	$P_{\text{max}}[\text{kW}]$
120	15	2.5	16	62	377
120	20	3.3	16	46	283
120	25	4.1	16	38	232
120	30	4.9	16	31	189
100	10	3.5	35	77	222
100	15	5.0	33	52	154
100	20	6.5	33	39	118
100	25	8.1	32	31	96
95	10	4.4	44	74	166
95	15	6.3	42	49	116
95	20	8.3	41	37	89
95	25	10.1	40	29	73
90	10	5.9	59	70	118
90	15	8.3	56	46	83
90	20	10.8	54	33	61
90	25	13.3	53	28	52

4.1.2 Establishing a High Power Slow Spill Program

Commissioning the Main Injector slow-extraction systems following the 2012 shutdown will be necessary for the continued success of the MTest test beam facility and the SeaQuest experiment. Both of these programs are driven by the “Switchyard-120” complex that transports beam from the Main Injection extraction point to these fixed target areas. Main Injector beam is extracted near the F0-Tevatron point and transported to the A0-Tevatron point through a set of original main ring magnets referred to as the “main-ring remnant”. Main Injector beam is then carried from A0 to the Switchyard and subsequent beam lines to MTest and SeaQuest.

If ORKA is sited in the SeaQuest hall (NM4), then the existing beam transport to NM4 could be employed. Part of the beam transport to NM4 may require additional radiation shielding to transport the 75-kW beam. If ORKA is sited in the B0 collision hall, then additional main ring magnets and beam line must be installed from A0 and B0 in the Tevatron tunnel. The Tevatron tunnel shielding should be adequate for 75-kW beam transport, but this should be verified with detailed radiation safety studies. In addition to the A0–B0 beam transport, a Lambertson magnet

or switching dipole will be necessary at A0 to toggle beam between the Switchyard-120 program and the ORKA experiment at B0.

4.1.3 Operational Considerations

The powered elements of the beam transport from the Main Injector to the ORKA experiment will need to operate with the same duty factor as the Main Injector during production running. ORKA has optimal sensitivity with Main Injector beam energy in the 90–100 GeV range. The main-ring magnets that compose the beam transport to the experiment were designed to operate at 400 GeV, so these magnets should be able to operate at 95 GeV/ c comfortably with a high duty factor.

4.1.4 Proton Source Summary

After development and commissioning, operation of ORKA in the NO ν A era would be technically straightforward with beam sharing among the Main Injector suite of experiments being subject to program planning. The required slow-extraction beam performance was routinely achieved by BNL-AGS production running, and there is now an active community of slow-extraction experts at J-PARC and CERN which can be called on to critically review slow-extraction designs and plans at Fermilab.

The ORKA experiment would begin commissioning with low-duty-factor beam after several years of NO ν A operation and will have negligible impact on the NO ν A sensitivity. Following commissioning, the experiment would require relatively high-duty-factor (35–45%) beam. During NuMI beam-line downtime, the experiment would benefit greatly by dedicated running at a high duty factor (60%) that would be possible in the absence of fast-extraction cycles. It is worth mentioning that the 8-GeV Booster research program would likewise benefit from insertion of the proposed slow-extraction cycle during which Booster beam can be dedicated to the 8-GeV program.

4.2 Target Yield Studies and Performance Requirements

The proton beam extracted from the Main Injector impinges on a production target to produce forward ($\theta < 100$ mrad) low-energy K^+ for the secondary beam line. The optimal target to produce forward low- x_F (Feynmann- x) kaons should have high- Z material where secondary interactions in the target increase the low-momentum kaon yield by 20-30%. High- Z targets are also relatively compact, which minimizes aberrations in the K^+ beam-line optics. The E949 experiment operated with a 6-cm-long (0.7 interaction-length) platinum target at 40 kW in thermal contact with a water-cooled copper heat sink. The optics of the ORKA K^+ beam line is designed to accept kaons from a longer, 8-cm platinum target in order to increase the yield. The beam power on the ORKA target is expected to be about 50–75 kW, somewhat higher than the BNL E949 beam power. This power level can likely be maintained with the BNL E949 cooling scheme. A conceptual design for a higher power platinum target (in excess of 50 kW) was developed for the KOPIO initiative [1] and is illustrated in Fig. 4.1. It could be pursued if necessary. A study of the deposited energy and kaon yield as a function of target width is summarized in Table 4.2 which shows that the transverse dimension of the target is optimized at about 4 times the transverse dimension of the beam.

The relative yield of low-energy charged pions and kaons from thick high- Z targets at high energy (95-GeV/ c beam) compared to E949 has been estimated with two different simulation codes: MARS default(v15) [6], and the Los Alamos Quark Gluon String Model (LAQGSM-MARS) [7]. Both of

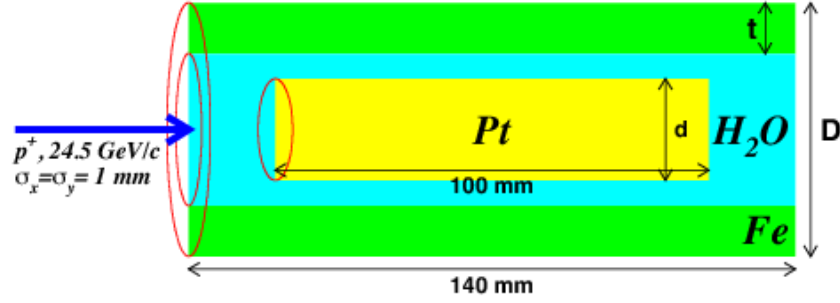


Figure 4.1: Illustration of the KOPIO target concept [1].

Table 4.2: Energy deposition study and target yield study (Eff) as a function of transverse dimensions [2].

Target dimensions (mm)				Deposited Energy (kJ/10 ¹⁴ p)					
				GEANT-GHEISHA			GEANT-FLUKA		
d	D	t	Eff.	Pt	H ₂ O	Fe	Pt	H ₂ O	Fe
2	none		0.39	4.0	0.0	0.0	6.1	0.0	0.0
2	10	0.5	0.39	4.1	0.9	0.5	6.6	1.1	0.5
3	10	0.5	0.68	10.0	1.0	0.8	15.1	1.2	0.9
4	10	0.5	0.86	17.0	1.0	1.0	24.8	1.1	1.1
5	10	0.5	0.96	22.9	0.9	1.1	35.6	1.0	1.2
4	20	0.5	0.86	17.1	2.3	0.8	24.6	2.5	0.8
4	30	0.5	0.86	17.0	3.2	0.6	24.5	3.4	0.6
4	10	1.0	0.86	16.8	0.9	2.0	24.4	1.0	2.4
4	10	2.0	0.86	17.0	0.6	4.5	24.7	0.6	5.2

these simulation codes fully simulate shower propagation through a thick target. The LAQGSM-MARS charged kaon yield estimate per proton for the E949 experiment and 95-GeV/ c is shown in Fig. 4.2. Unfortunately, there are few data on low- x_F (0.3–3)% forward production of kaons and pions to calibrate the absolute prediction of these models. Data from different beam energies and higher x_F experiments has been studied and indicate that these models predict the absolute yield within a factor of 2 of projected data and each other.

In contrast to the variation in absolute yield estimates, the relative yields are in good agreement between the two models. Defining the ratio R :

$$R = (95\text{-GeV}/c \text{ yield into } K^+ \text{ beamline}) / (E949 \text{ yield into } K^+ \text{ beamline}) . \quad (19)$$

Table 4.3: Estimates of relative K^+ yield between BNL-E949 and the 95-GeV/ c yield point.

Simulation Code	R (relative K^+ production yield)
LAQGSM-MARS	7.09 ± 0.65
MARS-default	5.97 ± 0.46

The two models give reasonably consistent predictions for the relative yield R . The mean value of R between the models will be used for sensitivity estimates with an uncertainty that spans the two models.

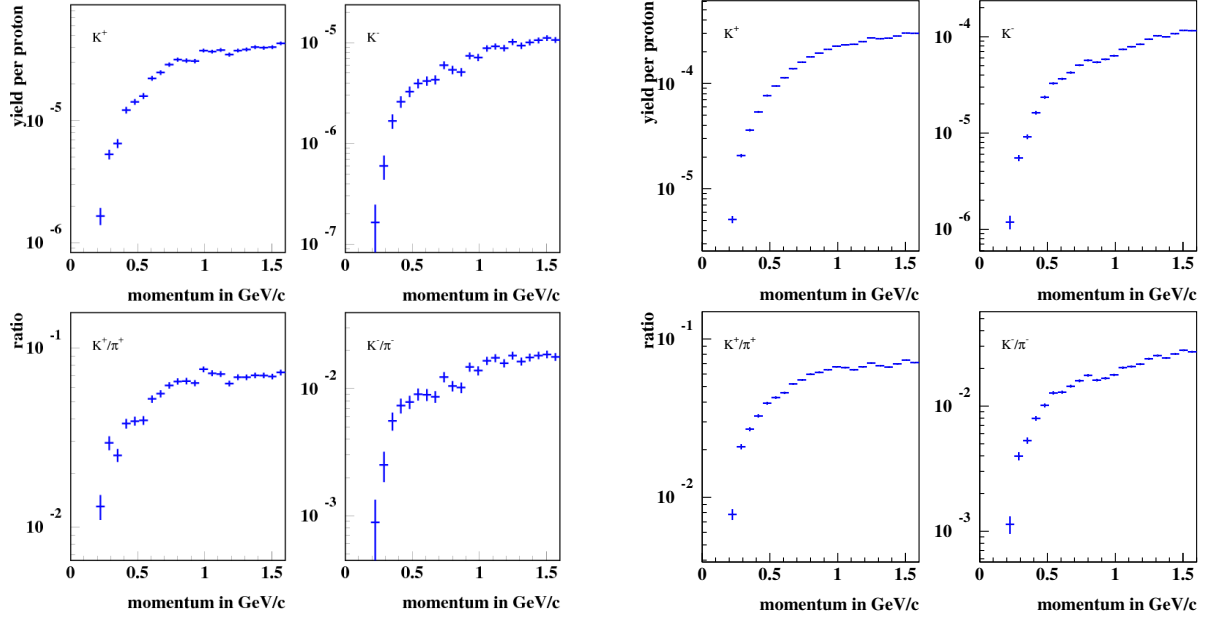


Figure 4.2: LAQGSM-MARS K^+ yields and K^+/π^+ ratios for 21.5-GeV/ c protons on a 6-cm Pt target into 12 msr (BNL-E949) on left, and for 95-GeV/ c protons on a 8-cm Pt target into 20 msr on right.

References

- [1] D. Bryman, e-print arXiv:hep-ex/0206072. See also <http://www.kopio.bnl.gov/> .
- [2] A. Poblaguev, KOPIO Technote TN056, available at <http://pubweb.bnl.gov/users/litt/www/e926/technotes/tn056.pdf> .
- [3] Personal communication with Ioanis Kourbanis, Fermilab Main Injector department head.
- [4] N.V. Mokhov, “The Mars Code System User’s Guide,” Fermilab-FN-628 (1995); N.V. Mokhov, S.I. Striganov, “MARS15 Overview,” in Proc. of Hadronic Shower Simulation Workshop, Fermilab, September 2006, AIP Conf. Proc. 896, pp. 50-60 (2007). See also <http://www-ap.fnl.gov/MARS/>
- [5] S.G. Mashnik *et al.*, “CEM03.03 and LAQGSM03.03 Event Generators for the MCNP6, MCNPX and MARS15 Transport Codes,” LANL Report LA-UR-08-2931 (2008); arXiv:0805.0751v1 [nucl-th] 6 May 2008.

5 Experiment Siting Options

There are several possible sites for ORKA. In order to control capital costs, we have considered only siting options that reuse existing buildings and beam-line enclosures and which do not excessively complicate other planned projects. Three siting options will be discussed: the CDF Collision Hall at B0, the Meson Detector Building (MDB), and NM4 (the site of KTeV and now SeaQuest). These sites are shown in an aerial view of the accelerator complex in Fig. 5.1, with an expanded view in Fig. 5.2.

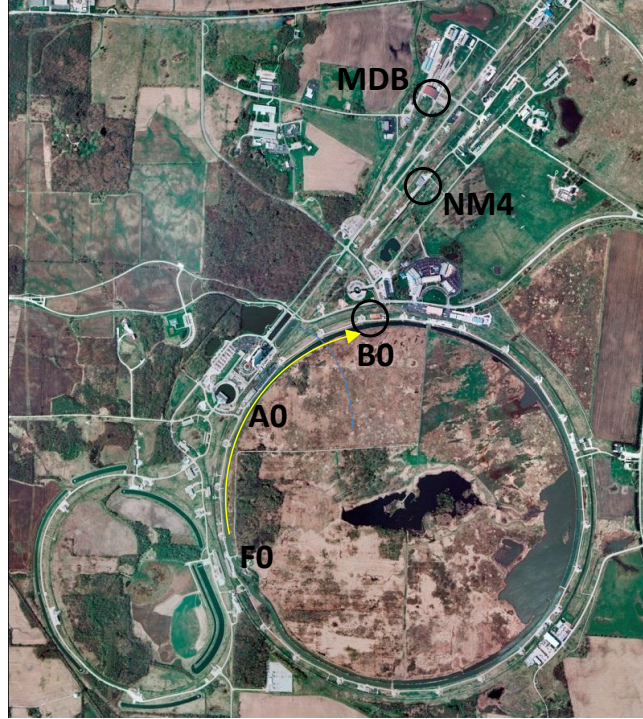


Figure 5.1: Aerial view of the accelerator complex with possible ORKA sites circled.

5.1 Re-use of the CDF Collision Hall

The most promising option appears to be transport of the Main Injector beam around the Main Ring/Tevatron tunnel to a K^+ production target in the CDF collision hall. The ORKA spectrometer would reuse the CDF solenoid magnet. A new beam line would be built (with re-use of main ring dipole and quadrupole magnets) to transport the Main Injector beam from the Tevatron A0 point to a K^+ production target in the collision hall. A two-way split would need to be added to the “main ring remnant” at A0 to allow beam to be delivered to the fixed target area as well as to the Tevatron B0 point.

The Tevatron beam line is located near the outer radius of the Main Ring tunnel. A new beam line could be located near the inside of the tunnel. This beam line would enter the CDF collision hall at least 6 feet south of the center of the building. The K^+ production target would be located approximately 28 feet west of the center of the CDF collision hall. A short beam line (described

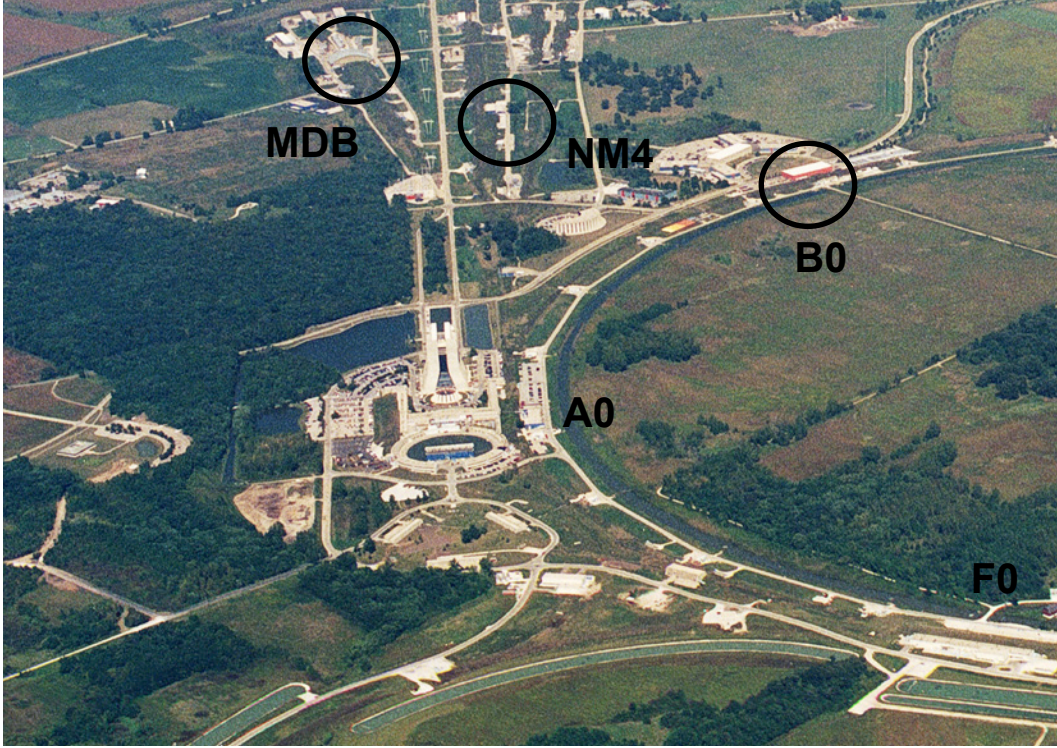


Figure 5.2: Experiment siting options. Beam is extracted at F0 and either transported in the Main Ring/Tevatron tunnel to B0, or to one of two locations in the Fixed Target Area.

in Chapter 6) would bend the K^+ beam through 90° . The detector (Chapter 7) would be located in the “access passage” between the CDF collision and assembly halls. The uninteracted proton beam would be dumped in the collision hall. Figure 5.3 illustrates this siting option. The beam dump in the figure has a dimension equal to that of the NuMI absorber, which was designed for 65 kW and qualified for one hour at 400 kW.

We have also begun to explore a second layout for the experiment in the CDF collision hall. In this case, the low energy K^+ beam would be modified by reducing the bend angle of the momentum-selecting dipole magnet from 45° to approximately 30° , and reversing the polarity of the final dipole so that the beam has a dog-leg configuration rather than a right angle bend. With this configuration, the experiment would fit in the collision hall with the shield wall in its current closed location. The solenoid magnet would not need to be rotated from its current position, but only moved 10 feet towards the shield wall. This layout would necessitate only the removal of the northern muon wall and arches. Further study is required to determine whether or not this configuration can yield a suitable K^+ beam, but it appears to be a very promising option. ORKA will pursue this re-design with high priority which, if realized, will preserve the CDF detector in the current orientation with respect to the tunnel and collision hall.

5.2 Siting the Experiment in the Meson Detector Building

The primary proton beam could be transported through one of the Meson beam lines (probably MCenter) to the Meson Detector Building. Due to the concrete installed to shield the RF test area in MEast, there is not enough floor space in the Meson Detector Building to accommodate

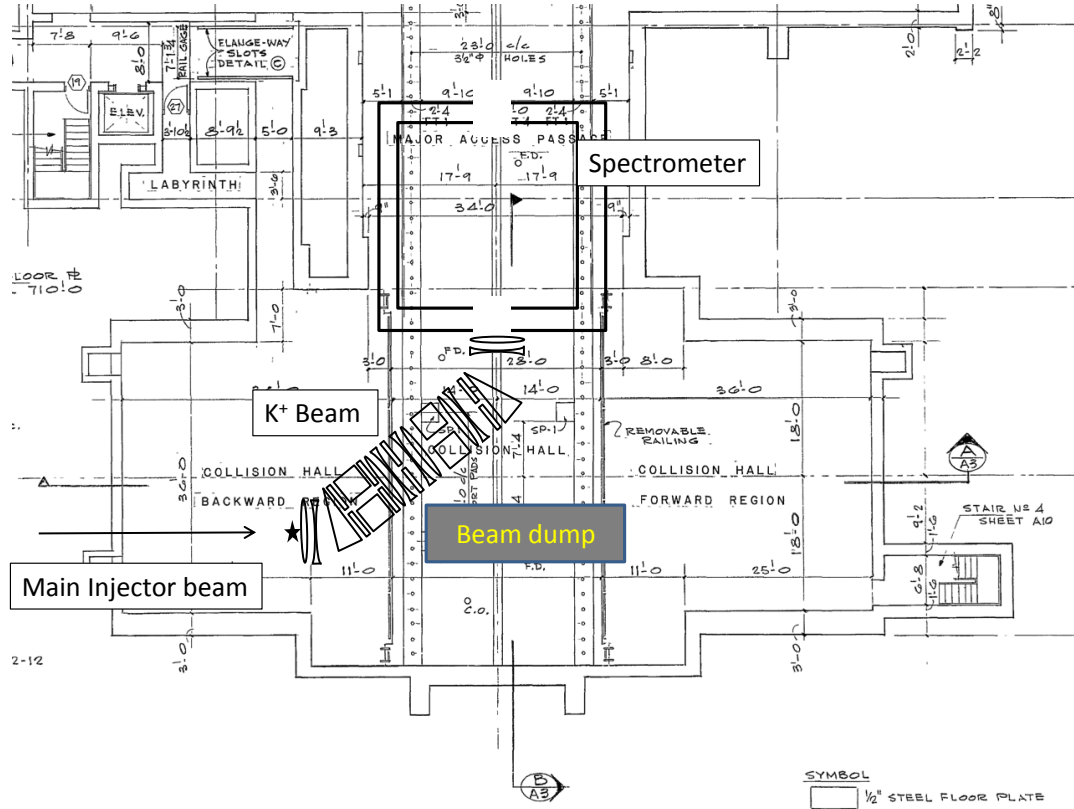


Figure 5.3: Illustration of the ORKA beam line and detector sited within the B0 collision hall.

the ORKA experiment and the low energy beam line described in Chapter 6 without modification. If a dog-leg configuration were used (as described above), the experiment could be located in the center of the building. However, it is not likely that this siting would allow continued use of the planned MCenter test beam.

The Meson beam lines would need to be upgraded in order to transport a high-intensity Main Injector beam with acceptable losses. Beam extracted through the switchyard to the Meson Test Facility is currently limited to 1.2×10^{13} protons/hour as measured by the MW1 SEM. A plan to add a number of focusing magnets to the primary beam transport upstream of the Meson target train was developed as part of the SY120 project, but was dropped to save money. Currently, there are electrostatic septa in enclosure F1 that initiate a three-way (vertical) split of the Meson beams. Lambertson magnets approximately 475 m downstream in enclosure M01 separate up to three beams horizontally, and the beams pass through three holes in the Meson target train at the downstream end of M01. (When four beams were run in Meson, the MTest beam was split off of MWest downstream of the target train). The three beams drift another approximately 200 m to enclosure M02. No focusing element exists between F1 and M02.

As stated above, the Switchyard 120 Conceptual Design Report [1] contains a plan to add quadrupole magnets in the F enclosures and M01. It was also anticipated that the Meson septa would be moved to the upstream end of enclosure M01. The report notes that “this location will necessitate moving almost all beam-line elements in Enclosures M01 and M02 as well as modifying the Meson target train.” A second lattice was proposed in 2005 [2], with the beam requirements of E906 in mind. This design was intended to reduce the losses in the upstream Meson enclosures even more than

would have been the case for the unimplemented SY120 design. A rough estimate of how much it would cost to implement the more recent design for the upstream end of Meson was made in June 2005. The estimated total cost was \$725k. The bulk of this cost was for rigging, pipefitting, and electrical work. It should also be noted that the E906 experiment assumes an exposure of 5.2×10^{18} protons in two years. This value is substantially less than required for ORKA.

The superconducting RF R&D program located in MEast currently uses all of the cryogenic infrastructure that exists in the Meson area. ORKA would require additional cryogenic infrastructure for its superconducting solenoid.

5.3 Siting the Experiment at SeaQuest Hall (the old KTeV Hall; NM4)

The E906 experiment (SeaQuest) is scheduled to run in the old KTeV hall (NM4) in the 2013-2015 time frame, in advance of ORKA commissioning. The transport of primary protons to NM4 would need to be reviewed in light of the required increase in intensity, but is likely possible.

The NM4 enclosure has good modern electrical and water services. However, the building has even less space transverse to the primary proton beam line than the CDF assembly hall. A dog-leg configuration would be required, and the optimization of the low-energy K^+ beam might be more problematic than if the experiment were sited either in the CDF collision hall or in the Meson Detector Building.

NM4 also does not have the cryogenic infrastructure that would be required by a superconducting solenoid spectrometer magnet.

References

- [1] FERMILAB-TM-2014.
- [2] FERMILAB-TM-2324-AD

6 Secondary Beam Line

After production of kaons in the primary target, the secondary beam line provides a clean, momentum-analyzed beam of K^+ particles that are stopped in a scintillator fiber target. A much larger production of π^+ particles must be suppressed, and the overall length of the beam line must be kept as short as possible to minimize losses due to in-flight decays. There are other tradeoffs between the choice of nominal beam momentum and the loss of flux due to interactions and out-scattering from degraders within the detector portion of the beam line.

The design of a separated low-momentum K^+ beam for the experiment and possible choices for degrading and stopping the kaons in the experiment target are discussed in this section.

6.1 A Separated K^+ Beam

The K^+ particles produced at the production target will be transported through a beam line that is designed to select those with momenta in the 550-600 MeV/ c range. The optimum operating point within this range is discussed below. The overall layout of the beam channel and the beam envelopes are shown in Fig. 6.1. Also shown along with the beam envelopes is the dispersion in units of cm per percent $\Delta P/P$.

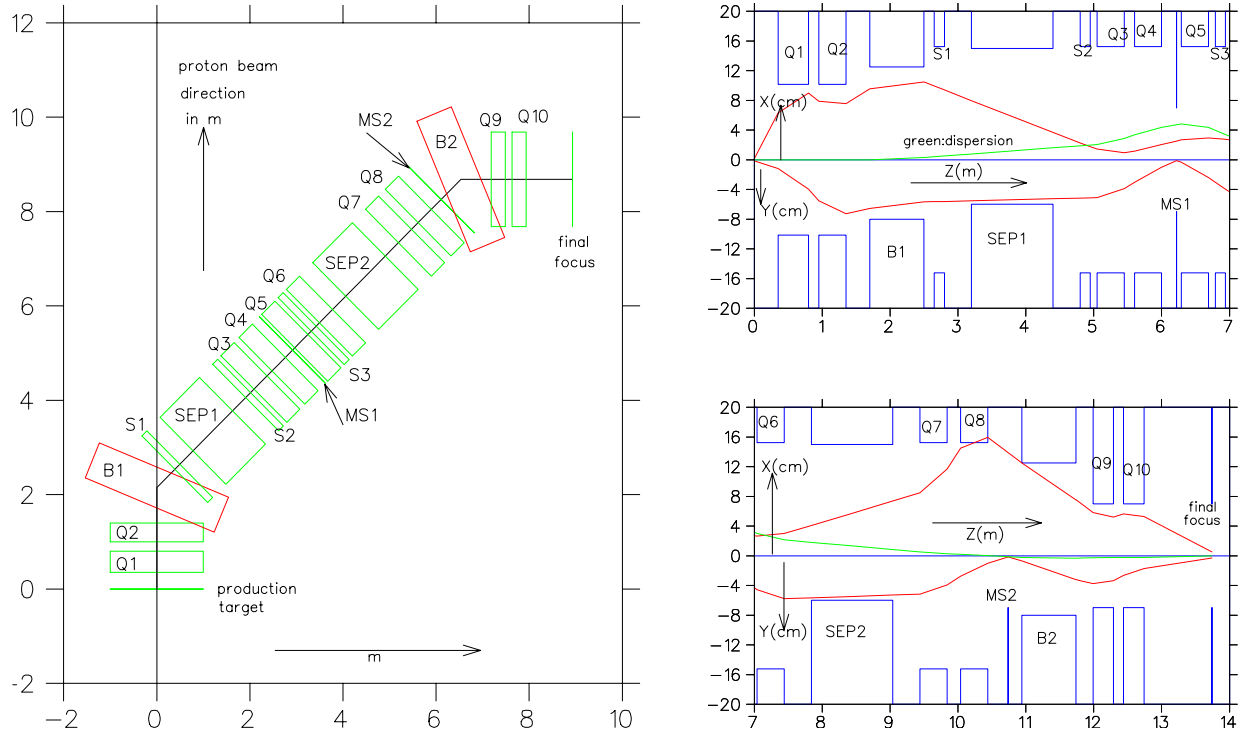


Figure 6.1: Left: The beam-line layout. Right: The beam envelopes.

The beam line is 13.74 m long, including a 1.0-m drift after the last quadrupole. The ratio of production of pions to kaons is 23. This ratio increases by a factor 18 to a value of 400 at the final focus due to decay. Thus, a 0.1% transmission of pions corresponds to a pion contamination fraction of 0.40 at the experiment target.

There are two crossed-field separators, each 1.2 m long with an electric gradient of 50 kV/cm, or 600 kV over a 12-cm vertical gap. The K^+ and π^+ separation is done in two stages by two slits MS1 and MS2 that together remove 99% of the pions. The remaining 1% pions, corresponding to four times the kaon rate, are removed by a fixed piece of beam blocker in Q8.

Experiment E949 at BNL was done at LESB-III, a 19.6-m-long beam line, first at 800 MeV/ c and later at 710 MeV/ c . The angular acceptance was 12 msr, and the momentum bite was 4%, for a total acceptance of 48 msr-%. The kaon survival fraction was 2.52%.

In the current design for the Fermilab experiment, the angular acceptance is 20 msr and the momentum bite is 6%, for a total acceptance of 120 msr-%. The overall acceptance is thus improved by a factor 2.5. The kaon survival rate is now 5.36% (for 600 MeV/ c momentum), a factor of 1.44 improvement over the 710-MeV/ c case for LESB-III.

The length of the production target assumed for the design was 6 cm. It is possible to use an 8-cm target, but MS2 would have to be closed further at the expense of some kaon rate. The net increase in intensity compared to a 6-cm target is estimated to be about 12%.

An important reason for having two stages is the cloud pion problem. They originate in the decay of other particles produced in the production target, and present a large vertical source to the channel. The MS1 slit redefines this source for the second stage. The two mass slits together successfully remove most of the cloud pions.

Pions decay into muons. Because MS1 stops 80% of the pions, they can no longer decay into muons further downstream. The muon contamination at the experiment target is therefore negligible.

6.1.1 Layout and Optics

The beam-line elements are listed in Tables 6.1 and 6.2. The secondary beam is selected at zero degrees to the proton beam from a 8-cm-long production target. The doublet Q1–Q2 catches the beam and focuses it through bending magnet B1. The beam is vertically parallel in the first separator. The B1 magnet is a 38° sector magnet which bends the beam 45° . The negative poleface entrance and exit angles of -3.5° enhance the horizontal focusing of B1. Therefore, the strength of Q1 can be reduced. This design results in a larger vertical-angle acceptance.

After passing through the Q3 and Q4 quadrupoles, the beam has a vertical focus at the first mass slit MS1. In order to make the beam line short, the distance between the Q4 and Q5 quadrupoles is only 29 cm. The MS1 slit is 22 cm from Q4, and 7 cm from Q5. It is not possible to put a variable slit here. It has to be a fixed vertical aperture with a width of 6 mm. The doublet Q5–Q6 steers the beam through the second separator, where the beam is vertically parallel. Quadrupole Q7 focuses the beam vertically at the second mass slit MS2. The Q7 and Q8 quadrupoles together also steer the beam through the 45° bending magnet B2. This parallel-faced bending magnet has entrance and exit poleface angles of 22.5° . The short 7-inch-diameter doublet Q9–Q10 provides a final horizontal and vertical focus 1.0 m downstream of Q10. The beam is nearly achromatic in both angle and position.

Second-order aberrations have been corrected with 3 sextupoles. Third-order aberrations have been left uncorrected.

Table 6.1: Beamline elements, and poletip fields.

element	length (cm)	pole radius (cm)	design pole field (kG)
Quadrupole			
Q1	45.0	10.16	12.43
Q2	40.0	10.16	-8.58
Q3	40.0	15.24	-7.71
Q4	40.0	15.24	3.35
Q5	40.0	15.24	7.81
Q6	40.0	15.24	-8.36
Q7	40.0	15.24	-8.06
Q8	40.0	15.24	9.16
Q9	30.0	8.89	-10.56
Q10	30.0	8.89	8.56
Sextupole			
S1	15.0	15.24	2.28
S2	15.0	15.24	-3.60
S3	15.0	12.24	-1.91

Table 6.2: Dipole and separator characteristics.

	entr/exit angle to pole face (deg)	length (cm)	pole gap (cm)	field (kG)	bend angle (deg)
dipole					
B1	-3.5/-3.5	80.0	8.89	18.01	45.0
B2	22.5/22.5	80.0	7.62	18.01	45.0
separator	length (m)	plate width (cm)	plate gap (cm)	plate gap voltage (kV)	magnetic field (kG)
SEP1	1.20	30	12.00	600	0.224
SEP2	1.20	30	12.00	600	0.224

6.1.2 Results of Monte Carlo Calculations

Monte Carlo calculations of the beam were done with the high-order ray-tracing program ZGOUBI. The performance of the kaon beam is given for the case that MS1 is 6 mm wide and MS2 has an aperture of 8 mm. The momentum acceptance from the production target, beam-spot distributions at the focal plane, and the beam divergence at the focal plane are shown in Fig. 6.2.

The pion component of the beam can be a serious concern, but is also easily compensated. The vertical pion and kaon beam spots at MS1 and MS2 are shown in Fig. 6.3 (left). The pion tails sneak under the kaon spots. About 1% of the pions pass through the mass slits. The X-Y distribution of the blue kaons and the red pions that pass through the two mass slits are shown in Fig. 6.3 (right). The pions can be removed by a beam blocker piece in a corner of Q8.

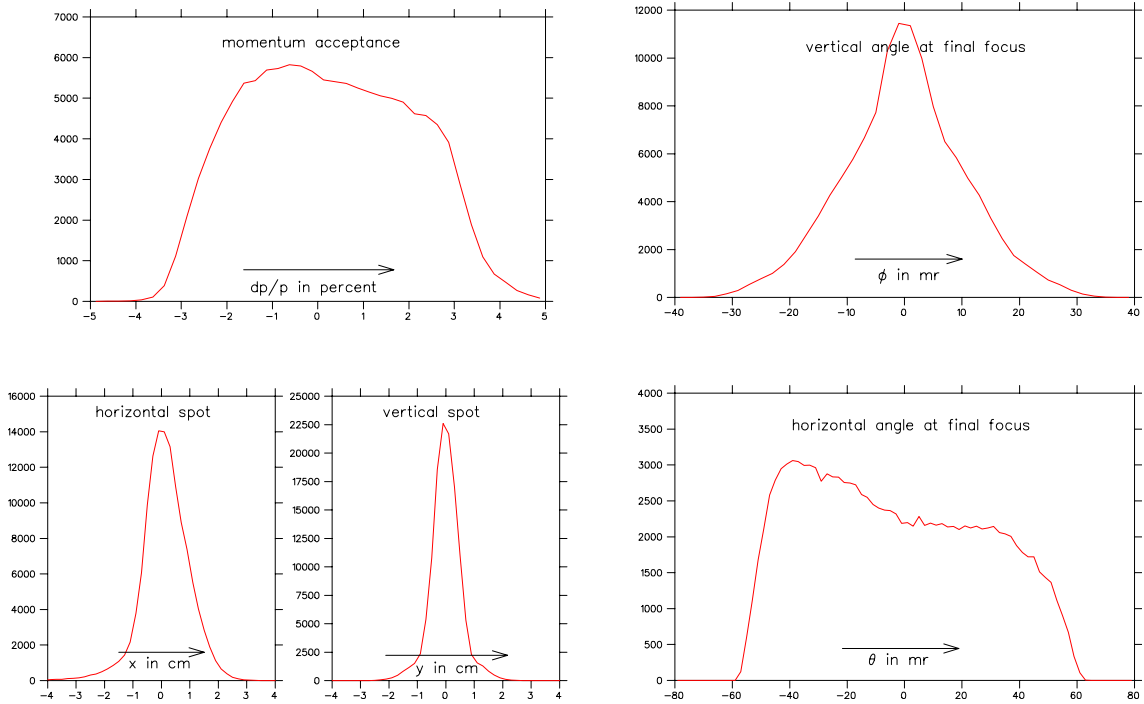


Figure 6.2: Left: The momentum acceptance (top) and the spot sizes at the focal plane (bottom). Right: The beam divergences at the focal plane

6.2 Beamline Degraders

The beam line described above, illustrated for 550 MeV/c, will be run at 600 MeV/c. After the beam leaves the Q10 quadrupole, it must be degraded so that the K^+ stop soon after they enter a scintillating target. A set of Monte Carlo calculations has been done to assist in selecting the best beam momentum and degrader, considering in-flight decays through the 1.0-m drift distance, interactions in the materials, and out-scattering from degraders and the target.

The calculations were made with the standalone code FLUKA [1], which is distributed as binary libraries for GNU/Linux systems. Hooks are available for user routines. It is derived from the old GEANT3-FLUKA code, with substantial recoding and numerous extensions. All simulations made use of the PRECISION set of defaults. Generally, these defaults include an extensive set of

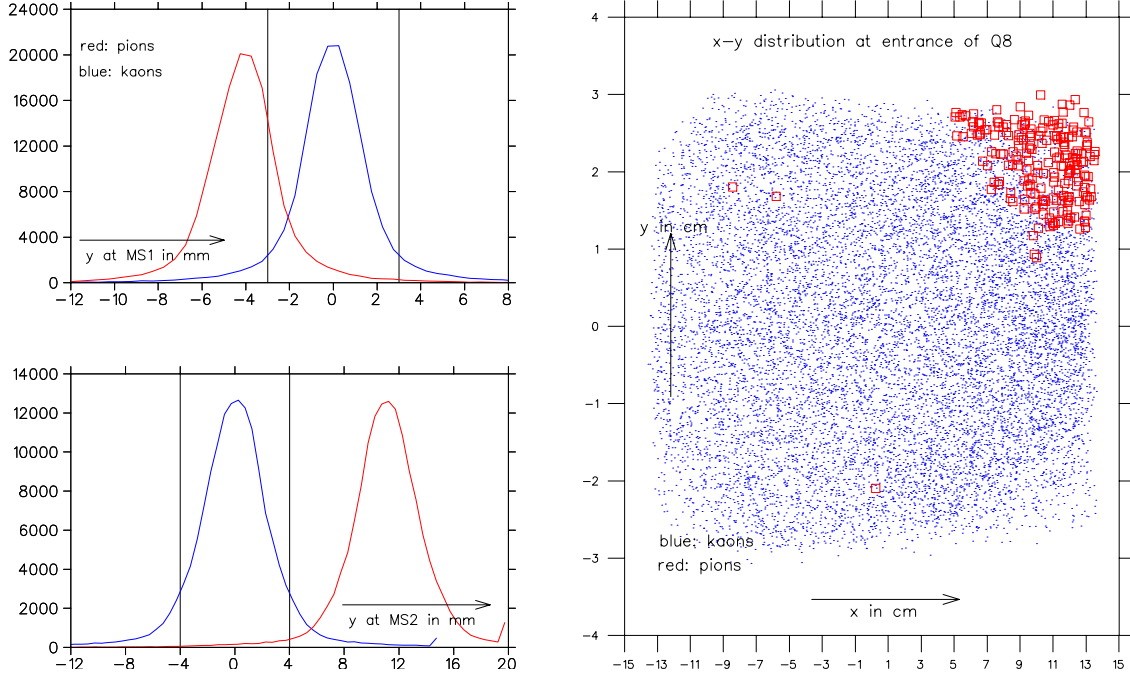


Figure 6.3: Left: Vertical kaon and pion spots at the mass slits. Right: Kaon and pion scatter plot at the entrance of Q8 for those particles transmitted through the mass slits when MS1 is 6 mm wide and MS2 has 8 mm aperture.

electromagnetic processes, including photon and muon photonuclear processes, and tracking for most particles down to 100 keV. Neutrons are tracked down to 20 MeV, and then handled in a logarithmic scale of energies down to low thermal energies. Hadronic interactions are modeled through a set of well-tested algorithms.

6.2.1 Beamline and Logic

In these calculations, the target was taken to be a cylinder of scintillator material of radius 6 cm and sufficient length. It was placed to start at $Z = 0$. Several options for degrading materials were used. All degraders, also 6 cm in radius, were placed immediately upstream of the target. The target and degrader were placed inside a cylindrical ‘sides’ region. An ‘end’ region was also placed at the far end of the target. A particle that crossed the boundary from the target or beam-line region (which holds the degrader) into one of the regions was recorded as having ‘escaped.’

Within the target and degrader regions, stopped K^+ particles were identified as those that tracked until they had a momentum $p_K = 0$. Those that decayed in-flight along the way were identified with an internal code number that indicated the production of secondaries from decay, and which also had non-zero momentum. (The requirement of non-zero momentum was needed to prevent K^+ particles which stopped and then decayed from being double-counted.) Finally, K^+ particles that interacted with nuclei and disappeared were identified with a second internal code number for production of secondaries. The list of secondaries was scanned, and the K^+ was identified as ‘interacted’ if there was no such particle in the list. There are thus four classes of K^+ events: stopped, decayed, interacted, and escaped. The total number of kaons in these groups was about 99.5% of the beam.

A beam file that contained a list of X and Y coordinates, their respective divergences, and momenta for rays computed at 1.0 meters from the end of Q10 was available from the design of the separated beam line. It was used for all calculations, with the rays back-traced to a specified starting point in the beam line.

6.2.2 Degraders and Yields

To conform to the features of the E949 experiment [2], the criterion was adopted that the stopped K^+ peak should be near 12 cm into the target scintillator. A momentum of about 335 MeV/ c at the entrance to the target is needed to satisfy the criterion. In addition to BeO and diamond used in previous studies at 550 MeV/ c , SiO₂ (silica, quartz) and Al₂O₃ were also studied as degrader materials at 600 MeV/ c .

Initial studies focused on the effects of different degrader materials, and the initial beam position was set just upstream of the respective degrader. For comparisons under more realistic conditions, including decays along the beam line, a common starting point is needed. This point was taken to be the upstream end of the scintillator degrader at 550 MeV/ c , and was at $Z = -41$ cm. Results for some key numbers are shown in Table 6.3.

Table 6.3: Distributions of K^+ particles in various regions, for 100,000 beam particles. The common beam-line segment for all cases starts at $Z = -41$ cm. The degrader thickness is in units of cm. The numbers in the Target columns are totals for that region.

Momen.	Degrader	Dgrdr Thick.	Stopped K^+		Decayed K^+		Interact. Dgrdr	Escaped	
			Dgrdr	Target	Dgrdr	Target		Dgrdr	Target
550	Scint	41.0	5,934	60,464	10,757	4,834	4,083	9,808	2,752
550	BeO	16.4	11,172	61,112	10,097	4,680	5,555	3,174	3,392
550	Diamd	13.4	12,085	62,744	10,035	4,565	5,190	2,192	2,787
600	BeO	21.8	13,433	55,289	9,276	4,172	7,133	6,235	3,534
600	SiO ₂	24.9	11,928	55,207	9,412	4,261	6,428	7,169	4,504
600	Al ₂ O ₃	17.0	14,639	56,533	9,361	4,394	6,539	3,963	3,766

Several trends are evident from the table. Degraded materials other than scintillator are, in several ways, beneficial. First, they shorten the overall length, usually leading to fewer decayed or escaped kaons and to larger total numbers of stopped kaons. A significant portion of the benefit comes from larger densities of the materials. (The densities of BeO, diamond, SiO₂, and Al₂O₃ are 3.0, 3.52, 2.65, and 3.95 g/cm³, respectively.) But heavier nuclei can also cause more multiple scatterings and produce larger backgrounds.

Second, higher beam momenta makes things worse: the total numbers of stopped K^+ are lower, and the numbers of interacted and escaped kaons are both higher. However, the loss in going from 550 to 600 MeV/ c is only $\sim 10\%$ and is more than compensated by the reduced decay fraction and higher production yield at 600 MeV/ c .

Looking into the details, the results in the degrader and target were analyzed in terms of four sub-regions: (1) the beam line, upstream of the degrader material; (2) degrader; (3) a ‘tail’ region with $Z > 0$ but Z less than the start of a stopped K^+ peak; and (4) a ‘peak’ region for stopped K^+ above a starting point. The starting point of the ‘peak’ was estimated to be where the counts began to significantly rise above the preceding ‘tail’ region. The division into ‘tail’ and ‘peak’ sub-regions

allows for the possibility that acceptance windows might be placed on the location of stopped kaons in the peak. Otherwise, the number of stopped K^+ in the target is the sum of the two sub-regions, as listed in Table 6.3.

The breakdown of stopped and decayed K^+ in the four sub-regions is shown in Table 6.4. The breakdowns for the interacted kaons are not included as they account for only a few percent of the kaons; about 85-95% of the interactions take place in the degraders, depending on the momentum.

Table 6.4: Distribution of stopped and decayed K^+ particles in the degrader, ‘tail,’ and ‘peak’ sub-regions defined in the text.

Momen.	Degrader	Stopped K^+			Decayed K^+			
		Dgrdr	Tail	Peak	BmLine	Dgrdr	Tail	Peak
550	Scint	5,934	1,414	59,050	0	10,757	1,903	2,931
550	BeO	11,172	1,887	59,255	5,815	4,282	1,827	2,853
550	Diamd	12,085	1,739	61,005	6,478	3,557	1,515	3,050
600	BeO	13,433	1,966	53,303	4,198	5,078	1,645	2,527
600	SiO ₂	11,928	1,581	53,626	3,526	5,886	1,554	2,707
600	Al ₂ O ₃	14,639	1,598	54,935	5,262	6,539	1,439	2,956

Although the total number of stopped K^+ in the target is lower at 600 MeV/ c , the fraction in the tail region is also lower at this momentum. Aluminum oxide appears to be the best choice of degrader (excluding diamond due to cost). It can provide the largest number of stopped K^+ in the target, particularly in the peak with low numbers in the tail region. The BeO and SiO₂ degraders are comparable, with possibly a slight edge for SiO₂.

Distributions of K^+ stopping in the materials, decaying, or ‘escaping’ from the beam line or detector are shown in Fig. 6.4 for selected cases at both energies.

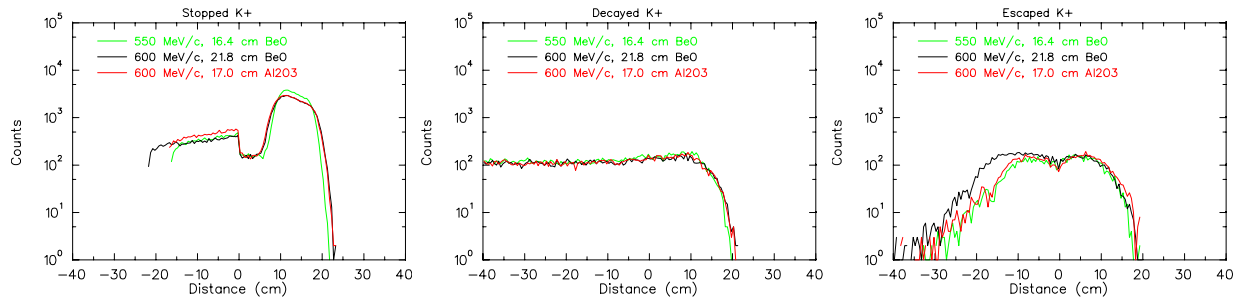


Figure 6.4: Distributions of stopped, decayed, and escaped K^+ . The target starts at $Z = 0$.

6.2.3 Secondaries

In addition to the kaons, production of secondary particles into the detector is also a matter of concern. Here, we consider all particles that ‘escaped’ into the outside region. Table 6.5 lists the yields for the dominant particles.

In the table, no discrimination has been made on the number of daughter layers, or the origins of the particles. For example, π^0 s are not tracked, and the daughter photons are included in the γ

Table 6.5: Yields of the dominant particles that ‘escape’ from the degrader and target into a detector region.

Mom.	Dgrdr	p	e^+	e^-	γ	n	μ^+	π^+	π^-	K^+
550	Scint	2637	14,163	17,524	117,403	18,017	54,093	18,787	2216	12,560
550	BeO	1252	16,567	18,878	153,190	28,471	57,327	19,246	2138	6,843
550	Diamd	1155	16,342	19,048	157,030	23,003	58,601	19,292	1982	4,979
600	BeO	1404	16,719	18,209	159,508	35,398	53,841	18,396	2634	9,769
600	SiO ₂	1460	17,620	18,358	189,851	28,810	53,405	18,363	2559	11,673
600	Al ₂ O ₃	1239	18,718	19,165	220,960	37,361	55,449	18,427	2338	7,729

column. Most of the μ^+ particles come from the decay of the K^+ . The fact that the μ^+ numbers are reduced in going from 550 to 600 MeV reflects the reduction in stopped and decayed K^+ .

The table does not include escaped K^0 and \bar{K}^0 particles. About 2000-2400 were produced at 550 MeV/ c , and about 3000 at 600 MeV/ c . The ratio of K^0/\bar{K}^0 was typically about 1.5 at both momenta.

Many of the yields have, at most, modest dependence on beam momentum. But attention is drawn specifically to the γ and n numbers. Not only do they increase significantly with beam momentum, even for the same degrader material, they also depend on the material. Generally, nuclei with larger Z or N , and especially larger N/Z , should be avoided. On the other hand, other benefits come from materials with higher densities.

The calculations here do not include other elements in the beam line such as trigger scintillators, Čerenkov detectors, or wire chambers. These items would be located upstream and would cause additional losses due to interactions and out-scattering.

6.2.4 Summary of Degradar/Stopping Efficiency Calculations

In summary, the FLUKA simulations indicate that $\sim 55\%$ of the 600-MeV/ c K^+ that enter the beam line can be stopped in the scintillating target. The fraction is a bit higher at 550 MeV/ c , but not enough to overcome the loss of flux due to decay. The best degrader materials should have low Z and high density. Good choices are Al₂O₃ or BeO.

Simulations were also conducted for the E949 experiment [2], and were in reasonable agreement with data from the experiment. The implications for the ORKA experiment are discussed in Chapter 9.

References

- [1] Fluka Monte Carlo code. See <http://www.fluka.org/fluka.php> and references therein.
- [2] S. Adler *et al.*, Phys. Rev. D **77**, 052003 (2008); A. V. Artamonov *et al.*, Phys. Rev. D **79**, 092004 (2009).

7 Spectrometer

The spectrometer proposed for ORKA is illustrated in Fig. 7.1. It will be an improved version of the E949 detector (see Fig. B in Appendix B).

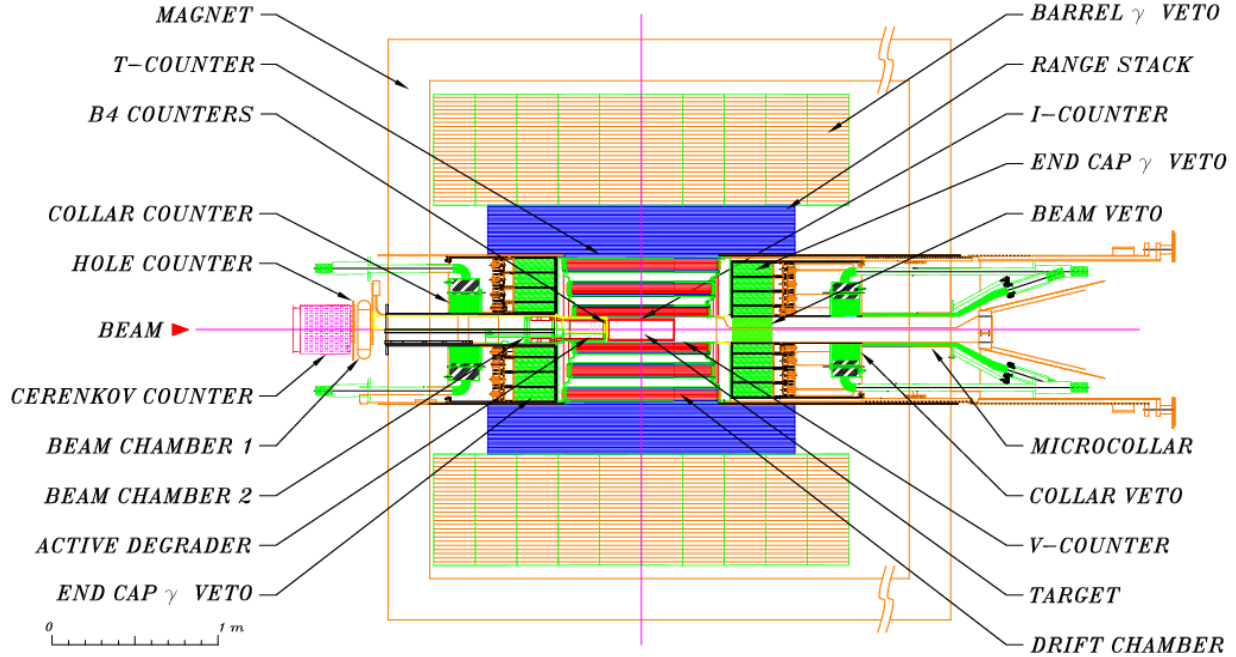


Figure 7.1: Elevation view of the proposed ORKA detector. The beam enters from the left, and several key components are labeled.

Kaons will be stopped in a highly segmented active target and $K^+ \rightarrow \pi^+ \nu \bar{\nu}$ events will be observed by using a high-precision central drift chamber surrounded by segmented scintillation detectors for measuring pion range, energy, and the $\pi - \mu - e$ decay sequence, and also an efficient 4π solid-angle calorimeter for vetoing events accompanied by gamma rays. An existing solenoid magnet, such as the CDF solenoid, run with a 1.25-T magnetic field will be used to allow a longer detector with increased solid angle acceptance and improved momentum resolution. Other improvements are anticipated, including $4\times$ finer segmentation of the pion stopping-region ‘Range Stack’ (RS) detectors. The photon veto detector will also be enhanced by using 23 radiation lengths compared to 17.3 used in E949.

7.1 Magnet

The default plan is to use the CDF solenoid, although the CLEO solenoid is also well suited. The field will be increased by 20–30% over E949 to 1.2–1.3 T, and the length of the Drift Chamber, Range Stack and Barrel Veto can be extended in Z from 50 cm to 80 cm to increase the solid angle acceptance of the detector and made to fit within either new magnet.

7.2 Beam and Target

Beam instrumentation similar to E949 will be used in the new spectrometer. A Fitch-style Čerenkov detector capable of efficient pion and kaon detection would be placed immediately downstream of or within the last quadrupole of the kaon beam line. It will be followed by two drift chambers, each with X , U , and V views. An active degrader will be placed immediately upstream of a two-plane (U and V views) scintillator hodoscope similar to B4 in E949. The final element is the scintillating fiber stopping target.

In the following, it is assumed that waveform digitizers are 500-MHz, 10-bit, unless stated otherwise, and that an ADC is either a QIE-style device or another slower WFD (~ 50 – 100 MHz clock).

- Čerenkov (28 channels)
 - Similar to E949, but requires smaller longitudinal extent
 - TDC and WFD readout
- Beam wire chambers (~ 1000 channels)
 - Faster gas would give better time resolution
 - TDC readout
- Active degrader (~ 50 channels). The active degrader has three requirements: Slowing the incoming kaons, discrimination of incoming kaons and pions, and detection of photons from kaon decay in the target. The latter two necessitate an active material such as scintillator or lead glass with segmented readout (either in Z or azimuthally, or both) of a few radiation lengths. The former requirement can be best satisfied by low- Z material to minimize dispersion of the beam. The degrader specifications will be determined by optimization based on these requirements. Wave-shifter fiber readout is likely in any case with a WFD, TDC, and QIE or ADC on every element.
- Beam hodoscopes (~ 32 channels) provide the position of the incoming beam particle as well as dE/dx information. A suitable design would have overlapping “ Z ”-shape scintillator fingers similar to E949 with fiber readout and a TDC, WFD, and QIE/ADC on each channel.
- Target (~ 500 channels). E949’s target was composed of 413 5-mm-square, 310-cm-long scintillating fibers packed into a rectangular grid to form a 6-cm-radius cylinder and readout by 1” PMTs. Smaller “edge” fibers filled the gaps near the outer edge and were grouped into additional PMTs. Each fiber was readout by a TDC, an ADC, and two 8-bit WFDs with gains of $\times 3$ and $\times 1$.

The ORKA target would be similar in radius and will likely use smaller elements. A shorter target (~ 100 cm) with double-ended readout would increase the light yield and provide better Z information for measurement of the kaon decay point and the outgoing pion. Double-ended readout could be accomplished by using clear fibers connected to PMTs or other photo-sensors outside the magnet. The means to extract the fibers, particularly on the upstream end, requires a detailed design. An alternative would be to readout only the downstream end and mirror the upstream end of the fibers (as was done in E949) while maintaining the ~ 100 -cm length. A cylindrical photon veto would be needed in the downstream region to provide capability lost by the short target. Another alternative would be to duplicate the E949 target. For all options, each channel would have a TDC, QIE/ADC, and 10-bit WFD.

7.3 Drift Chamber

The low-mass central Drift Chamber will have a 43.3-cm outer radius similar to that used in E949 [1] but will be longer (87.4 cm) (Sec. 9.1.3) to provide a fiducial length of ± 43.3 cm and larger solid angle. An attempt will be made to reduce the mass of the endplates and local electronics in order to minimize inactive materials. Faster gas and/or smaller cells would give reduced accidental loss, but resolution might be compromised. We expect ~ 2000 channels.

7.4 Range Stack

The Range Stack is similar to that in E949 but composed of 30 layers and 48 azimuthal sectors where each element would be half as thick (~ 9.5 mm) and half as wide, for an inner radius of 44.5 cm and an outer radius of 74.5 cm. Each element would be ~ 185 -cm long and readout on both ends. Cast plastic scintillator with diamond-polished sides as in E949 would be desirable. Minerva-style extruded scintillator is a possibility, but concerns about uniformity of response and gaps between counters must be addressed. Tests of prototypes in a π^+ beam at TRIUMF will be performed. E949 had ~ 10 photoelectrons per MeV, whereas ≥ 20 PE/MeV is desirable. Perhaps this level could be achieved with higher quantum efficiency photon detectors and/or better optical coupling than in E949. Fiber readout would be needed to get signals from the photon detectors outside of the magnet, with a TDC, QIE/ADC, and WFD on each end of each element. An alternative would be a TDC, low- and high-gain WFD per channel.

7.5 Photon Veto

A 23-radiation-length-thick Barrel Veto (BV) with Shashlyk-style elements similar to those designed for KOPIO [2] would satisfy the photon veto requirement. A possible configuration for each module would be 155 interleaved layers of 0.8-mm lead and 1.6-mm scintillator readout by ~ 400 WLS fibers. Including the bundling and routing of the fibers, the total depth of each module would be ~ 67 cm without a photon detector. This depth would preserve ~ 10 cm of space between the BV and inner magnet bore. Coupling of the WLS fibers to clear fibers for readout outside the magnetic volume by PMTs is a possibility. KOPIO elements had a 25.6×20.0 cm² cross-section. Increasing each element to 32 cm \times 25 cm² would require 35 azimuthal elements and 11 elements in Z for a total of 385 elements. The total length would be ~ 353 cm to provide photon veto coverage in polar angle comparable to E949. A log-style BV, with readout on each end as in E949, is an alternative, but studies would be required to ensure that it would have the same photon veto inefficiency of Shashlyk. A TDC, QIE/ADC, and WFD on every channel would be desirable. Note that the BV length will require careful integration with the final kaon beam-line elements that extend to within a meter of the center of the target.

The current design presumes re-use of the E949 pure CsI endcap crystal detectors, with TDC, QIE/ADC, and WFD on every channel (~ 200 channels).

In the upstream beam region, the empty spaces would be filled with collar-style photon vetos. The downstream region depends on the target option. A short target would allow downstream endcaps to essentially fill the beam region. This choice would require approximately 200 channels of TDC, QIE/ADC, and WFD.

7.6 Front-end Electronics

The frontend electronics for all PMT-based readout will consist of a base and a signal splitter that will feed a WFD, an ADC, and a TDC. The WFD is planned to be a 500-MHz, 10-bit ADC. The ADC is planned as a lower frequency WFD with more dynamic range.

The default plan is to use one WFD channel for every PMT channel. Every channel, including the gas chambers, will also feed a TDC. All PMTs and some of the Drift Chamber channels will feed an ADC.

Experience with E949 shows that the redundancy provided by a TDC, ADC, and WFD on each channel is important for high photon veto and signal detection efficiency.

References

- [1] S. Ahmad, E. W. Blackmore, D. A. Bryman, J. Cresswell and T. Numao, “Central Drift Chamber For Rare Kaon Decay Spectrometer,” *IEEE Trans. Nucl. Sci.* **33**, 178 (1986).
- [2] D. Bryman, e-print arXiv:hep-ex/0206072. See also <http://www.kopio.bnl.gov/> .

8 Trigger and Data Acquisition

The trigger-DAQ system will identify, readout, and store event information associated with kaon decays in the stopping target. The design of this system is guided by the principles that trigger decisions should be as loose as possible and that the amount of information stored for later offline analysis should be maximized. Doing so will help to insure the largest possible acceptance for $K^+ \rightarrow \pi^+ \nu \bar{\nu}$ events while preserving information that may be used to reject backgrounds. This philosophy is supported by current DAQ trends in high-energy physics, evident for example in the DAQ designs of NO ν A at Fermilab and NA62 at CERN, as well as the fully streaming conceptual designs for the LHCb upgrade at CERN and the Mu2e experiment at Fermilab. These designs are all motivated by recent and ongoing technology developments that enable very high bandwidth data transfers in a network fabric and large processor farms.

Several factors will drive the design of the trigger and data acquisition systems for this experiment. These factors include high beam intensity resulting in a high rate of kaon decays, long beam spills (i.e., 4.4-sec spills separated by 5.6 sec gaps), the need to record about 10 μ sec of time history for many detector channels for each trigger, and the need to avoid downtime.

In the following sections, we will describe a scenario for our trigger/DAQ system. These are preliminary ideas that will have to be developed in detail with engineering support. Because detector front-ends have not been fully specified at this early time, some generality in this discussion is unavoidable.

8.1 Detector Rates and Downtime Issues

As in any rare decay experiment, large beam intensities and large decay rates result in high detector rates. Table 8.1 lists the various detector systems and their expected instantaneous rates for a nominal 20 MHz of kaons into the stopping target during the beam spill; these rates are based on extrapolations from actual E949 experience.

Table 8.1: For each subdetector, approximate channel counts, hit multiplicities, total rates, and rate per channel are shown, assuming the design beam intensity, based on E949 experience.

System	Subsystem	No. Chan	Hit Multi	Total Rate (MHz)	Rate per Chan (kHz)
Beam Counters	Hodoscopes	32	4.3	110	3500
	Drift Chambers	1000	6.0	160	160
	Cherenkov	28	14	370	13,000
	Degrader	50	2.6	68	1400
Target		1000	30	330	330
Central Drift Chamber		2000	27	290	150
Range Stack		2880	340	3700	1300
Photon Veto	Endcaps	200	25	270	1400
	Barrel	385	4	43	110
	Other	100	2.4	26	260

Downtime must be avoided both at the single channel level and at the trigger level. Single-channel downtime is dangerous because a signal in a detector element (*e.g.*, a photon veto counter) might be lost. Because we must suppress photons from the primary background source $K^+ \rightarrow \pi^+ \pi^0$, we

cannot allow for individual channels to be dead due to an earlier hit in the same channel. Such losses will be minimized by continuously digitizing all critical channels and reading out hits continuously. While a hit can still be lost if it is preceded closely in time by a larger hit, the full pulse-shape record provides the best possible information to separate the signals.

Trigger deadtime can be avoided by, effectively, having no trigger. More precisely, the idea is to read out complete events into a processor farm before any event selection is made. With the rather low channel count of our detector, this should be possible. In this scenario, low-level trigger decisions are not necessary, although we expect to form low-level trigger primitives that will be pipelined and readout along with raw data. These low-level trigger primitives will, for instance, flag time periods during which an incoming beam kaon stopped within about one K^+ lifetime of a charged particle emerging from the target and being detected in the range stack. Such primitives can be formed for separate regions of the detector and may provide the seed information for a high-level software-based event selection.

8.2 Data Acquisition Architecture

Triggerless data acquisition involves reading out continuous streams of data from the detector. Large bandwidth is required, but current technology can accommodate the data transfer rates required for this experiment. Data will be temporarily stored in memory associated with a processor farm realized in firmware and commodity processors on the network fabric. The processing farm will execute high-level software algorithms to build events and select those which are appropriate for permanent storage on disk. Such a system is conceptually simple and has the benefit that trigger decisions are only made by relatively sophisticated algorithms that have access to full events, thereby offering the best opportunity to maximize trigger acceptance and minimize any losses from overlapping K -decays. Figure 8.1 illustrates such a system.

Signals from detector elements will be digitized in front-end electronics, producing both ADC and TDC values and, for the scintillator systems, also a sequence of FADC values providing a time-history for the hit channel (i.e., a digitized waveform). This information will be packaged along with channel ID information, then read out via high-speed optical data links to a network switch which will direct data to processor nodes, where events will be built and where a filter algorithm will select a small subset of events for permanent storage. Note that this system is highly scalable both at the front-end, because the number of data links can be varied to meet the demand of different detector elements, and in the number of nodes in the processor farm.

E949 recorded a 10 μ sec history for critical counters by using 500-MHz, 8-bit transient digitizers that sampled for 2 μ sec along with multi-hit TDCs that sampled for 10 μ sec. For this experiment, we will evaluate a number of possible scenarios, with the general goal of providing good pulse-height and timing information over a period of about -150 to $+200$ ns around each PMT hit. For instance, 500-MHz, 10-bit FADCs on all channels may accomplish this goal, or we may opt to split signals and also record TDC information and possibly other ADC information. We will reassess the optimal digitization rate and dynamic range in view of available FADCs, but we will assume 500-MHz, 10-bit digitization for this discussion. The front-end electronics will have to package the ADC, TDC, and FADC information for transmission. Zero suppression for the FADCs may be implemented in order to achieve some data compression at the front-end. We expect about 100 bytes of information per hit should be adequate to store the necessary information, including the overhead for a header with address information, global timestamp, etc. In this scenario, the Range Stack counters, used to identify the $\pi \rightarrow \mu \rightarrow e$ decay chain, do not need to be treated differently from other counters. Drift chamber signals will be readout with a combination of TDCs and ADCs (or FADCs), but will not significantly impact the data volume compared to the Range Stack. Based on the rates from Table 8.1, a single Range Stack channel would generate about

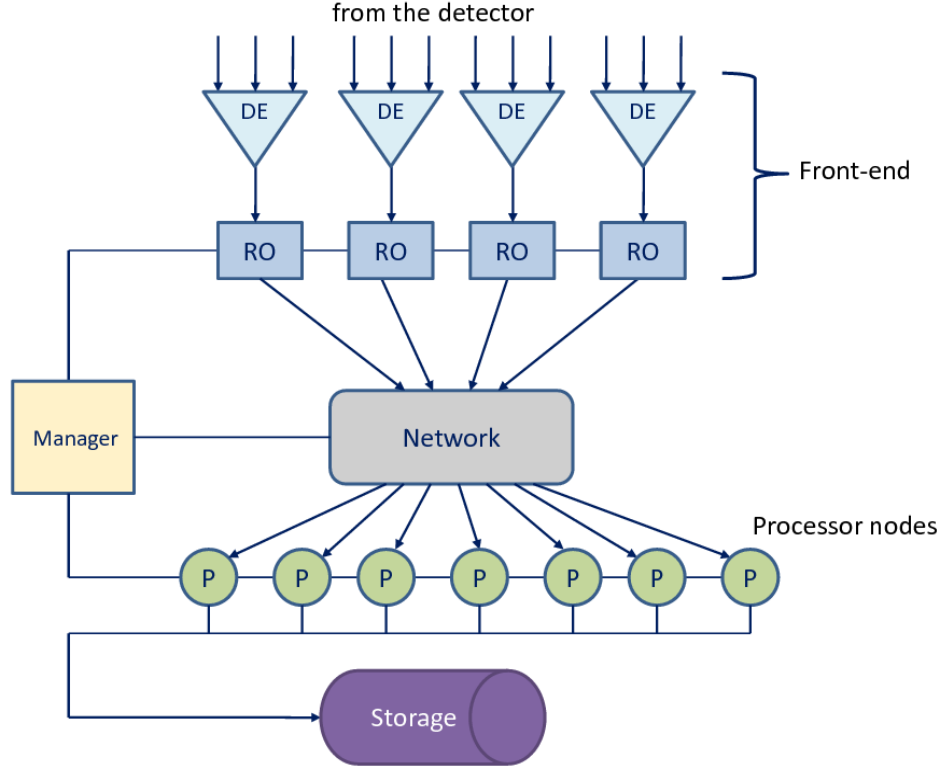


Figure 8.1: A scalable triggerless data acquisition architecture. Detector electronics (DE) sends hit information to readout modules (RO), which transmit data over high-speed optical data links to a network switch that routes data from different parts of the detector to individual processor nodes (P). Events are selected and prepared for storage in the processor nodes. The number of front-end data links and/or the number of processor nodes can be increased to add throughput to the system.

130 Mbytes/s ($1.3 \text{ MHz} \times 100 \text{ bytes}$) of data during the beam spill. The full Range Stack, with 2880 channels, would thus generate about 370 Gbytes/sec. These data can be split over several data links (optical links with 40 Gbits/s capacity are available today). A similar approach can be applied to the other detector systems.

8.3 Event Storage

The high-level filter algorithm running on the processor farm will select events for permanent storage. The filter algorithm will reconstruct tracks and associate them with counter signals based on ADC and TDC information from the central drift chamber, stopping target, Range Stack, and photon veto systems. It can apply matching requirements between the track and hits in the stopping target, track momentum versus range and energy cuts, and reject clear cases of events coincident with signals in the Photon Veto counters. Range Stack FADC records can also be inspected to apply preliminary $\pi \rightarrow \mu$ identification. The number of events passing the high-level filter can be tuned, but a working number of 500 per second will be used for illustration. For 5000 hours of running per year, this rate results in 9×10^9 events per year. Even assuming the high number of 1000 detector hits per event, the event size is only about 100 kBytes. Therefore, the data storage requirement is about 10^{15} bytes (1 petabyte) per year, which is manageable.

8.4 Controls and Monitoring

As in any experiment, a slow controls system will be needed to turn systems on and off, and to control high voltages, magnet current, thresholds, and other similar adjustable running parameters. Monitors and alarms will be necessary for all detector systems. We will take advantage of existing Fermilab standards for such tools.

An important issue for this experiment is the continuous monitoring of detector channels, particularly those critical to vetoing photons, to make sure no dead or malfunctioning channels are in the system. All scintillator-based detector elements will be monitored by a flasher system which will produce controlled light injection pulses into each element during data-taking. This system will operate at about 1 Hz.

9 Sensitivity and Background Estimate

The sensitivity estimate of the new experiment (ORKA) is based as much as possible on extrapolation from and experience with E949 and E787. This chapter is organized as follows. Sections 9.1 and 9.2 describe the expected increase in detector acceptance and the number of stopped kaons per year, respectively. Section 9.3 describes the expected background sources. Section 9.4 contains the estimated precision on $\mathcal{B}(K^+ \rightarrow \pi^+ \nu \bar{\nu})$.

9.1 Detector Acceptance

The estimates of the increase in acceptance are summarized in Table 9.1 and described in the following subsections. The estimates will concentrate on the PNN1 region, but are largely applicable to the PNN2 region.

Table 9.1: Estimated acceptance increase factors for components of the acceptance. Descriptions of each estimate are provided in the sections indicated in the right hand column.

Component	Acceptance factor	Section
$\pi \rightarrow \mu \rightarrow e$	2.24 ± 0.07	9.1.1
Deadtimeless DAQ	1.35	9.1.2
Larger solid angle	1.38	9.1.3
1.25-T B field	1.12 ± 0.05	9.1.4
Range stack segmentation	1.12 ± 0.06	9.1.5
Photon veto	$1.65^{+0.39}_{-0.18}$	9.1.6
Improved target	1.06 ± 0.06	9.1.7
Macro-efficiency	1.11 ± 0.07	9.1.9
Delayed coincidence	1.11 ± 0.05	9.1.8
Product (R_{acc})	$11.28^{+3.25}_{-2.22}$	NA

9.1.1 $\pi \rightarrow \mu \rightarrow e$ Acceptance

Positive identification of the charged pion is made by observation of the $\pi^+ \rightarrow \mu^+ \rightarrow e^+$ decay chain. The $\pi \rightarrow \mu \rightarrow e$ acceptance $A_{\pi\mu e}$ is defined to be the acceptance for stopped pions in the range stack (RS) due to all cuts and trigger elements. For the E949 PNN1 analysis, $A_{\pi\mu e} = 0.35$ (Eq. 31 in [1]). To estimate the possible increase in acceptance, the inevitable losses due to cuts on the measured pion and muon lifetimes, muons escaping from the stopping counter, and undetectable positrons are given in Table 9.2. The factors for the pion and muon lifetimes assume that losses in E949 could be mitigated by the use of a deadtime-less trigger and data acquisition system (Section 9.1.2). Muon escape refers to a muon from $\pi^+ \rightarrow \mu^+ \nu_\mu$ exiting the counter that contains the stopping pion without depositing sufficient energy for detection in that counter. We assume here that it is not possible to recover these exiting muons. Undetectable positrons refers to those that do not deposit sufficient energy in at least two counters, as required for positron identification in E949. A more finely segmented RS could mitigate some of this loss. The product of the factors is $A_{\pi\mu e} = 0.78 \pm 0.02$, which implies an improvement of acceptance with respect to E949 of 2.24 ± 0.07 . Further details can be found in Ref. [3].

Table 9.2: Estimate of acceptance factors due to cuts on the measured pion and muon lifetimes, muon escaping from the stopping counter and undetectable positrons.

Quantity	Range	Acceptance	Comment
π decay	(3,105) ns	0.8734	Realistic maximum (E949 cuts)
μ decay	(0.1,10) μ s	0.9450	Realistic maximum (E949 cuts)
μ escape	NA	0.98	E949 technote K036[4]
e^+ detection	NA	0.97 ± 0.03	Guess
Product		0.78 ± 0.02	

9.1.2 Deadtimeless Data Acquisition

The typical deadtime for the trigger and data acquisition was 26% (Sec. II.I of [1]). A deadtime-less DAQ and trigger would gain $1/0.74 = 1.35$ in acceptance. A deadtime-less DAQ and trigger are required to attain the expected gain in $\pi \rightarrow \mu \rightarrow e$ selection described in Sec. 9.1.1.

9.1.3 Larger Solid Angle

The E949 Drift Chamber was 50.8 cm long at the outer radius of 43.3 cm [1]. Increasing the length to 84.7 cm would increase the solid angle acceptance by 1.38. Lengthening the drift chamber would require lengthening the Range Stack and Barrel Photon Veto also. It is assumed that the performance of the longer barrel elements (Drift Chamber, Range Stack and Barrel Veto) would attain or exceed the performance achieved in E949.

9.1.4 Magnetic Field

Increasing the solenoidal magnetic field from 1 T to 1.25 T would improve the momentum resolution. The estimated momentum resolution of a 43-cm-outer-radius drift chamber with the same radial thickness (0.002 radiation lengths) and measurement precision (200 μ m) as the E949 drift chamber is compared with the E949 momentum resolution in Figure 9.1. In the PNN1 region from the $K_{\pi 2}$ peak of 205 MeV/ c to the kinematic limit of 227 MeV/ c , the resolution of the proposed experiment is ≤ 0.90 times that of E949. The energy resolution at the $K_{\pi 2}$ peak in E949 was 2.976 ± 0.005 MeV, or 0.93 times the E787 resolution of 3.205 ± 0.005 (Table 13 of [5]) and allowed a $\times 1.12$ increase in acceptance in E949 with respect to E787. Assuming a linear dependence of acceptance increase upon the momentum resolution would yield $\times 1.17$. The estimated acceptance increase due to the improvement in momentum resolution is taken to be 1.12 ± 0.05 .

9.1.5 Range Stack Segmentation

Range Stack elements with half the thickness and half the width of those in E949 would reduce accidental losses in $\pi \rightarrow \mu \rightarrow e$ detection. RS elements with half the width of those in E949 are estimated from a simple model to give an improvement of 0.87 ± 0.05 in range resolution. Detailed simulation could provide a more accurate estimate. Extrapolation from the acceptance increase in energy resolution as described in the Sec. 9.1.4 would give an acceptance increase of 1.12 ± 0.06 due to improved range resolution.

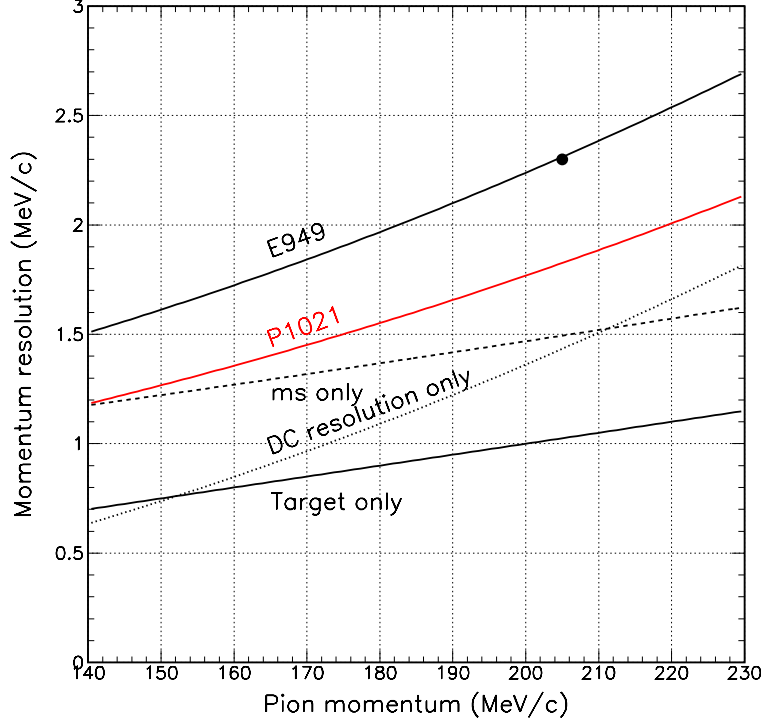


Figure 9.1: The estimated momentum resolution as a function of pion momentum for E949 and ORKA. The latter is indicated by the red line. The contributions to the E949 resolution from multiple scattering (“ms only”), drift chamber resolution (“DC resolution only”) and the target (“Target only”) are shown. The single black point at 205 MeV/c corresponds to the measured resolution for $K_{\pi 2}$ decays in E949 (Table II of [1]). The target contribution to the uncertainty in the track curvature is taken to be 0.015 MeV/c/p so that the quadrature sum of the three components agrees with the measured point at 205 MeV/c.

9.1.6 Photon Veto

The proposed thickness of the barrel region of the new detector would be 23 radiation lengths (r.l.) compared to 17.3 r.l. in E949 (Fig. 7 of [1]). The increase in signal acceptance can be estimated from simulation studies for the KOPIO experiment (Table A.1 and Figure A.2 of [6]). The main background with photons in KOPIO is $K_L \rightarrow \pi^0 \pi^0$ and the photon energy distribution is similar to that in E949, although KOPIO’s background photons extend below 20 MeV which is the lower limit for photons from $K_{\pi 2}$ decay-at-rest. The KOPIO studies determined the signal yield for KOPIO photon veto (PV) thicknesses of 16, 18, 21.6, and 26 radiation lengths for three representative sets of selection criteria with fixed S/B of 2 or 8. The estimated improvement of increasing the PV thickness from 17.3 to 23 r.l. is $1.65^{+0.39}_{-0.18}$ where the uncertainty is based on differing interpolations schemes.

The improvement in acceptance for the PNN2 region would likely be larger as the main PNN2 background is $K_{\pi 2}$ with the π^+ scattering in the target. Greater background rejection is needed from the photon veto because cuts on kinematic quantities are less effective in suppressing this $K_{\pi 2}$ background than in the PNN1 analysis.

9.1.7 Improved Target

A target with readout on each end of each fiber, as opposed to the single-ended readout in E949, would improve the light yield by roughly a factor of 2 and provide improved discrimination of the kaon decay point in Z (in the beam direction). It is difficult to assess the acceptance improvement of such a target from E949 data. Cuts related to the Z of the kaon decay point had a relative acceptance of 0.97 (Table 32 of [5]) and 0.91 (Table 62 of [7]) for the E949 PNN1 and PNN2 analyses, respectively. The acceptance increase from an improved target is estimated to be 1.06 ± 0.06 .

An improved target would likely provide larger benefits for the PNN2 region as a result of better identification and rejection of $K_{\pi 2}$ -scatter background.

9.1.8 Delayed Coincidence

E949 required a delayed coincidence of 2 ns between the stopped kaon and the outgoing pion to suppress prompt backgrounds. The one online and two offline components of this requirement had a cumulative acceptance of 0.7632 [5, 3]. Given the kaon lifetime, the acceptance of a (2.0 ± 0.5) -ns requirement is 0.851 ± 0.035 . An improved trigger and DAQ would likely regain the lost acceptance of a 2-ns requirement, and additional improvement would be possible with better time resolution. The estimated improvement factor is taken as $(0.851 \pm 0.035)/0.763 = 1.11 \pm 0.05$.

9.1.9 Macro-efficiency

Table 9.3 compares the “macro-efficiency” of E949 with FNAL experiments in fiscal year 2008 [9]. The E949 best week is consistent with MiniBooNE and SciBooNE performance. Assuming such current FNAL experiments are the best approximation to a future E949-like experiment yields an expected macro-efficiency of 0.85 ± 0.05 , where the uncertainty is a symmetrized guess based on performance of 95% for both the beam and experiment.

Table 9.3: Macro-efficiency of E949 compared to FNAL experiments in FY08. The E949 data are from [8] and the FNAL data are largely from [9]. The “Beam on” fraction for CDF and D0 is determined from the 16% unscheduled downtime of the collider. The “Beam on” fraction of MiniBooNE and SciBooNE is estimated from some SciBooNE weekly reports at the all-experimenters meetings. The MINOS data recording efficiency corresponds to the far detector only.

Experiment	Beam on	Data recorded	Macro-efficiency
E949	0.858	0.890	0.763
E949 best week	0.894	0.940	0.840
CDF	0.84	0.83	0.697
D0	0.84	0.906	0.761
MINOS	0.75	0.99	0.742
MiniBooNE	~ 0.90	> 0.95	0.855
SciBooNE	~ 0.90	0.95	0.855

9.1.10 Other Acceptance Gains

Other possible acceptance gains include

1. Elimination of some losses incurred by the E949 trigger for short- and long-range tracks. The trigger/DAQ described in Chapter 8 would enable a more sophisticated online treatment of events with a more accurate assessment of the track range.
2. Optimization of the instantaneous rate of stopped kaons with respect to accidental losses. The lower-momentum kaon beam is expected to produce a lower accidental rate per stopped kaon, although the precise rate is difficult to estimate. In addition, if NO ν A “Beam on” performance is comparable to MINOS (Table 9.3), there will be the opportunity to run ORKA at a higher instantaneous rate without impacting the neutrino program.

These gains are difficult to quantify based solely on the E949 experience.

9.2 Stopped Kaons per Year

The estimated number of stopped kaons per year is based on extrapolation from the E949 experiment “as run” (not “as proposed”). Table 9.4 summarizes the estimation.

9.2.1 Proton Accounting

As described in Sec. II.B of [1], E949 was not run as proposed due to a broken motor generator at the AGS. E949 ran with a 21.5-GeV/ c proton beam with a 65×10^{12} protons per 2.2-s spill and with a 3.2-s interspill. The protons impinged upon a 6-cm platinum target, and a 710-MeV/ c kaon beam at 0° was collected and transported by the LESB-III beamline.

Running the Main Injector at 95 GeV/ c with a cycle time of 10 seconds and a flat-top of 4.4 seconds yields a duty factor of 0.44 with 48×10^{12} protons per spill (Chapter 4).

9.2.2 Kaon Beamline

The 19.6-m-long LESB-III beamline contained two electro-magnetostatic separators with an angular acceptance of 12 msr and momentum acceptance of $\Delta p/p = 4.0\%$ (FWHM) at 710 MeV/ c [10]. The final 2.6 m of the beamline was a “drift” region from the end of the final quadrupole, and was largely occupied by the E949 experiment [11]. There were 12.8×10^6 kaons per spill with a kaon-to-pion ratio of 3 incident upon the E949 Cherenkov counter which served as the effective end of the beamline at 17.6 m. The nominal $K:\pi$ ratio was 4 for LESB-III but, during the E949 run, the first separator was run below its nominal operating point due to high voltage discharges.

The proposed kaon beamline (Sec. 6.1) would be 13.74 m with an angular acceptance of 20 msr and momentum acceptance of $\Delta p/p = 6.0\%$ at 600 MeV/ c . It also contains two electro-magnetostatic separators and supposes a 8-cm-long platinum target for kaon production. The kaon and pion survival probabilities of a 13.74-m beamline are 4.77% and 66.4%, respectively. The simulation used to estimate the fraction of K^+ that stop in the target (Sec. 9.2.4) assumed an effective beamline

Table 9.4: The E949 experiment “as run” is compared with the proposed experiment. N_K is the number of kaons entering the Cherenkov detector that defines the upstream end of the experiment. Instantaneous is abbreviated as “inst.” and average as “ave.” in the table. Descriptions can be found in the section indicated in the right hand column.

Component	E949 “as run”	ORKA	Ratio	Section
Proton momentum (GeV/c)	21.5	95	$R_{\text{proton}} = 0.738$	9.2.1
Protons/spill	65×10^{12}	48×10^{12}		9.2.1
Spill length(s)	2.2	4.4		9.2.1
Interspill(s)	3.2	5.6		9.2.1
Duty factor	0.41	0.44		9.2.1
protons/sec(ave.)	12×10^{12}	4.8×10^{12}		9.2.1
protons/sec(inst.)	15.9×10^{12}	10.9×10^{12}		9.2.1
Kaon momentum (MeV/c)	710	600	$R_{\text{surv}} = 1.4408$ $R_{\text{ang}} = 1.66$ $R_{\Delta p} = 1.5$	9.2.2
K beamline length(m)	19.6	13.74		9.2.2
Effective beam length(m)	17.6	13.21		9.2.2
K survival factor	0.0372	0.0536		9.2.2
Angular acceptance (msr)	12	20		9.2.2
$\Delta p/p(\%)$	4.0	6.0		9.2.2
$K^+:\pi^+$ ratio	3	3.31 ± 0.41		9.2.2
Relative K/proton	—	—	$R_{K/p} = 6.5 \pm 0.8$	9.2.3
N_K/spill	12.8×10^6	$(88.5 \pm 10.9) \times 10^6$		9.2.5
$N_K/\text{sec(inst.)}$	6.3×10^6	$(20.1 \pm 2.5) \times 10^6$		9.2.5
$N_{K+\pi}/\text{sec(inst.)}$	8.4×10^6	26.2×10^6		9.2.5
$N_K/\text{sec(ave.)}$	2.6×10^6	$(8.85 \pm 1.09) \times 10^6$		9.2.5
Stopping fraction	0.21	0.54 ± 0.12		9.2.4
Kstop/s(ave.)	0.69×10^6	$(4.78 \pm 1.21) \times 10^6$		9.2.5
Running time(hr)	—	5000		9.2.5
Kstop/”year”	—	$(8.6 \pm 2.2) \times 10^{13}$		9.2.5
$\mathcal{S}'_{\text{loss}}$			0.77 ± 0.02	9.2.5

length of 13.21 m which implies a kaon survival probability of 5.36%. By assuming a relative pion-to-kaon production rate of 24 ± 3 (Chapter 4) and a 0.1% transmission of pions (Chapter 6), the estimated $K:\pi$ ratio would be 3.31 ± 0.41 , comparable to E949.

9.2.3 Kaon Production

The estimate of the relative rate of K^+ between E949 and a 95 GeV incident proton beam is described in Chapter 4 and summarized in Table 4.3. We average the MARS-LAQGSM and MARS-default relative rates of 7.09 ± 0.65 and 5.97 ± 0.46 , respectively, to obtain 6.53 ± 0.82 where an additional $\pm 8.6\%$ uncertainty is assigned to cover the spread between the relative rates from the two model results.

9.2.4 Kaon Stopping Fraction

The kaon stopping fraction is defined as the number of kaons entering the experiment that come to rest in the stopping target. For the purposes of these calculations, kaons enter the experiment at the effective end of the kaon beamline as described in Sec. 9.2.2. In E949, 6.3 MHz of kaons traversed the Cherenkov counter and 1.70×10^6 kaons per second (instantaneous) stopped in the target. With a factor $f_s = 0.774$ to correct for kaons that left the target (see Eq. 36 of Ref. [1]), the target stopping fraction was 21% [1].

In a simulation of the beam and target region of the new experiment for a 550-MeV/c kaon beam described in Sec. 9.2.2, the number of stopped kaons per 100,000 incident kaons is 59050, 59255 and 61005 for degraders of scintillator, BeO and diamond, respectively (Table 6.4). For a 600-MeV/c beam, the number of stopped kaons per 100,00 incident kaons is 53303, 53626 and 54935 for degraders of BeO, SiO₂ and Al₂O₃, respectively. We assume a stopping fraction of 0.54 with a range of ± 0.02 to take into account the possibility of different degraders. A simulation of the E949 710-MeV/c beamline yields 24,806 stopped kaons for 100,979 incident or 0.246. Correcting for the differing beamline lengths in E949 and the simulation gives a stopping fraction of $0.246/0.92 = 0.266$, in reasonable agreement with the E949 data. The stopping fraction of the new experiment is assumed to be 0.54 ± 0.12 where the additional uncertainty is taken from the fractional difference between data and simulation for the E949 beamline.

9.2.5 Expected Rate of Stopped Kaons and Signal Yield

The expected rate of kaons per spill incident upon the experiment can be estimated as

$$\begin{aligned} N_K(\text{ORKA})/\text{spill} &= N_K(\text{E949})/\text{spill} \times R_{\text{surv}} \times R_{\text{proton}} \times R_{K/p} \\ &= 12.8 \times 10^6 \times 1.4408 \times 0.7385 \times (6.5 \pm 0.8) \\ &= (88.5 \pm 10.9) \times 10^6 . \end{aligned} \quad (20)$$

For a 4.4 s spill, the instantaneous rate of kaons entering the experiment is

$$N_K/\text{s}(\text{inst.}) = (88.5 \pm 10.9) \times 10^6 / 4.4\text{s} = (20.1 \pm 2.5) \times 10^6 \text{ } K^+/\text{s} \quad (21)$$

and the instantaneous rate of pions and kaons, assuming a $K^+:\pi^+$ ratio of 3.31 (Sec. 9.2.2) entering the experiment, is

$$N_{K+\pi}/\text{s}(\text{inst.}) = N_K/\text{s}(\text{inst.}) \times (1 + 1/(K^+/\pi^+)) = 20.1 \times 10^6 \times (1 + 1/3.31) = 26.2 \times 10^6 , \quad (22)$$

which is over three times the instantaneous rate in E949 of $6.3 \text{ MHz} \times (1 + 1/3) = 8.4 \text{ MHz}$. Accidental veto rates in E787 and E949 scale with $N_{K+\pi}/\text{s}(\text{inst.})$ [12].

Based on E949 photon veto data, the expected relative loss of acceptance due to the higher rate is estimated to be $\mathcal{S}_{\text{loss}} = 0.54 \pm 0.02$ [13]. We assume that the time window for the photon veto in P1021 will be halved with respect to E949 due to improvements in light collection efficiency. The resulting loss is $\mathcal{S}'_{\text{loss}} = 1 - (1 - \mathcal{S}_{\text{loss}})/2 = 0.77 \pm 0.02$. This estimate does not take into account the anticipated reduction in singles rate due the increase in the target stopping fraction.

For one year of running (5000 hours), the total number of stopped kaons in the experimental target is

$$\begin{aligned} N_{K\text{stop}}/\text{year} &= (88.5 \pm 10.9) \times 10^6 / 10.0\text{s} \times 5000 \times 60 \times 60 \times (0.54 \pm 0.12) \\ &= (8.6 \pm 2.2) \times 10^{13} . \end{aligned} \quad (23)$$

Assuming $\mathcal{B}(K^+ \rightarrow \pi^+ \nu \bar{\nu}) = (0.781_{-0.077}^{+0.084}) \times 10^{-10}$ (Eq. 9), the number of signal events per 5000-hour year is

$$\begin{aligned} N_{K^+ \rightarrow \pi^+ \nu \bar{\nu}} &= \mathcal{B}_{SM}(K^+ \rightarrow \pi^+ \nu \bar{\nu}) \times N_{K\text{stop}} \times A_{\text{E949}} \times R_{\text{acc}} \times \mathcal{S}'_{\text{loss}} \\ &= (0.781_{-0.077}^{+0.084}) \times 10^{-10} \times (8.6 \pm 2.2) \times 10^{13} \times (3.59 \pm 0.36) \times 10^{-3} \times (11.3_{-2.3}^{+3.3}) \times (0.77 \pm 0.02) \\ &= 210 \text{ SM-level events per year} \end{aligned} \tag{24}$$

where A_{E949} is the sum of the acceptance of the E949 PNN1 (Table 9.5) and PNN2 ($(1.37 \pm 0.14) \times 10^{-3}$ in Sec. III.D.8 in [2]) signal regions and R_{acc} is the product of acceptance factors given in Table 9.1.

Due to the availability of considerable data from E949, we are able to provide a good estimate of the uncertainty in the SM-level signal yield for ORKA of approximately 40%. In contrast, many previous rare decay experiments encountered unexpected factors that led to large (even orders of magnitude) deviations from the initial sensitivity predictions.

9.3 Backgrounds

The sources of background in the new experiment should be the same as E949. Production of the kaon beam from a 100 GeV/c proton beam with a shorter kaon beamline may introduce additional accidental hits in the new detector; however, no evidence for background or accidental activity due to the primary beam was ever observed in E949 or E787.

The total background level and the contribution from each source for the E949 PNN1 analysis is given in Table 9.5. Nearly all background components are estimated directly from data by using

Table 9.5: The components of the background for the E949 PNN1 analysis. The acceptance of the standard and extended signal region was $(1.69 \pm 0.05 \pm 0.13) \times 10^{-3}$ and $(2.22 \pm 0.07 \pm 0.15) \times 10^{-3}$, respectively. The components are described in the text. This table reproduces Table IX of [1].

Background	Standard	Extended
$K_{\pi 2}$	0.019 ± 0.004	0.216 ± 0.023
$K_{\mu 2}$ range tail	0.010 ± 0.001	0.044 ± 0.005
Muon band	0.005 ± 0.002	0.024 ± 0.010
Single beam	0.004 ± 0.002	0.006 ± 0.002
Double beam	0.003 ± 0.002	0.003 ± 0.002
CEX	0.004 ± 0.001	0.005 ± 0.001
Total	0.05 ± 0.01	0.30 ± 0.03

the bifurcated analysis technique (Sec. III.B.2 of [1]). Only the contribution of the charge-exchange (CEX) background required the use of simulation, and methodology was developed for the E949 PNN2 analysis [2] that reduced the reliance of the CEX background estimate on simulation.

Decays of stopped kaons dominate the background. The $K_{\pi 2}$ background in the PNN1 analysis occurs when the kinematic quantities of the pion (range, energy, and momentum) are mismeasured and the photons from the π^0 decay are undetected. The $K_{\mu 2}$ range-tail background is due to short-range muons, presumably due to an interaction in the range stack, and misidentification of the muon as a pion. Muon-band events are due to $K^+ \rightarrow \mu^+ \nu \gamma$ or $K^+ \mu^+ \nu \pi^0$ decays where the photon(s) are undetected and the muon is misidentified.

The three categories of beam-related background are single-beam, double-beam, and CEX background. The two processes comprising single-beam background are

1. $K_{\pi 2}$ decay-in-flight in the target of a beam kaon such that the π^+ is boosted into the signal region and the π^0 is undetected, and
2. A beam pion being misidentified as a kaon and scattering in the target into the fiducial region of the detector.

Single-beam background is suppressed by good π^+/K^+ discrimination in the beam elements, and time resolution for the delayed coincidence measurement. Double-beam background occurs when the single-beam processes are preceded by an additional incoming kaon whose decay products are undetected. Double-beam background is suppressed by requiring an absence of activity in the beam detectors in coincidence with the pion detected in the Range Stack. The charge exchange background is the result of $K^+n \rightarrow pK^0$ in the target followed by the K^0 turning into a K_L^0 and decaying semileptonically. It is suppressed by detection of the lepton, observation of a gap between the incoming K^+ and outgoing π^+ in the target, and the short flight time of the K_L^0 in the target.

9.4 Estimated Precision on $\mathcal{B}(K^+ \rightarrow \pi^+ \nu \bar{\nu})$

In E949 and E787, the product of the signal acceptance A and background rejection R was maximized, which is equivalent to maximizing the signal-to-background ratio S/B . For the estimate presented here, it is assumed that $A \times R$ remains constant as the detector acceptance is increased as described in Sec. 9.1. Additionally, the sensitivity estimate will assume that all parts of the PNN2 signal region have the same S/B and that the PNN1 signal region is divided into two regions, the “Standard” region and the region defined by the difference of the “Extended” and “Standard” regions described in Table 9.5. This is a conservative assumption in that E949 has already shown that a likelihood-based technique can improve the sensitivity by taking into account the variation in S/B within the signal region for both the PNN1 [1] and PNN2 [2] analyses.

The kaon exposure used in the PNN1 and PNN2 analyses in E949 was 1.77×10^{12} and 1.71×10^{12} , respectively, and the PNN2 background was $0.93 \pm 0.17^{+0.32}_{-0.24}$. By using the acceptance and backgrounds of the three regions and the branching fraction of 0.781×10^{-10} (Eq. 9), the expected fractional precision on $\mathcal{B}(K^+ \rightarrow \pi^+ \nu \bar{\nu})$ for five years of running would be 4.4% from statistics alone. If the background uncertainty were 10% as in the E949 PNN1 analysis, the fractional uncertainty increases to 5.3%. These values are comparable to the non-CKM theoretical uncertainty of 5.5% (Chapter 2.1). The sensitivity as a function of time is shown in Figure 9.2. The total signal yield would be 1050 events after five years of running. The likelihood-based technique would obtain higher statistical precision than this simple estimate so that the ultimate precision would depend on the knowledge of the signal acceptance and the background. Because the background and acceptance estimates are determined from data, the statistical uncertainties would be negligible in the new experiment; systematic effects would be likely be the dominant source of uncertainty. The sources of systematic uncertainty in E949 and methods for mitigation are discussed in the following sections.

9.4.1 Background Systematic Uncertainties

As described in Sec. 9.3, backgrounds were estimated from data for all but the CEX background (<10% of the total background). Extensive analysis machinery was developed and refined by E787

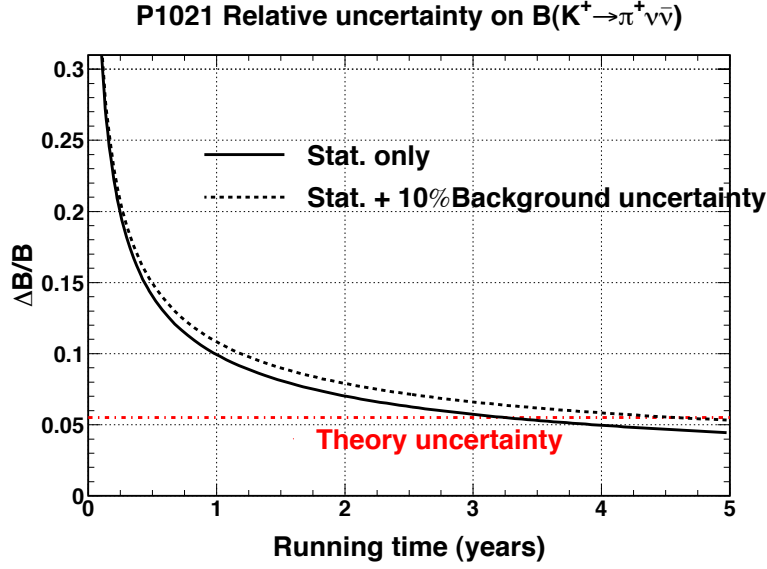


Figure 9.2: The fractional uncertainty in the $K^+ \rightarrow \pi^+ \nu \bar{\nu}$ branching ratio of P1021 as a function of running time. Solid (dashed) curve is the sensitivity assuming no (10%) background uncertainty. The red solid line is the uncertainty due to theory excluding uncertainties in the CKM matrix elements.

and E949 to enable robust and accurate estimation of the background from data. Systematic uncertainties in the background estimates can arise from

1. correlation between the two bifurcation cuts,
2. contamination of samples used in the background estimates,
3. analysis flaws,
4. unforeseen background mechanisms, or
5. analysis bias.

Correlations between the two bifurcation cuts can be measured by comparing the predicted and observed event rates near but outside the signal region (Sec. III.G.8 of [1]). When using a data-based background estimate, pure samples of a single background are prepared by inverting one cut. The rejection factor of a second cut is then evaluated from that sample. If the sample is contaminated by other backgrounds, then the rejection factor and subsequent background estimate will be flawed. The E949 PNN2 analysis developed techniques that allowed contamination levels of $\mathcal{O}(1\%)$ to be measured (Sec. III.C.8 of [2]). The “single-cut-failure” method (Sec. III.B.8 of [2] and Sec. III.G.8 of [1]) was developed to reveal analysis flaws and unforeseen background mechanisms. Individual cuts that exploit similar background characteristics are grouped together to form $\mathcal{O}(10)$ cut categories, and events that fail only a single category are examined. In E787 and E949, analysis bias was minimized by obtaining the final background estimate from a different sample than that

used to determine the selection criteria. Each set of three consecutive events was selected for the “1/3” and “2/3” samples. Selection criteria were developed by using the former sample, and the final background estimate was made from the latter sample. In fact, all studies to assess the systematic uncertainties described above were performed first on the 1/3 and then on the 2/3 sample. It might be prudent in ORKA to prepare “1/30”, “9/30” and “2/3” samples to anticipate unforeseen or different background mechanisms in the new environment.

9.4.2 Overview of Systematic Uncertainties in Acceptance

In general, the systematic uncertainties in the acceptance could be reduced by measuring the signal yield with respect to the observed $K_{\pi 2}$ and $K_{\mu 2}$ rate, which would require estimation of the relative acceptance of $K^+ \rightarrow \pi^+ \nu \bar{\nu}$ to that of $K_{\pi 2}$ and $K_{\mu 2}$. Table 9.6 lists the components of the PNN1 acceptance with the relative systematic uncertainties determined for the E949 PNN1 analysis [1]. Mitigation of the uncertainty is discussed in the following sections.

Table 9.6: The relative systematic uncertainty assessed for components of the PNN1 signal acceptance in E949 [1].

Component	Rel. unc.(%)	Description	Section
$A_{\pi \text{scat}}$	3.07	Acceptance related to π track	9.4.3
$A_{\pi \mu e}$	1.90	Acceptance of $\pi \rightarrow \mu \rightarrow e$ detection	9.4.4
A_{trig}	4.68	Geometric acceptance of trigger	9.4.5
A_{nucl}	5.01	Acceptance factor due to pion-nuclear interactions	9.4.6
$A_{T \cdot 2}$	1.50	Acceptance of $T \cdot 2$ component of trigger	9.4.7

9.4.3 Pion Track Acceptance Systematic Uncertainty

The systematic uncertainty in $A_{\pi \text{scat}}$, the acceptance related to the pion track, was assessed by increasing and decreasing by one standard deviation the size of the kinematic “box” in range, energy, and momentum in a selected sample of scattered beam pions (Sec. III.H.3 of [1]). The kinematic properties of the scattered pions are uncertain due to the identification of the scattering point in the target because the target pattern recognition is optimized for a stopped kaon decaying to a pion. *Mitigation:* Use the larger data sample to measure $A_{\pi \text{scat}}$ as a function of R , P , and E , including the $K_{\pi 2}$ peak. Use comparison with $K_{\pi 2}$ to assess the impact of the reliability of the kinematics of the scattered pion sample.

9.4.4 Acceptance of $\pi \rightarrow \mu \rightarrow e$ Detection Systematic Uncertainty

Uncertainty in $A_{\pi \mu e}$ is due to possible correlation with the μ/π particle identification cuts in the RS used in the selection of the π_{scat} sample (Sec. III.H.4 of [1]). *Mitigation:* use the larger data sample to measure the correlation as a function of the particle identification cut parameters. The more finely segmented RS for ORKA should reduce the correlations.

9.4.5 Systematic Uncertainty in Geometric Acceptance of the Trigger

The geometric acceptance of the trigger is assessed with simulation and the systematic uncertainty is based on the consistency of the cross-check measurement of the $K_{\pi 2}$ branching ratio (Sec. III.H.5 of [1]). *Mitigation:* Measure $\mathcal{B}(K^+ \rightarrow \pi^+ \nu \bar{\nu})$ relative to $\mathcal{B}(K_{\pi 2})$.

9.4.6 Systematic Uncertainty in Acceptance Loss due to Nuclear Interactions

The acceptance factor A_{nuc} due to the loss of π^+ via nuclear interactions is assessed with simulation (Sec. III.H.5 of [1]). The systematic uncertainty is assessed based on the 0.15-cm difference between the measured range resolution for $K_{\pi 2}$ events in data and simulation. *Mitigation:* Calibrate the simulation for π^+ -nucleus interaction in the RS by using a π_{scat} sample selected without the RS. Corroborate by measuring the $K_{\pi 2}$ branching ratio.

9.4.7 $T \cdot 2$ Acceptance Systematic Uncertainty

The $T \cdot 2$ requirement is a coincidence of the trigger scintillator T with the second layer of the Range Stack. Inefficiency in the $T \cdot 2$ component of the trigger is due to gaps between the T counters or the inability to detect the scant scintillation light (~ 1.7 photoelectrons/MeV [5]) in the 0.64-cm-thick T counters (Sec. III.H.6 of [1]). The counter inefficiency was measured with $K_{\pi 2}$ and $K_{\mu 2}$ samples selected without the $T \cdot 2$ requirement, and extrapolated into the signal region by taking into account particle type and dE/dx with simulation. The systematic uncertainty was assessed from the observed variation in $A_{T \cdot 2}$ when the fiducial requirement on the Z of the extrapolated track was varied. *Mitigation:* Increased light yield of the T counters would reduce inefficiency. The simulation could be calibrated by using a sample of scattered pions similar to that in Sec. 9.4.6.

References

- [1] S. Adler *et al.*, Phys. Rev. D **77**, 052003 (2008).
- [2] A. V. Artamonov *et al.*, Phys. Rev. D **79**, 092004 (2009).
- [3] D.E.Jaffe and S.Kettell, “Estimated increased acceptance of E949-like experiment”, Kaon doc-707, 28 April 2009.
- [4] D.E.Jaffe, “FITPI acceptance”, E949 Technical note K-036.
- [5] S.Chen *et al.*, “2002 $\pi \nu \bar{\nu}(1)$ Data Analysis”, E949 Technical note K-034.
- [6] Conceptual Design Report of the KOPIO Project, April 2005.
- [7] J.Ives *et al.*, “Analysis of the 2/3 E949 pnn2 data”, E949 Technical Note K-074.v1.
- [8] B.Bhuyan *et al.*, “Summary of the 2002 dataset and Pass0 processing”, E949 Technical Note K-025, December 14, 2004.
- [9] S.Brice *et al.*, Ed. J.A.Appel, “Accelerator/Experimental Operations - FY 2008”, FERMILAB-TM-2421-D0, October 2008.
- [10] “Low Energy Separated Beam III- C4”, <http://server.c-ad.bnl.gov/esfd/c4.html>

- [11] J. Doornbos *et al.*, Nucl.Inst.and Meth. A**444** (2000) 546.
- [12] P.Meyers, “Comparison of Accidental Veto Rates in LESB I and LESB III”, E787 Technical Note 244, 18 November 1992.
- [13] D.E.Jaffe, “Estimate of accidental losses in a E949-like experiment”, Kaon doc-1355, November 2011.

10 Costs

The detector design is based on the E949 design, with some modest upgrades, and advantages taken of current technology. The cost estimates are likewise in part derived from experience with E949. The accelerator, beam, and target construction costs are based on previous fixed target operations in FY99.

At this preliminary stage, the cost estimates are not based on firm designs. They represent good-faith estimates based on plausible concepts for each costed item, but in all cases much work will need to be done to arrive at defensible costs after mature designs have been made. In view of the preliminary nature of these estimates, we apply a 60% contingency on all items.

10.1 WBS and Costing Methodologies

Our cost estimate is based on a five year construction project (see Chapter 11). Labor rates are based on standard Fermilab rates, with an overhead rate of 80%. The labor rates for the drift chamber and beam chamber are taken from standard TRIUMF rates and overhead. Labor for detector installation is taken from experience with the construction of the very similar E787 detector and its upgrade to E949. The preliminary work breakdown structure is shown at the highest levels in Table 10.1.

Table 10.1: High level Work Breakdown Structure (WBS).

WBS element		Task Name
1.1		Accelerator and Beams
	1.1.1	A0 to B0 transport
	1.1.2	Target and Dump
	1.1.3	Kaon Beam
1.2		Detector
	1.2.1	Spectrometer Magnet
	1.2.2	Beam and Target
	1.2.3	Drift Chamber
	1.2.4	Range Stack
	1.2.5	Photon Veto
	1.2.6	Electronics
	1.2.7	Trigger and DAQ
	1.2.8	Software and Computing
	1.2.9	Installation and Integration
1.3		Project Management

10.2 Accelerator and Beams

Costs for Accelerator and Beams are estimated to sum to \$12M, assuming 60% contingency, and are shown in the following cost table (Table 10.2). We include individual estimates for the A0 to B0 transport, the target and beam dump, and the kaon beam line. For the A0 to B0 transport, estimates were made in consultation with Fermilab staff with relevant experience. Note that this transport is also needed by another proposed experiment and might be considered for AIP funding,

rather than be charged to this project. For the kaon separator beamline, estimates were based on the cost of the LESB-III (Low Energy Separated Beam) beamline for the BNL E787 and E949 experiments. As discussed in Chapter 4, much of the slow-extraction equipment employed in the 1999 Fermilab Fixed-Target run still exists and could possibly be re-deployed to reduce capital beamline costs. Likewise, many of the quadrupole magnets and associated spare equipment of the LESB-III beamline exists at BNL and could be re-deployed in the Fermilab separated kaon beamline to further reduce capital costs. These possible savings are not assumed in the estimated project cost.

Table 10.2: Estimated project cost. All costs in FY10 \$k.

WBS element		Description	Total Cost	60% conting.	Total w/cont.
1.0		TPC	\$33M	\$20M	\$53M
1.1		Accelerator and Beams	7,510	4,490	12,000
	1.1.1	A0 to B0 transport*	2,200	1,300	3,500
	1.1.2	Target and Dump	940	560	1,500
	1.1.3	Kaon Beam	4,370	2,630	7,000
1.2		Detector	22,390	13,430	35,820
	1.2.1	Spectrometer Magnet	500	300	800
	1.2.2	Beam and Target	600	360	960
	1.2.3	Drift Chamber	1,900	1,140	3,040
	1.2.4	Range Stack	2,500	1,500	4,000
	1.2.5	Photon Veto	3,000	1,800	4,800
	1.2.6	Electronics	4,000	2,400	6,400
	1.2.7	Trigger and DAQ	2,000	1,200	3,200
	1.2.8	Software and Computing [†]	2,000	1,200	3,200
	1.2.9	Installation and Integration	5,890	3,530	9,420
1.3		Project Management	2,740	1,640	4,380
1.4		OPC	700	420	1,120
	1.4.1	R&D	300	180	480
	1.4.2	Commissioning	400	240	640

* Candidate for off-project Accelerator Improvement Project (AIP) funding.

[†] Included here although there is no uniform practice to do so.

10.3 Detector

10.3.1 Spectrometer Magnet

Our plan is to use an existing superconducting solenoid. For this cost estimate, we assume re-use of the CDF solenoid.

10.3.2 Beam and Target

These items consist of a Čerenkov counter, two beam chambers, an active degrader, a beam scintillator hodoscope, and a scintillating fiber target. All items will be similar to the analogous detectors used in E949. We assume two-ended readout of the target, 32 hodoscope channels, 28 Čerenkov channels, 50 degrader channels, and 1000 beam chamber channels. We estimate \$600K for these detectors, plus contingency. The charge and time digitization of the signals is covered under Electronics.

10.3.3 Drift Chamber

The central drift chamber will be similar in design to the “ultra thin chamber” from E949. The chamber construction is estimated to require 6.0 FTE and \$750k in materials. The electronics for 2000 channels is estimated to cost \$700k: \$100k for preamps, \$200k for postamps/discriminators, and \$400k for cables and connectors. The mechanical infrastructure to mount the drift chamber within the spectrometer is included in the Installation and Integration budget. The charge and time digitization of the signals is covered under Electronics.

10.3.4 Range Stack

The Range Stack (RS) will have four times greater segmentation than E949. This entails 30 layers of 1-cm-thick cast Bicron BC-404 scintillator with WLS fibers in 48 sectors for a total of 1440 scintillators and 2880 readout channels. The preliminary cost estimate is \$850/channel, which includes \$500 for PMT, \$250 for scintillator, and \$100 for miscellaneous. The total cost would be \$2.5M. The mechanical infrastructure to mount the range stack within the spectrometer is included in the Installation and Integration budget. The charge and time digitization of the signals is covered under Electronics.

10.3.5 Photon Veto

The photon veto is composed of several parts. The major portion is the Barrel Veto (BV), with 385 channels. The cost estimate for the BV is derived from the KOPIO Shashlyk photon veto cost estimate. Another major portion is for the CsI endcaps (EC), which will be reused from E949. Other elements include upstream and downstream photon veto elements. We assume 200 channels for the EC along with another 100 channels for the other PV systems. The mechanical infrastructure to mount the photon veto systems within the spectrometer is included in the Installation and Integration budget. The charge and time digitization of the signals is covered in the FEE budget. We estimate \$2.4M for the BV, \$100k for the EC, and \$500k for other system elements, for a total of \$3.0M

10.3.6 Electronics

The primary elements of the Electronics WBS include the digitization systems: the wave form digitizers (WFD) and TDCs. In addition to these items, other systems include the high voltage, crates, and racks. This system is also responsible for the bases and cables for the systems readout by PMTs (everything except the drift chamber and beam chambers).

The current estimated cost for a 500-MHz 10-bit WFD is \$500/channel. For the target we plan on a WFD per PMT and two PMTs per fiber. We need 2880 WFD channels for the RS, 110 channels for the beam counters, some 300 channels for the endcaps and upstream and downstream vetos, and 385 channels for the barrel veto. Assuming a total channel count of 5000, the total cost comes to \$2.5M.

We will need an additional 2000 drift chamber and 1000 beam-chamber channels of TDC for a total of about 10,000. We may want a similar count of QIE/ADC channels. We make a very preliminary estimate of \$1.5M.

10.3.7 Trigger and DAQ

The Trigger/DAQ WBS includes the online processor farm along with the switches and fiber optic connections to the front end digitizing electronics. This WBS is responsible for the clock and clock distribution system. This WBS is also responsible for the Slow Controls, which includes control of the flasher systems (the flasher hardware is the responsibility of each detector subsystem). We currently estimate the cost of these systems to be \$2M.

10.3.8 Software and Computing

The WBS includes development of common software and computing between the DAQ and offline analysis, which are closely allied in the proposed DAQ architecture. The items include framework development and infrastructure, database management, and data-handling development. The category does not include substantial off-project effort from ORKA collaborators to develop applications, such as filter codes. It also does not include M&S for offline computing or operations.

10.3.9 Installation and Integration

Installation of all components into the spectrometer magnet is expected to require 0.25 FTE senior engineer for three years (FY12–FY14) to develop the overall plan and the cost and schedule. The installation itself is expected to take two years (FY15–FY16) and require 1 senior technician (\$500k) for supervision and planning, and 15 FTE technicians for the installation labor (\$2.5M). We also need surveyors and riggers, electricians, carpenters, *etc.*, for which we assume \$750k. Including a conservative \$1M for installation tooling and materials, the total installation effort would then be \$4.75M.

The integration of detector components is expected to require a 0.25-FTE senior engineer (\$85k) as a level of effort for the 4 years of design and construction, and 4.0-FTE designers (\$800k), for a total of \$1.14M.

10.3.10 Project Management

The project management costs are temporarily estimated at BNL rates, with 1 FTE senior physicist as Project Manager (\$275k), 0.5 FTE senior engineer as Chief Engineer (\$170k), 0.5 FTE senior administrator as scheduler (\$125k), and 0.5 FTE administrator for budget and accounting (\$90k). This team is expected to ramp up during the first year of the project and ramp down during the final year for a total of 4 years staffing during the 5 year project duration.

10.4 Cost Estimate

The cost estimate is at a preliminary stage and some of the individual estimates are quite rough. Nonetheless, we have made an effort to be realistic, rather than optimistic. Also, in view of this early state of cost development, we have assumed a high contingency of 60% on all costs. The total project cost is \$53M (FY10 \$) and is summarized in Table 10.2. With the funding profile as given in Fig. 11.1 and an annual rate of inflation of 3.5%, the total project cost becomes an inflation adjusted \$63M. Note that if Software and Computing goes off-project, which is commonly the case, the FY10 \$ cost becomes \$49.8M and the escalated cost \$59M. If, in addition, the A0 to B0 transport is covered under AIP funding, these figures become respectively \$46.3M and \$50.7M. Finally, we note that there are considerable potential savings associated with recycling of the CDF infrastructure that we have not used to offset costs. These include \$2M-\$3M on electronics infrastructure (racks, power, crates, cooling, monitoring), \$0.4M on drift chamber front-end electronics (ASDQ), and \$0.5M on power and cooling infrastructure for trigger/DAQ farm.

The total OPC includes \$300k for R&D through FY14 and \$400k for commissioning in FY15–FY16. Commissioning includes Cryogenics operations, detector operations (gas, manpower) and some spares.

11 Schedule and Funding

In this proposal, we have described a modest-scale experiment that will exploit unique accelerator facilities at Fermilab and a well-developed experimental technique to make a precision measurement of the branching fraction of the decay $K^+ \rightarrow \pi^+ \nu \bar{\nu}$. The collaboration includes the leadership and veterans of the BNL E787 and E949 experiments that observed this decay, as well as the leadership and veterans of other successful rare K -decay experiments at BNL and Fermilab. The collaboration will have to grow, but we have a solid base upon which to build.

We are requesting Stage-1 approval for this experiment. This approval is necessary for us to build a stronger collaboration and for us to make progress (with assistance from Fermilab technical staff) toward buildable and costed designs for beam-line and detector components.

If approved, we hope to achieve DOE Critical Decision 0 (Approve Mission Need) in the Fall of 2012. Technical support from Fermilab and funding from DOE/Fermilab will be required so that we can move toward CD-2 (Approve Performance Baseline) before the end of calendar 2013. Our target is to begin construction in Spring 2014. We expect no civil construction to be needed, and the detector is of modest scale compared to most recent projects in HEP. Consequently, construction can be completed in about 2.5 years.

A decision on the location of the experiment needs to be made early so that the construction schedule can be optimized to mesh with beneficial occupancy of the building and the opportunity to begin installation of beamline and detector systems. Table 11.1 lists our goals for major milestones for the experiment.

Table 11.1: Our projected timescale for major milestones and activities. Dates refer to calendar year, not fiscal year.

Milestone/Activity	Time Period
Stage One Approval	Winter 2012
DOE Approval of Mission Need (CD-0)	Fall 2012
Beam/Detector Design	2012–2013
Approve Cost Range (CD-1)	early 2013
Baseline Review/CD-2	End of 2013
Start Construction (CD-3)	Spring 2014
Begin Installation	mid-2015
First Beam/Beam Tests	End of 2015
Complete Installation	Mid-2016
First Data (Start Operations/CD-4)	End of 2016

A preliminary cost estimate for this experiment has been presented in Chapter 10. While an estimate at this early conceptual stage has large uncertainty, we have been careful to avoid a low-ball value and to keep it realistic. Significant contingency has been assumed. In addition to the beamline and detector costs presented in Chapter 10, project management costs are also included in the Total Project Cost (TPC) of \$63 M in then-year dollars, which assumes 3.5% annual inflation.

A funding profile is shown for this experiment in Figure 11.1. It is based on general considerations rather than detailed plans, but can probably be used to assess the impact of our proposed experiment and schedule on Fermilab and DOE budgets. We anticipate about 15% of the TPC to be needed for design work, which needs to be completed before the start of construction. We anticipate the need for three years of construction funding, with the bulk coming in the first two

of these three years, in order to maintain our goal to begin beamline and detector installation in 2014.

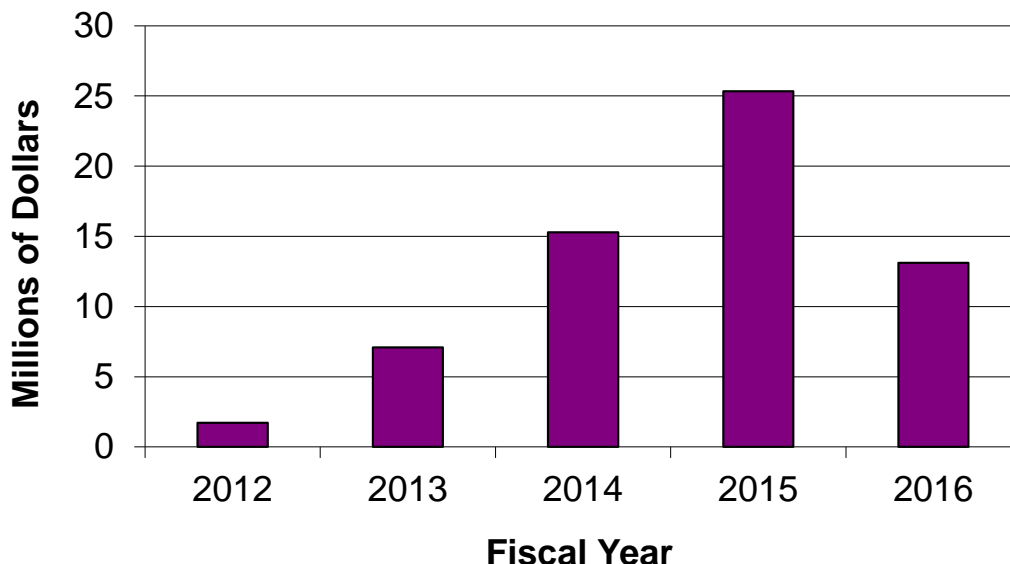


Figure 11.1: A funding profile that assumes our estimated TPC of \$63 M in then-year dollars. While based on general considerations rather than detailed plans, a funding profile close to this will be necessary to meet our proposed schedule.

While ORKA may begin operations 2–3 years after the CERN NA-62 experiment is projected to run, it would be complementary and competitive because the ORKA technique is well known and NA-62 may well require some further development in order to reach its goals. Should NA-62 proceed as proposed, ORKA would be in position either to precisely measure a deviation from the SM prediction (reaching comparable sensitivity to NA-62 in less than one year), or to carry on to reach the ultimate sensitivity allowed by the uncertainty of the SM predictions. In particular, ORKA could observe a 5-sigma deviation even if the discrepancy is as small as 35%.

Appendix A

Publications from E787/E949

Apart from the discovery and subsequent improved measurements of $K^+ \rightarrow \pi^+ \nu \bar{\nu}$, the BNL-E787/949 series of experiments made several other discoveries and measurements, and improved the limits on many other processes. In addition, E787/E949 made several technical innovations in hardware and software. These accomplishments included the development of large systems of 500-MHz transient digitizers, the scintillating fiber target, the low-mass central drift chamber with inflated cathode foils, and the E787/E949 spectrometer which was the most efficient 4π detector system ever reported. In addition, E787/E949 developed one of the first modern implementations of the blind analysis technique. The decay processes are listed in Table A. Following the table is a complete list of publications from this program.

Table A: E787/949 physics achievements

Process	Observation	Ref.
$K^+ \rightarrow \pi^+ \nu \bar{\nu}$	Discovery	[18]
$K^+ \rightarrow \pi^+ \mu^+ \mu^-$	Discovery	[19]
$K^+ \rightarrow \pi^+ \gamma \gamma$	Discovery	[20]
$K^+ \rightarrow \mu^+ \nu \gamma$	First observation of structure dependence Measurement of direct γ emission	[25]
$K^+ \rightarrow \pi^+ \pi^0 \gamma$		[26]
$K^+ \rightarrow \pi^+ X^0$	Limit	[40]
$K^+ \rightarrow \pi^+ \gamma \gamma$	Limit in dis-favored region	[36]
$K^+ \rightarrow \pi^+ \gamma$	Limit	[29]
$K^+ \rightarrow \pi^+ \pi^0 \nu \bar{\nu}$	Limit	[27]
$K^+ \rightarrow \pi^+ H; H \rightarrow \mu^+ \mu^-$	Limit	[6]
$K^+ \rightarrow e^+ \nu \mu^+ \mu^-$	Limit	[22]
$\pi^0 \rightarrow \nu \bar{\nu}$	Limit	[8]
$\pi^0 \rightarrow \gamma + X^0$	Limit	[11]

References

- [1] S. Ahmad, E. W. Blackmore, D. A. Bryman, J. Cresswell and T. Numao, “Central Drift Chamber For Rare Kaon Decay Spectrometer,” *IEEE Trans. Nucl. Sci.* **33**, 178 (1986).
- [2] J. V. Cresswell, S. Ahmad, E. W. Blackmore, D. A. Bryman, N. Khan, Y. Kuno and T. Numao, “A Cylindrical Drift Chamber for the Measurement of $K \rightarrow \pi \nu \bar{\nu}$ Decay,” *IEEE Trans. Nucl. Sci.* **35**, 460 (1988).
- [3] M. Atiya, M. Ito, J. Haggerty, C. Ng and F. W. Sippach, “Wave Form Digitizing at 500 MHz,” *Nucl. Instrum. Meth. A* **279**, 180 (1989).
- [4] M. S. Atiya *et al.*, “A Study of $K^+ \rightarrow \pi^+ \nu \bar{\nu}$,” *Nucl. Phys. Proc. Suppl.* **8**, 364 (1989).
- [5] M. S. Atiya *et al.*, “Search for the Decay $K^+ \rightarrow \pi^+ \nu \bar{\nu}$,” *Phys. Rev. Lett.* **64**, 21 (1990).
- [6] M. S. Atiya *et al.*, “A Search for a Light Higgs Boson in the Decay $K^+ \rightarrow \pi^+ H, H \rightarrow \mu^+ \mu^-$,” *Phys. Rev. Lett.* **63**, 2177 (1989).

- [7] M. S. Atiya *et al.*, “Search for the decay $K^+ \rightarrow \pi^+ \gamma \gamma$,” Phys. Rev. Lett. **65**, 1188 (1990).
- [8] M. S. Atiya *et al.*, “Upper limit on the branching ratio for the decay $\pi^0 \rightarrow \nu \bar{\nu}$,” Phys. Rev. Lett. **66**, 2189 (1991).
- [9] M. S. Atiya *et al.*, “A detector to search for $K^+ \rightarrow \pi^+ \nu \bar{\nu}$,” Nucl. Instrum. Meth. A **321**, 129 (1992).
- [10] M. S. Atiya *et al.*, “Search for the decay $K^+ \rightarrow \pi^+ \nu \bar{\nu}$,” Phys. Rev. Lett. **70**, 2521 (1993) [Erratum-ibid. **71**, 305 (1993)].
- [11] M. S. Atiya *et al.*, “Search for the decay $\pi^0 \rightarrow \gamma + X$,” Phys. Rev. Lett. **69**, 733 (1992).
- [12] M. S. Atiya *et al.*, “Search for the decays $K^+ \rightarrow \pi^+ \nu \bar{\nu}$ and $K^+ \rightarrow \pi^+ X_0$ for $150\text{-MeV}/c^2 < M(X_0) < 250\text{-MeV}/c^2$,” Phys. Rev. D **48**, 1 (1993).
- [13] M. Kobayashi, T. Shinkawa, T. Sato, S. Sugimoto, M. V. Korzhik, A. A. Fedorov and V. A. Kachanov, “YAlO-3:Ce-Am light pulsers as a gain monitor for undoped CsI detectors in a magnetic field,” Nucl. Instrum. Meth. A **337**, 355 (1994).
- [14] M. Burke, L. Felawka, R. Poutissou, S. C. Adler, J. Haggerty, R. Strzelinski and C. Witzig, “E-787 Data Acquisition Software Architecture,” IEEE Trans. Nucl. Sci. **41**, 131 (1993).
- [15] S. C. Adler *et al.*, “Search for the decay $K^+ \rightarrow \pi^+ \nu \bar{\nu}$,” Phys. Rev. Lett. **76**, 1421 (1996) [arXiv:hep-ex/9510006].
- [16] I. H. Chiang *et al.*, “CsI endcap photon detector for a $K^+ \rightarrow \pi^+ \nu \bar{\nu}$ experiment at BNL,” IEEE Trans. Nucl. Sci. **42**, 394 (1995).
- [17] D. A. Bryman, M. Constable, J. V. Cresswell, A. Daviel, M. LeNoble, J. L. Mildemberger and R. Poutissou, “500-MHz transient digitizers based on GaAs CCDs,” Nucl. Instrum. Meth. A **396**, 394 (1997).
- [18] S. C. Adler *et al.* [E787 Collaboration], “Evidence for the Decay $K^+ \rightarrow \pi^+ \nu \bar{\nu}$,” Phys. Rev. Lett. **79**, 2204 (1997) [arXiv:hep-ex/9708031].
- [19] S. C. Adler *et al.* [E787 Collaboration], “Observation of the Decay $K^+ \pi^+ \mu^+ \mu^-$,” Phys. Rev. Lett. **79**, 4756 (1997) [arXiv:hep-ex/9708012].
- [20] P. Kitching *et al.* [E787 Collaboration], “Observation of the Decay $K^+ \rightarrow \pi^+ \gamma \gamma$,” Phys. Rev. Lett. **79**, 4079 (1997) [arXiv:hep-ex/9708011].
- [21] T. K. Komatsubara *et al.*, “Performance of fine-mesh photomultiplier tubes designed for an undoped-CsI endcap photon detector,” Nucl. Instrum. Meth. A **404**, 315 (1998).
- [22] S. C. Adler *et al.* [E787 Collaboration], “Upper Limit on the Decay $K^+ \rightarrow e^+ \nu \mu^+ \mu^-$,” Phys. Rev. D **58**, 012003 (1998) [arXiv:hep-ex/9802011].
- [23] E. W. Blackmore *et al.*, “Central tracking chamber with inflated cathode-strip foils,” Nucl. Instrum. Meth. A **404**, 295 (1998).
- [24] S. C. Adler *et al.* [E787 Collaboration], “Further Search for the Decay $K^+ \rightarrow \pi^+ \nu \bar{\nu}$,” Phys. Rev. Lett. **84**, 3768 (2000) [arXiv:hep-ex/0002015].
- [25] S. C. Adler *et al.* [E787 Collaboration], “Measurement of Structure Dependent $K^+ \rightarrow \mu^+ \nu \gamma$,” Phys. Rev. Lett. **85**, 2256 (2000) [arXiv:hep-ex/0003019].
- [26] S. C. Adler *et al.* [E787 Collaboration], “Measurement of Direct Photon Emission in $K^+ \rightarrow \pi^+ \pi^0 \gamma$ Decay,” Phys. Rev. Lett. **85**, 4856 (2000) [arXiv:hep-ex/0007021].

- [27] S. C. Adler *et al.* [E787 Collaboration], “Search for the Decay $K^+ \rightarrow \pi^+ \pi^0 \nu \bar{\nu}$,” Phys. Rev. D **63**, 032004 (2001) [arXiv:hep-ex/0009055].
- [28] J. Doornbos *et al.*, “Optics design and performance of LESB3, a two-stage separated 800-MeV/c kaon beamline,” Nucl. Instrum. Meth. A **444**, 546 (2000).
- [29] S. C. Adler *et al.* [E787 Collaboration], “Search for the rare decay $K^+ \rightarrow \pi^+ \gamma$,” Phys. Rev. D **65**, 052009 (2002) [arXiv:hep-ex/0108006].
- [30] S. S. Adler *et al.* [E787 Collaboration], “Further Evidence for the Decay $K^+ \rightarrow \pi^+ \nu \bar{\nu}$,” Phys. Rev. Lett. **88**, 041803 (2002) [arXiv:hep-ex/0111091].
- [31] S. S. Adler *et al.* [E787 Collaboration], “Search for the decay $K^+ \rightarrow \pi^+ \nu \bar{\nu}$ in the momentum region $P_\pi < 195$ MeV/c,” Phys. Lett. B **537**, 211 (2002) [arXiv:hep-ex/0201037].
- [32] O. Mineev *et al.*, “Photon sandwich detectors with WLS fiber readout,” Nucl. Instrum. Meth. A **494**, 362 (2002) [arXiv:physics/0207033].
- [33] S. S. Adler *et al.* [E787 Collaboration], “Further search for the decay $K^+ \rightarrow \pi^+ \nu \bar{\nu}$ in the momentum region $P < 195$ MeV/c,” Phys. Rev. D **70**, 037102 (2004) [arXiv:hep-ex/0403034].
- [34] V. V. Anisimovsky *et al.* [E949 Collaboration], “Improved measurement of the $K^+ \rightarrow \pi^+ \nu \bar{\nu}$ branching ratio,” Phys. Rev. Lett. **93** (2004) 031801 [arXiv:hep-ex/0403036].
- [35] T. Yoshioka *et al.*, “Upgrade of the level-0 trigger system for BNL-E949,” IEEE Trans. Nucl. Sci. **51**, 334 (2004).
- [36] A. V. Artamonov *et al.* [E949 Collaboration], “Search for the decay $K^+ \rightarrow \pi^+ \gamma \gamma$ in the π^+ momentum region $P > 213$ MeV/c,” Phys. Lett. B **623**, 192 (2005) [arXiv:hep-ex/0505069].
- [37] A. V. Artamonov *et al.* [E949 Collaboration], “Upper Limit on the Branching Ratio for the Decay $\pi^0 \rightarrow \nu \bar{\nu}$,” Phys. Rev. D **72**, 091102 (2005) [arXiv:hep-ex/0506028].
- [38] S. Adler *et al.* [The E949 Collaboration and E787 Collaboration], “Measurement of the $K^+ \rightarrow \pi^+ \nu \bar{\nu}$ Branching Ratio,” Phys. Rev. D **77**, 052003 (2008) [arXiv:0709.1000 [hep-ex]].
- [39] A. V. Artamonov *et al.* [E949 Collaboration], “New measurement of the $K^+ \rightarrow \pi^+ \nu \bar{\nu}$ branching ratio,” Phys. Rev. Lett. **101**, 191802 (2008) [arXiv:0808.2459 [hep-ex]].
- [40] A. V. Artamonov *et al.* [BNL-E949 Collaboration], “Study of the decay $K^+ \rightarrow \pi^+ \nu \bar{\nu}$ in the momentum region $140 < 199$ MeV/c,” Phys. Rev. D **79**, 092004 (2009) [arXiv:0903.0030 [hep-ex]].

Appendix B

The E949 Detector

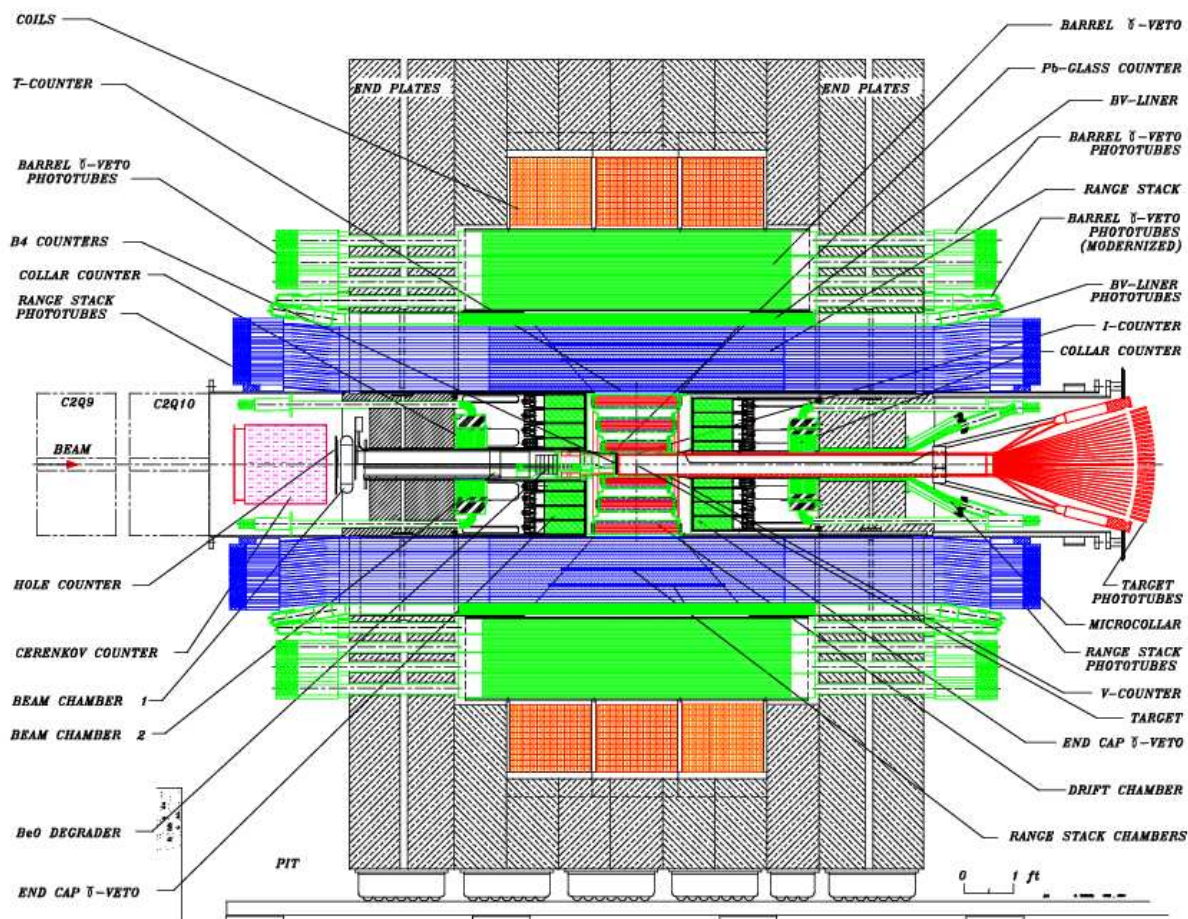


Figure B: Elevation view of the E949 detector. The beam enters through the Čerenkov detector, and several key components are labeled.